SCULPTING ON THE NANOSCALE

INVESTIGATING ARTIFICIAL ATOMS, MOLECULES AND LATTICES

VORMGEVEN OP NANOSCHAAL

ONDERZOEK NAAR KUNSTMATIGE ATOMEN, MOLECULEN EN ROOSTERS

Saoirsé Erin Freeney

Printing: Proefschriftmaken || www.proefschriftmaken.nl

Design: Nathan Middelham || www.heartanddata.com

ISBN: 978-94-6423-403-9

Cover description: A selection of images of CO molecules on copper(111) depicting the steps of construction of the artificial matter discussed in this thesis. The process is shown to occur on a sculpture, Venus de Milo, which is selected because of the historical association of Venus with copper.[1]

Bookmark/invitation image description: A series of quantum corrals constructed with CO on Cu(111).

Sculpting on the Nanoscale

Investigating Artificial Atoms, Molecules and Lattices

Vormgeven op Nanoschaal
Onderzoek naar Kunstmatige Atomen, Moleculen en Roosters
(met een samenvatting in het Nederlands)

Proefschrift

ter verkrijging van de graad van doctor aan de Universiteit Utrecht
op gezag van de rector magnificus, prof.dr. H.R.B.M. Kummeling,
ingevolge het besluit van het college voor promoties
in het openbaar te verdedigen op

woensdag 25 augustus 2021 des middags te 12.15 uur

door

Saoirsé Erin Freeney

geboren op 9 april 1994
te Londen, Verenigd Koningkrijk

Promotor:
Prof. dr. D.A.M. Vanmaekelbergh

Copromotor:
Prof. I. Swart

Dit proefschrift werd (mede) mogelijk gemaakt met financiële steun van de Nederlandse Organisatie voor Wetenschappelijk Onderzoek.

CONTENTS

CHAPTER 1

INTRODUCTION

This chapter was written for this thesis.

This thesis describes the creation of artificial matter at the atomic scale, molecule by molecule.

This statement might seem fantastical, but the scanning tunnelling microscope (STM) is capable of bringing it to reality. This chapter presents a brief introduction to the thesis and a short description of STM. Chapter 2 then provides a deeper background.

The origins of scanning probe microscopy extend as far back as half a century,[2] with the STM itself being invented in 1981.[3] This allowed individual atoms to be resolved in real space for the first time in history. It was not long after the invention of STM that the first atomic-scale structure was assembled at will: researchers at IBM wrote out their company initials with xenon atoms on nickel.[4] The technique of atomic manipulation was demonstrated again to create a so-called quantum corral, which herded electrons to a confined space.[5] The corral was a ring of iron atoms on the surface of copper(111). On the (111) termination of copper, there exists a "sea" of electrons that arises from Shockley states. Adsorbates placed on the surface scatter these electronic states, which results in standing wave patterns measurable using scanning tunnelling microscopy. What is imaged in a typical STM topograph is proportional to the probability density $|\Psi|^2$, and visually it is reminiscent of the ripples that form when a raindrop hits a puddle.

When adsorbates are arranged in such a way as to enclose a space within (in the 1993 quantum corral work,[6] the enclosure was circular), then the electrons are confined, and their wave functions and energy levels become quantised. The remarkable thing is that by merit of the quantised states, this is directly comparable to atomic behaviour. Where atoms constrain electrons with an attractive potential at the core, quantum corrals constrain them with a repulsive potential from the outside. This entails that quantum corrals can be considered artificial atoms. Quantum corrals can be coupled together to form artificial molecules, exhibiting bonding and anti-bonding orbitals specific to molecules. This idea can be extended as far as to create entire artificial two-dimensional lattices, by sculpting the desired potential landscape one adsorbate at a time. The first example of a lattice constructed in this way was artificial graphene.[7] Using carbon monoxide on copper(111), the electronic surface state was confined to a hexagonal pattern. Not only did the group emulate the electronic behaviour of graphene, but they also (i) opened a band gap by altering the lattice unit cell, (ii) effectively n- and p- doped the artificial graphene by changing the lattice constant, and (iii) simulated a magnetic field by tweaking the lattice geometry. This work revealed the value of artificial lattices produced adsorbate-by-adsorbate: they are highly tunable and local density of states measurements can be performed immediately. The crux is that we are not limited to mimicking structures that are known to exist. In fact, since the artificial graphene publication,[7] a plethora of investigations have modelled novel systems using the same platform of CO on Cu(111).

As a brief aside, this genre of quantum simulator is by no means the only. Cur-

rently, there are an array of techniques that grant control and measurement of artificial quantum states, including (magneto-)optical lattices,[8–11] photonic lattices,[12] (topo)electrical circuits[13] and acoustic systems.[14–16] Even within the realm of STM, other methods of construction of artificial matter have been shown.[17–22]

1.0.1 How does one create artificial matter?

Specifically, how can one use carbon monoxide, copper and a scanning tunnelling microscope to wield control over the behaviour of electrons? First, the copper surface must be atomically flat. A copper crystal is cut and polished such that its top surface is the (111) facet (figure 1.1a). It is then inserted into vacuum, sputtered and annealed. This is the process of bombarding the surface with argon ions to remove any contaminants, and warming up the sample such that the surface atoms relax into their minimum energy configuration, which is flat. The sample is then moved to the STM chamber and inserted into the measurement head, all the while remaining in ultra high vacuum. For all research described in this thesis, we made use of the Omicron LT-STM shown in figure 1.1b, cooled to 4.5 K using liquid helium. Once there, carbon monoxide can be leaked into the chamber where it adsorbs onto the Cu(111).

The scanning tunnelling microscope

The STM houses an atomically sharp needle sitting at an electrical bias with respect to the sample. This needle, or tip, is used to electronically "read" the surface like braille. Before measuring, the STM tip is driven towards the copper surface until a current on the order of nano-amperes is detected. This current arises from quantum mechanical tunnelling between the tip and sample, and is inversely exponentially dependant on the distance between them; that is to say, the smaller the gap between tip and sample, the *much* more probable the tunnelling. It is this great sensitivity that allows us to resolve features on the sub-nanoscopic scale. Using fine piezoelectric motors, the tip scans across the surface, maintaining constant current by slightly retracting and approaching when necessary. Figure 1.1c shows a representation of an STM tip as it scans a quantum corral. Usually, CO molecules are visualised as dips in the surface (as seen in figures 1.1e and f, but in figure 1.1c, the scan was experimentally acquired with a CO-terminated tip, which results in CO molecules appearing as protrusions. The trace of the tip's path is shown. The tip height is measured at each point in the scan, and is translated to a pixel intensity in an STM image. Figure 1.1d shows an exemplary Cu(111) surface, on a length scale 10,000 times smaller than the diameter of the sample. This figure is 500 nm wide, which is the wavelength of cyan/green light; the atomic terraces in this figure are smaller than could be resolved with an optical microscope, yet with STM, still smaller and smaller (figures 1.1e and f) areas can be measured.

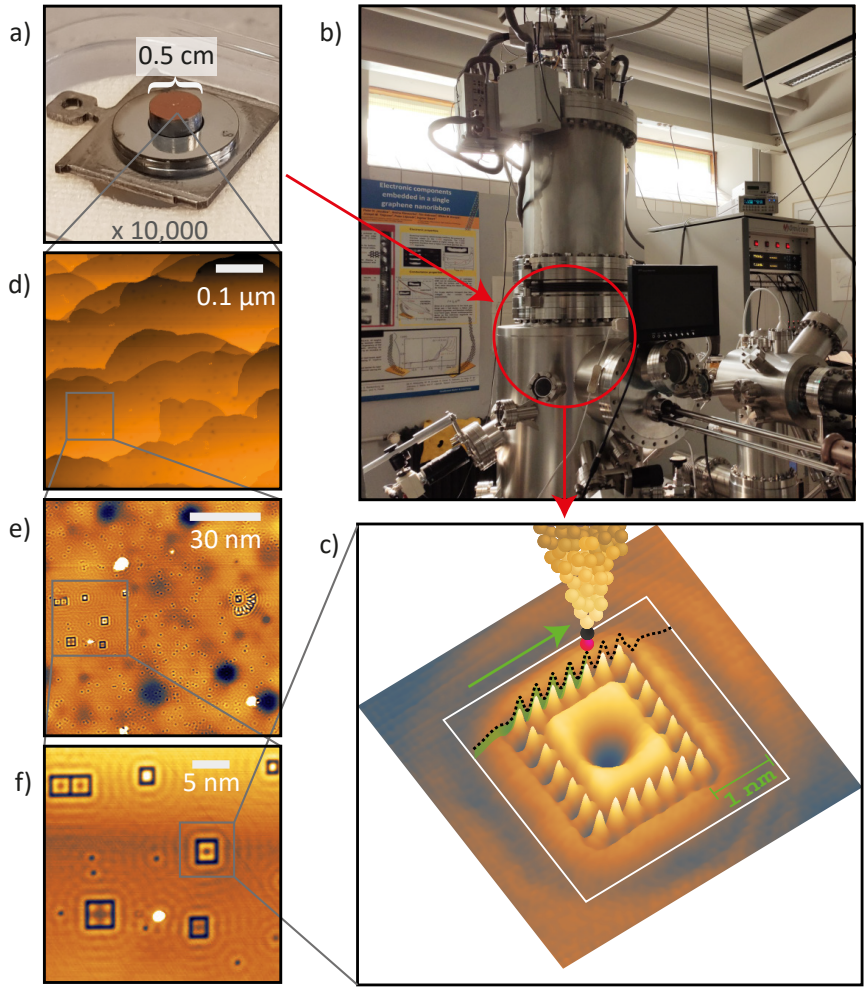

▲ Figure 1.1: **Zooming in on artificial matter.** (a) A copper crystal with a (111) terminated surface. (b) The Omicron LT-STM in which experiments were performed. (c) Representation of a CO-terminated tip (black = carbon, red = oxygen) scanning a quantum corral (the scan is a real experimental image). (d) A Cu(111) surface, with step-edges visible. (e) a flat terrace on the surface, where a "quantum playground" has been constructed. (f) a closer view of rectangular quantum corrals.

While scanning tunnelling microscopy is a powerful tool, one limitation is the requirement of heavy involvement from the user. For a crisp, atomically resolved image, the STM tip should be atomically sharp, which can be time-consuming to obtain. Recently, some scanning probe groups have begun to develop tools to automate the tip conditioning process. Automation has clear value in creating artificial matter adsorbate-by-adsorbate, but also more generally in scanning probe microscopy as a whole. Part of this thesis describes the use of neural networks for STM image recognition.

1.0.2 Thesis outline

This thesis adds to the body of work on artificial lattices produced with the CO/Cu(111) platform in several ways.

- In chapter 2, an introduction and broad overview on electronic artificial lattices is given, and most lattices that have been created with the CO/Cu(111) platform are reviewed. We also give an outlook on how such research could find applications in technology.
- Chapter 3 presents the goal of making STM experiments as a whole more efficient, therefore reducing the time needed to fabricate artificial lattices atom-by-atom. To this end, we developed an algorithm that could distinguish the state of the STM tip using neural network-based image recognition.
- The basic elements of the CO/Cu(111) platform - quantum corrals - and their coupling into artificial molecules, were investigated in chapter 4. This allowed us to gain a sense of the range of parameters that can be tuned in artificial lattices of the same sort.

In the remaining chapters, we engineered and performed measurements on two artificial lattices with the CO/Cu(111) platform that have theoretically been predicted to have interesting properties, but in nature do not exist.

- Chapter 5 reports the results of a study into an artificial crystalline topological insulator (TCI). Specifically, we exploit the atomic scale precision to study the influence of edge geometry on the emergence of topological states in TCIs.
- Finally, chapter 6 describes a study into how two-body interactions in 1D can be investigated using a non-interacting 2D artificial lattice.

The thesis ends with summaries in English and Dutch.

CHAPTER 2

ELECTRONIC QUANTUM MATERIALS SIMULATED WITH ARTIFICIAL MODEL LATTICES

This chapter is partially based on:
Electronic quantum materials simulated with artificial model lattices.
Saoirsé E. Freeney, Marlou R. Slot, Thomas S. Gardenier, Ingmar Swart and Daniel Vanmaekelbergh.
In preparation

2.1 Introduction

The field of (topological) electronic quantum materials is one of the major research directions in current solid-state physics, connecting theorists, solid state chemists, materials scientists and experimental physicists. This rapidly expanding field has its origin in several theoretical and experimental advances starting in the 1980s, and was boosted by the isolation and full electronic characterization of graphene.
The purpose of this review is firstly, to highlight some of the major advances in this field; secondly, to discuss the endeavour to experimentally model and characterise quantum materials that have been theoretically predicted; thirdly, to present some examples of electronic lattices produced molecule-by-molecule in STM with the CO/Cu(111) platform; and finally - having gone from theory to experimental modelling - to conclude with an outlook on real materials that could make use of novel quantum effects, and have technological applications.

2.2 The emergence of electronic quantum materials

Although the concept of a "quantum material" is not strictly defined (indeed, the electronic properties of all materials have a basis in quantum mechanics), some materials could be considered more "quantum" than others. In the last decades, a number of striking macroscopic physical phenomena have emerged that can most appropriately be explained by plain quantum physics. Notoriously, two-dimensional electron gases exhibiting the quantum Hall[23] and fractional quantum Hall effects,[24] several types of (high-temperature) superconductors,[25,26] semiconductors with opto-electronic properties that depend strongly on the overall dimensionality of the crystal (0D – 2D)[27–29] the nanogeometry,[30–37] and more recently, the rapidly expanding field of quantum materials with electronic surface or edge states, topologically protected by bulk band inversion and bulk-boundary correspondence.[38–56] The band inversion in these materials is caused by band shifts due to strong spin-orbit coupling or certain crystal symmetries. More generally, the extended electronic wave functions of the system and the related electronic band structure and electronic properties depend in an intricate way on (i) the atomic elements of the crystal defining the strength of spin-orbit coupling or magnetic effects, (ii) the precise atomic registry; that is to say the crystal structure including the surfaces and edges, and the effects of strain and electron occupation; (iii) the overall dimensions of the crystal, (iv) for 1D and 2D systems, the superimposed nanogeometry, inducing for instance alternating weak and strong hopping, and (v) the presence of Coulomb or spin interactions between the quasi-particles.
Theory has been dominant in the still young field of quantum materials. Several quantum phenomena of high potential interest have been put forward by theorists.[55,57–67] Experimental realizations often lag behind these theoretical developments because a given "theoretically interesting" crystalline material has to be

grown as a crystal with the right chemical composition and crystal structure, dimensionality, and nanogeometry. In addition, the crystal should not have (too many) defects or impurities. Then, the material has to be structurally characterized up to the atomic level. Study of the electronic band structure requires incorporation of the material in an optical or electronic device for cryogenic spectroscopy and/or transport measurements. For graphene, this cycle could be completed due to its intrinsic simplicity, simple growth and isolation, and chemical stability. Transport measurements in a magnetic field unambiguously demonstrated the anomalous quantum Hall effect, related to the electronic Dirac band structure of graphene.[68] Graphene can also be deposited or grown relatively easily on a flat metallic or insulator surface, allowing for atomic force[69–72] and scanning tunnelling microscopy and spectroscopy.[72–79] An active and promising area of interest at present is the molecular synthesis of atomically precise ribbons of graphene[80] with well-defined armchair or zig-zag edges. The electronic band structures of these nanoribbons can be obtained from scanning tunnelling spectroscopy measurements. This work reveals the direct influence of dimensions, edges and geometry on the electronic properties of a 2D crystal, and has revealed the emergence of topologically protected electronic phases.[70,80–90]

The quantum materials that arrived on the scene after graphene were generally more complex. Strained 2D HgTe was the first material discovered that manifested the famous quantum spin Hall effect.[50,52,91] The two-dimensional crystals of HgTe obtained a tweaked zinc blende crystal structure due to strain induced by epitaxy with CdTe. The strained zincblende structure and the strong intrinsic spin orbit coupling present in HgTe induces inversion of the conduction and valence bands. As a result, a topologically protected insulating gap arises in the HgTe crystal, with Dirac-type and helical electronic states at the edges of the crystal. Here, helicity means that there is an edge state with the spin locked to its momentum in one direction, say $(k, \uparrow)$, and a second counterpropagating spin mode $(-k, \downarrow)$. The states are dissipationless to a large extent as back scattering without spin-flip is not allowed without a large energy input. Later, 2D HgTe was reconsidered, but with a superimposed honeycomb geometry with nanometre periodicity. For this system, Dirac type hole valence- and electron conduction bands have been calculated. Due to the strong intrinsic spin-orbit coupling, a robust 30 meV gap arises at the Dirac point, hosting quantum spin Hall edge states.[37] In this system, the quantum spin Hall effect arises due to the honeycomb geometry combined with strong intrinsic spin-orbit coupling.[92,93] Two-dimensional crystals of HgTe with a honeycomb geometry on the nanoscale have not yet been experimentally realized.

2.3 Artificial electronic lattices as model systems

The examples above show the need for - and suitability of - analogue simulations with artificial electronic lattices. This entails the creation of lattices with certain

geometries mimicking real materials (or sometimes, materials that are not known to exist in nature), and characterization of the band structure including the edge or corner states. Some materials might be so complex or difficult to fabricate that it is worth building an artificial analogue that mimics a number of the essential elements of the original material, and is thus described with a similar Hamiltonian. Artificial lattices provide more control and are often easier to characterize than complex real materials.[94] Such quantum simulators have addressed questions in electronic materials science,[8,9,95–99] fundamental physics,[100–104] and chemistry.[8,103,105] As far as we know, the first ideas on quantum simulation originate from Richard P. Feynman.[106,107] Furthermore, with his lecture "There is plenty of room at the bottom", he anticipated the creation of quantum architectures by control over individual atoms, nothing more than a vague concept at that time. At present, this is fully realized with cold atoms in optical lattices and with atomic manipulations in a scanning tunnelling microscope.

The artificial lattices presented here are electronic in nature and fabricated in a scanning tunnelling microscope by atomic manipulation of adsorbates on a flat metallic surface. The concept of an artificial electronic lattice, its physical elements and its characterization will be discussed below. Briefly, artificial two-dimensional sites can be defined by groups of adatoms or carbon monixide molecules on well-defined positions on a metallic substrate. In such a way, the surface state electrons are forced into artificial sites that, together, form a lattice. The atom-by-atom construction by atomic manipulation provides atomically exact lattices, devoid of impurities. Scanning tunnelling microscopy maps the structure of the lattice. With scanning tunnelling spectroscopy, the local density of states (LDOS) can be measured, from which the band structure can be derived. This methodology can thus provide a one-to-one relationship between electronic band structure and the atomic lattice.

Artificial model systems are versatile. In addition to mimicking 2D materials on an atomic level, defects and impurities can be introduced and the consequences for the electronic band structure can be quantified. In an artificial lattice, it is also possible to change one parameter at a time, which is usually not the case in real materials. Furthermore, theories often use simplified assumptions; artificial lattices enable us to check the validity of these assumptions. For instance, band structure predictions are often based on tight-binding calculations based on nearest-neighbour hopping only. Measurements on artificial lattices have shown that next-nearest-neighbour hopping may substantially change the predicted band structure, for instance showing that predicted flat-bands obtain a (weak) dispersion.[108]

So far, electronic correlations, electron pair formation, and spin-orbit coupling have not been fully introduced in artificial electronic lattices, although they are essential physical elements of many real quantum materials and may result in topologically protected electronic phases.[38,109–113] These components are important next-steps in the pursuit of the mastery of quantum materials. It is possible that a metal-

lic substrate or adatoms of high atomic mass, such as thallium, lead or bismuth could induce spin-orbit coupling into the surface-state electronic gas by proximity,[114] and the same holds for electron pair formation. Coulomb interactions between the electrons are an essential element in many quantum materials. The artificial lattices reported so far have a high electron density and thus a strong screening of these interactions. In order to simulate Coulomb interactions, electron-poor surface-states will be required or systems in which the density of the surface gas can be manipulated by an electrostatic gate. This stage has not been reached yet. It can be concluded that in the present stage, artificial lattices prepared on flat metallic surfaces are appropriate to simulate the effects of lattice geometry in the single-electron regime. Even with these limitations, interesting lattices with Dirac bands, flat bands and topological edge states have been simulated in a convincing way. The discussion of the rendering of topological edge states with artificial lattices is omitted from this chapter and can be found instead in chapter 5 of this thesis, in full. Before the rest of these systems are reviewed, analogue quantum simulations with particles other than electrons are shortly discussed.

2.4 Quantum simulations with other platforms

A large variety of platforms are used for analogue quantum simulation, e.g. ultra-cold atoms, trapped ions, superconducting circuits, gated semiconductors and optical lattices. The platform in which analogue quantum simulations have reached the most advanced stage is that of ultra-cold atoms caught in optical lattices.[8–11] Two-dimensional lattices with potential wells and barriers are created with crossing laser beams; they are loaded with ultra-cold atoms - bosons or fermions - with a temperature in the nanokelvin regime.[115,116] The atomic occupation of each lattice site is measured by light scattering and monitored as a function of the on-site energies, tunnelling barriers, lattice geometry and external fields. The average occupation is usually smaller than one atom per lattice site. Although the lattice engineering, length scales, particles and monitoring of the particle positions are completely different from that in electronic lattices, the class of physical questions that can be investigated is similar. For instance, flat-bands in the Lieb and honeycomb lattices have been simulated.[97,108,117,118] This has also been done with artificial electronic lattices. The advanced stage of cold-atom optical lattices has enabled the investigation of on-site interactions and spin-orbit coupling.[97,119–121]

A second material system that has proved successful in analogue quantum simulations is that of pillar-arrays of III-V semiconductors. Each pillar contains a stacking of quantum wells and optical cavities to increase the interaction between a quantum-well exciton and its resonant photon. The resulting particle (or excitation) of interest is hence an exciton-polariton.[122] The geometry of the array of semiconductor pillars defines the lattice with lattice sites and hopping barriers for the exciton polaritons.[123–142] The de Broglie wave-length of exciton polaritons is large, and

is used to control hopping and interaction. Exciton-polariton lattices are powerful quantum simulators and could simulate the effects of lattice geometry on the band structure, from the single-particle regime[124,143–146] to that of (strong) interactions.[147–149] In the limit that exciton-polaritons are nearly photons, one deals with purely photonic lattices, which also have shown strong potential for quantum simulation.
Quantum simulations with arrays of semiconductor quantum dots in which the electron occupation can be controlled by individual gates also allow the study of many-body effects.[104,150–153] These arrays are most alike the artificial lattices on metallic surfaces that are presented below.

2.5 Methods of preparing artificial lattices in STM

This section will describe the separate physical elements underlying the modelling of quantum materials with artificial electronic lattices. Each of these elements is the result of extensive theoretical and experimental research, work that in some cases has even resulted in a Nobel prize. We have chosen to construct a brief and comprehensive review that contains sufficient detail to understand the principles behind the creation and electrical characterization of artificial electronic lattices and analogue quantum simulation.

2.5.1 Scanning tunnelling microscopy and spectroscopy

After its invention,[154,155] scanning tunnelling spectroscopy was rapidly developing as an accurate method to map the atomic structure of metallic surfaces, adsorbed flat molecules or two-dimensional systems. In brief, an electrically conductive tip is scanned over a metallic surface, with the tip in quantum mechanical tunnelling contact with the surface. This means that the tip is within a nanometre of the metallic surface. A bias V is applied between the tip electrode and the metallic substrate, inducing an electric field over the vacuum gap between the tip and the metal surface. This results in a controlled difference between the Fermi-level of the tip and that of the substrate; the thermodynamic driving force for directed electron tunnelling. The bias V is defined as $eV = E_{(F,tip)} - E_{(F,sample)}$. The convention is that at positive bias, the Fermi level of the tip, $E_{(F,tip)}$, is at higher energy than that of the sample, $E_{(F,sample)}$. When V is different from zero, an electron tunnel current flows from the tip to the substrate, or vice versa, and this current (usually smaller than 1 nA) is measured in an external circuit. At positive bias, electrons can tunnel from the tip to the substrate. Quantum mechanical electron tunnelling between (the last atom on) the tip and the metal surface is exponentially dependent on the tip-surface distance, which may allow the measurement of the atomic periodicity of the metal surface, or the presence of adatoms or molecules. In other words, a spatial map of the current variations represents the atomic corrugation of

the surface and highlights adsorbed species. Alternatively, and more commonly, the tip height at constant current is used to map the atomic structure of the surface. Surface steps, adatoms and molecules can be detected.

The scanning tunnelling microscope also allows one to perform powerful spectroscopy, providing the local electronic density of states, denoted as LDOS(E, x, y). Briefly, the tip is positioned with atomic accuracy at a specific position (x, y) on the sample. The bias V between the tip electrode and the substrate is varied, and the tunnel current I and conductance $\frac{dI}{dV}$ are measured as a function of the bias V; $\frac{dI}{dV}$ vs. V corresponds then to the LDOS(E) at that position. In order to understand this, one has to consider a quantum mechanical system with discrete energy levels (e.g. an adatom, molecule, quantum dot) on the substrate surface with the tip placed above this system. When the bias is increased above zero, a tunnel current is detected when the Fermi-level of the tip becomes resonant with an empty energy level of the quantum system. Hence, the empty energy level is seen as a step in the (I, V) curve or as a peak in the $\frac{dI}{dV}$ vs. V plot. The next energy level is then seen as a second peak in the $\frac{dI}{dV}$ vs. V plot. The same holds when the bias is made negative, and the filled energy levels of the quantum system are detected by onsets of tunnelling from the substrate to the tip. Hence, the energy levels of quantum mechanical objects on a metallic surface can be measured by scanning tunnelling spectroscopy.[156–167] Two remarks should be added: First, when an electron enters an adsorbed quantum system, it charges this object; this means that the resonance occurs at an energy equal to single-particle energy + the charging energy (also noted as self-energy). This charging energy can be expressed as e^2/C , with C being the capacitance of the quantum object. Second, if a second electron tunnels into the object before the first one has left, double charging occurs, and the resonance for the second electron is increased by an energy amount equal to the Coulomb repulsion between both electrons.[168] This means that, in principle, tunnelling spectroscopy allows one to quantify the single-particle energy of the eigenstates, and the electron interactions of the quantum mechanical system.[163]

Here, we focus on the spectroscopy of artificial atomic sites and artificial lattices prepared directly on metallic surfaces. The screening of the self-energy and electron-electron interactions is strong, and it is safe to assume that the resonances discussed below quantify the single-electron energy levels or dispersive bands of the system. Hence, the single-particle local density of states LDOS(E) is measured at a certain position by $\frac{dI}{dV}$ vs V. The amplitude of the $\frac{dI}{dV}$ is proportional to the squared wave function of the eigen-state at given bias (given energy): $\frac{dI}{dV} \propto \psi(E, x, y)^2$. In other words, maps of $\frac{dI}{dV}$ at given bias V reflect the squared wave functions $|\psi(E, x, y)|^2$ of the system. Scanning tunnelling microscopy, spectroscopy and wave-function mapping are suitable for the study of artificial lattices. A seminal example studying an artificial honeycomb lattice prepared with CO molecules as repulsive scatterers on Cu(111) was reported in 2012.[7]

2.5.2 Metals with surface state two-dimensional electron gases

In 1939, William Shockley published an influential work on the energy levels and bands related to the surfaces of three-dimensional metallic crystals.[169] This work commented on - and incorporated earlier work of - Tamm[170,171]and Goodwin.[172–174] The argument begins with a finite linear chain of quantum-mechanically coupled atoms. It is obvious that the potential energy landscape at both ends of the chain is different from the interior of the chain. The coupling of N atoms in the chain results in N energy levels that can form a dispersive band. Due to the deviating potential landscape of the ends of the chain, two of the N energy levels can be energetically separated from the band, and may even be found in a gap between two bulk bands. The two energy levels have a strong electron density localisation over a few atoms at the ends of the chain. In the three-dimensional case, considering a crystal of $N \times N \times N$ atoms, on the order of N^2 levels are localised on surface atoms. Shockley anticipated that these energy levels themselves can form a two-dimensional band, separated from the bulk bands. Such a band thus contains electrons caught in a two-dimensional potential with free motion and wavevectors parallel to the surface, i.e. a two-dimensional electron gas. Surface bands of energy close to or overlapping with the bulk Fermi level are of particular importance.

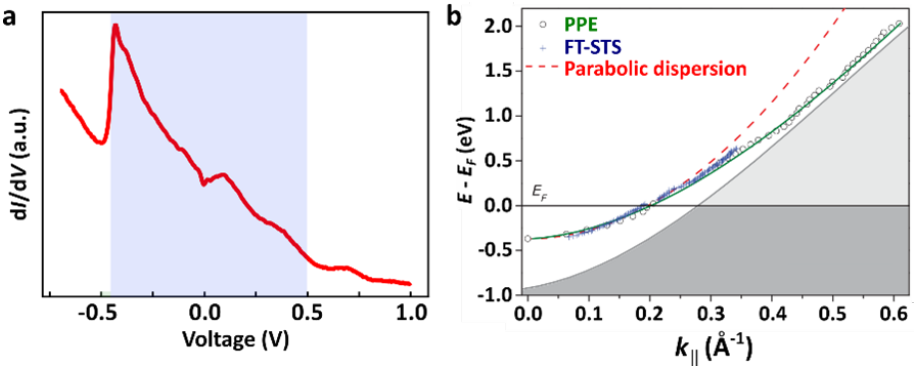

▲ Figure 2.1: **A two-dimensional electron gas residing on the surface of Cu(111).** (a) Typical surface state band of a Cu(111) surface as characterized by scanning tunnelling spectroscopy. The surface-state emerges at V = -0.45 V. The shaded energy range between -0.45 V and 0.5 V is suitable to localise electrons in artificial lattices. (b) Energy-wavevector dispersion of the Cu(111) surface state electrons presented in the gap above a filled bulk band (grey). The Fourier-transformed scanning tunnelling spectroscopy data (blue) coincide with the results of photoemission spectroscopy (green) and follow a parabola in the energy range between -0.45 V and 0.5 V. Reproduced with permission from Ünal *et al.*, Physical review B (2011).[175]

The surface-state band of a Cu (111) surface, characterised by scanning tunnelling spectroscopy, was reported by the IBM Almaden group, and confirmed by other experiments.[5,176,177] Figure 2.1 shows the results that were obtained. The surface state density sets on at an energy of -0.45 eV with respect to the Fermi-level, rises rapidly to a maximum, before slowly decaying to become negligible at 0.5 eV. With Angle Resolved Photo Emission Spectroscopy (ARPES) the energy vs. surface-parallel wavevector dispersion is determined, being nearly the same to that obtained with scanning tunnelling spectroscopy.[176–178] The energy region between -0.45 and +0.5 eV is thus the region in which artificial atomic sites and lattices will be able to localise the Cu(111) surface state electrons as standing waves, see below. More generally, the energy vs. wave vector dispersion relation of (electron-occupied) surface bands has been investigated extensively with scanning tunnelling spectroscopy and Angle Resolved Photoemission Spectroscopy (ARPES), for several facets of noble metals.[157,179–192] Alternatively, the oscillatory LDOS patterns of the surface waves at step edges of scattering adatoms can be measured as a function of the bias, finally providing the dispersion relation and the effective surface electron mass, reported to be around 0.38 m_e to 0.42 m_e for Cu(111).[5,193–195] Furthermore, surface states can hybridise with the specific energy levels of an adatom, giving rise to an atom-localised electronic state that can often be distinguished from the two-dimensional surface band by scanning tunnelling spectroscopy. For instance, a Cu adatom on a Cu(111) surface state gives rise to a localised state of energy just below the onset of the surface band itself.[196] By using atomic manipulation, chains of Cu adatoms could be prepared. The energy levels and $\frac{dI}{dV}$ maps, proportional to the squared wave function, appear to be determined by the size and shape of the atomic chain.[18,197–200] In fact, these energy levels can be considered as arising from standing waves in a "molecule" of ad-atoms, in other words an "artificial atomic site" emerges. Such architectures and others can be prepared on a sample surface with atomic accuracy, in a cryogenic scanning tunnelling microscope. Atomic manipulation is the second physical element required to prepare and study artificial lattices.

2.5.3 Atomic manipulation of atoms or small molecules adsorbed on a metal surface

Adatoms and small molecules such as CO chemisorb on clean and flat metal terraces in such a way that a minimum-energy configuration is formed.[201] Adatoms on e.g. a (111) face of an fcc crystal typically take the trigonal valley between three atoms of the metal surface, to maximise van der Waals and chemical interactions. CO forms an interesting exception to this, as on e.g. a Cu (111) surface it binds with is carbon atom on top of a Cu atom.[202] If a metallic tip is brought closer to a chemisorbed CO or adatom, the adatom/tip attraction can become of the same order as the chemisorption energy, and an adatom might be transferred from the sample to the tip and placed on another well-defined position on the surface (i.e.

vertical manipulation[203]). In a subtler way, a tip can exert a force that allows to either drag, push, or pull the adatom or CO along the sample surface, put it on a well-defined position and retract the tip, i.e. horizontal manipulation. This atomic manipulation technique was developed at the beginning of the 1990s in the IBM Almaden group and extended by other groups; it was shown that noble gas atoms and transition metal adatoms could be positioned on a flat metallic surface.[4,193,203–210] Later, CO molecules chemisorbed with the C atom on top of the surface atoms could also be manipulated.[203,209] As CO molecules act as barriers for surface state electrons, they are suitable for the preparation of artificial atomic sites, molecules and lattices by enclosing these electrons in a limited surface space. It is this method that has been used extensively to prepare artificial lattices and even fractal structures, see below.

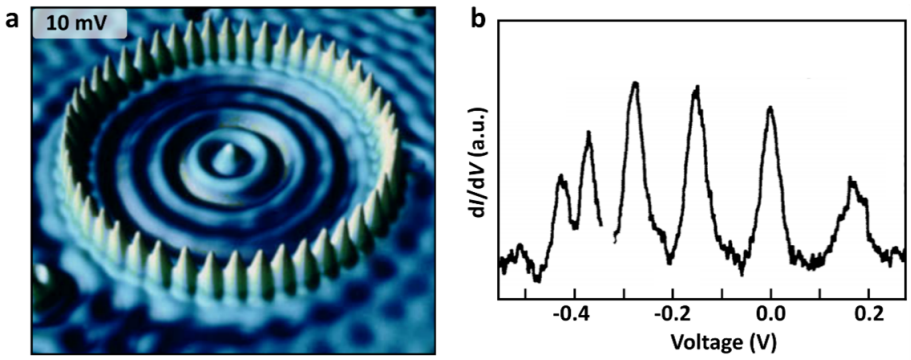

▲ Figure 2.2: **A quantum corral or artificial atom in two dimensions prepared on a Cu surface by atomic manipulation.** (a) The quantum corral consists of 48 Fe atoms, positioned by atomic manipulation into a circle with a radius of 7.13 nm. The scanning tunnelling spectroscopy map (LDOS(x, y)) at given energy E) reveals the standing-wave pattern inside the corral at a bias of V = 10 mV. (b) The LDOS(E, x, y) acquired in the centre of the corral, shows well-defined discrete energy levels, which can be considered as the eigenstates of the artificial atom. Reproduced with permission from Binnig, G. and Rohrer, H. In touch with atoms.[211]

2.5.4 Artificial atoms and molecules defined by adatoms

In this section, we focus on the electronic properties of artificial systems assembled with lateral manipulation. The reader that is interested in the magnetic properties of such systems is referred to reference.[212]

The ability to create atomically well-defined chains of adatoms allowed the evolution of the electronic structure with system size to be studied. A characteristic example was the formation of chains of Cu adatoms on Cu(111). The orbitals of Cu adatoms interact with the Cu(111) surface band, and form new particle-in-a-box type states predominantly localised on the chain.[196–198] The interaction of these quantum eigenstates with (i) the surface band living outside the system, and (ii) bulk bands of the Cu substrate results in a broadening of the states.[178] Experiments with other metal adatoms on metal surfaces corroborate these findings.[17,213–215] Such experiments have also been performed on the surface of semiconductors[216–218] and using dangling bonds.[22] Atomically well-defined systems can also be used to study more exotic phenomena such as Majorana quasi-particles. For example, the Wiesendanger group used lateral manipulation to construct atomically precise chains of Fe atoms on a superconducting Re(0001) surface.[219] Spin-polarized STM experiments revealed the presence of spin-spirals in these chains. Hence, the required ingredients for the formation of Majorana quasiparticles are present. Indeed, the ends of the chain feature pronounced zero-energy modes. Such modes have also been observed by other groups using self-assembled molecular chains on Pb surfaces.[220–222]

2.5.5 Artificial atoms, molecules and lattices defined by vacancies in an atomic layer.

Another way to prepare artificial systems is to couple the localized states of atomic vacancies. Cl-vacancies in chlorine terminated Cu(100) can be manipulated and positioned at will, using the STM tip.[223–225] The Cl-vacancies act as artificial atomic sites with well-defined energy levels, and the ability to couple to identical neighbouring artificial sites. The emergence of quasiparticle Bloch states was studied.[225,226] In addition, a variety of 1D chains exhibiting topological end states and flat bands were realized,[227] as well as a two-dimensional Lieb lattice.[21] The latter lattice has strong similarities with the Lieb lattice that will be discussed below.[98]

2.5.6 Artificial atoms, molecules and lattices defined by confinement between adsorbates

The oscillatory patterns observed close to step edges and impurities indicated that the surface state electron waves, moving parallel with the surface, scatter with many sorts of adatoms. In a seminal work, corrals of such scatterers were prepared by atomic manipulation.[193] Inside the corral, the local LDOS shows a standing-wave pattern, which indicates the squared wave function of electron states of the corral (see above, section 1, and figure 2.2). A quantum mechanical explanation of the energy levels and wave functions of such quantum corrals showed that they can be considered as artificial two-dimensional atomic sites.[228,229] In the next section, we present quantum corrals as artificial atoms, forming the basis for artificial molecules and artificial lattices.

2.6 Artificial atoms and molecules in two dimensions

Consider a corral defined by CO atoms on the Cu surface state, see figure 2.3a. Each carbon monoxide molecule acts as a repulsive scatterer with a potential barrier height of about 0.9 eV per CO.[230] By placing CO molecules in a ring, a circular particle-in-a-box system can be approximated.[5,193] Electrons within the corral take on quantized energy and angular momentum,[229] akin to real atoms. To see how this arises, we revise the particle-in-a-circular-box problem, then we make detailed comparisons to the hydrogen atom. We then present how a 2D artificial atom can be realised experimentally and characterised with the CO/Cu(111) platform.

2.6.1 The particle in a circular well

We define the origin of the disk-like quantum corral at its centre, and let the radius be a. For simplicity, a potential well of infinite height around the circular artificial atom is assumed:

$$V(r) = \begin{cases} 0 & \text{for } r < a \\ +\infty & \text{for } r > a. \end{cases} \tag{2.1}$$

By using polar coordinates (r, θ), and assuming that the radial and angular parts of the wave functions are separable, i.e. $\psi(r, \theta) = \Theta(\theta)R(r)$, the Schrödinger equation can be written

$$-\frac{\hbar^2}{2m^*}\left(\frac{\partial^2}{\partial^2 r} + \frac{1}{r}\frac{\partial}{\partial r} + \frac{1}{r^2}\frac{\partial^2}{\partial \theta^2}\right) R(r)\Theta(\theta) = ER(r)\Theta(\theta), \tag{2.2}$$

where m^* is the effective mass of the electron. The solutions (which can be found in e.g. references[229,231,232]) read, for $r < a$:

$$\Psi(r, \theta) = \frac{1}{\sqrt{2\pi}} e^{im\theta} J_m(z_{m,n} r/a) \tag{2.3}$$

and the energy is given by

$$E_{m,n} = \frac{\hbar^2}{2m^* a^2} z_{m,n}^2. \tag{2.4}$$

The function $e^{im\theta}$ describes the angular dependence of the wave function, and the allowed values of m are $0, \pm 1, \pm 2, ...$
$J_m(z_{m,n} r/a)$ are the radial eigenfunctions. They are Bessel functions of order m. The n^{th} root of the Bessel function of order m is denoted $z_{m,n}$. These roots satisfy the boundary condition that the wave function must be 0 at the edges of the infinite well. The wave functions and energy levels are presented in figure 2.3b and c respectively. With this, we may now compare the 2D circular well to 3D atoms.

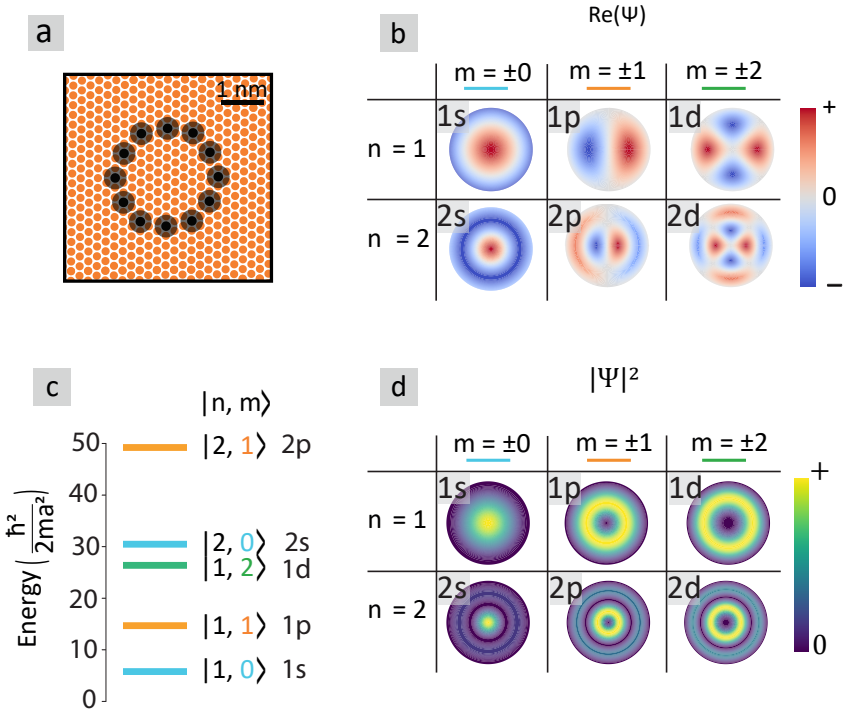

▲ Figure 2.3: **Artificial atoms in two dimensions.** (a) An artificial atom confined by a ring of CO molecules (black) placed on specific positions on a Cu(111) surface (orange). (b) Analytical calculation of the real part of the wave functions labelled by their radial quantum number n and the angular momentum quantum number m. (c) Energy scheme of the lowest energy levels labelled by (n, m). The analogous atomic orbital character (s, p, d) is listed next to each level. (d) The squared modulus of the wave functions providing spatial maps of electron probability density.

2.6.2 Comparison of the 2D artificial atom to the hydrogen atom

Some similarities and differences between the 2D circular well and the hydrogen atom are listed below, with reference to the equations and quantum numbers given above.

- The hydrogen atom introduces an extra degree of freedom compared to the 2D circular well. This ultimately leads to the existence of the quantum num-

ber ℓ, related to associated Legendre polynomials. The Legendre polynomials are not required for the solution to the 2D circular well, thus neither is ℓ.

- n, declared above for the 2D circular well, is a quantum number that is analogous to the principal quantum number in the hydrogen atom, also typically referred to as n.

- The number of radial nodes in the case of the hydrogen atomic orbitals is $n - \ell - 1$. In the case of the 2D circular well, the number of radial nodes is simply $n - 1$. The radial nodes in 2D are visible in the the real part of the wave functions, see figure 2.3b.

- m, as given above for the 2D circular well, is a quantum number that defines the angular momentum of the system. It directly corresponds to the magnetic quantum number (sometimes called the z-component angular momentum quantum number[232]) that one may derive from analytical treatment of the hydrogen atom, m_ℓ. In fact, the angular component of the wave function about the z-axis of the hydrogen atom is described by the very same equation as for the angular component of the wave function in 2D: $e^{im\phi}$.

- The total angular momentum in the case of the 2D circular well is given by $L = m\hbar$. In the hydrogen atom, the total angular momentum is $L = \sqrt{\ell(\ell+1)}\hbar$. The total angular momentum in 2D is the same as the z-component of angular momentum in 3D.

- The number of nodal lines that bisect the real part of the 2D circular well wave functions is given by m, which can be seen in figure 2.3b. In the case of the hydrogen atomic orbitals, there are ℓ nodal planes.

In light of the above points, we adopt the same notation used to label the orbitals of atoms, except s, p, d, f is determined by m rather than ℓ. Thus, to describe a state in the 2D circular well, we write the value of n and follow it with s, p, d, f to denote states with $m = 0, 1, 2, 3$. Figure 2.3 shows examples of labelled orbitals. In figure 2.3b and d, the columns of increasing m parallel s, p and d orbitals in atoms, while the rows correspond to increasing n.
A few extra points can be made in the comparison between the 2D circular well and hydrogen:

- To find the radial component of the wave function, Bessel functions are used in 2D, while associated Laguerre polynomials are used for the hydrogen atom. For the hydrogen atom, the associated Laguerre polynomials give outputs dependent on quantum numbers n and ℓ, and impose a restriction on ℓ such that $\ell < n$. Furthermore, in calculating the angular part of the wave function in full for the 3D case, associated Legendre polynomials are used, which in turn place another restriction such that $|m_\ell| \leq \ell$. The Bessel function used

in the 2D case places none of its own restrictions on the angular momentum quantum number (and the solution to the angular part of the wave function only requires that m is an integer), thus e.g. $1p$ states are possible in 2D but not in 3D.

- The energy eigenvalue for the hydrogen atom does not depend on angular momentum (only n), while the energy for the 2D circular well depends on both n and m (via the roots of the Bessel function).

- The degeneracy of each energy level in the hydrogen atom is n^2. In 2D, each energy level is two-fold degenerate (corresponding to the $+m$ and $-m$ states), except for the ground state which is non-degenerate ($m = 0$).

- For both the hydrogen atom and the 2D circular well, the wave functions are complex except when $m = 0$. To formulate the familiar $2p_x$ and $2p_y$ orbitals of hydrogen (commonly visualised as lobes aligned along the x and y axes), a linear combination of $2p_{m=+1}$ and $2p_{m=-1}$ orbitals are taken. This results in real-valued p_x and p_y orbitals. The same procedure can be performed for the 2D states, where the angular components would be $\frac{2}{\sqrt{2}}\cos\theta$ and $\frac{2}{\sqrt{2}}\sin\theta$, corresponding to p_x and p_y orbitals, respectively. The real parts of the p wave functions shown in figure 2.3 qualitatively correspond to the p_x state.

2.6.3 Other shapes of artificial atoms

The orbitals of an artificial atom depends on the shape, dimension and symmetry of the enclosure. In 2D, the closest analogue to a real 3D atom is the circular artificial atom, as presented here. The appearance of the orbitals are easy to relate to the 3D case, particularly because a particle in a circular well has a well-defined angular momentum. However, it is not strictly necessary to use circular artificial atoms - it is easier to use a shape that can be tessellated to fill a plane with no gaps to produce a lattice. Such shapes would still have discrete energy levels and quantum numbers, however, the angular momentum would not be well-defined, so s, p, d, f notation may not apply. Despite this, a similar description could be used based on the appearance of the wave function. For example, a square-shaped artificial atom[233,234] exhibits a central peak in its wave function for the lowest energy (s-like state), a nodal line for the second lowest energy (p-like state), and two nodal lines for the third lowest energy (d-like state), see chapter 4. Non-circular 2D artificial atoms have been used as the basis for all lattices realised on the CO/Cu(111) platform to date (most of which are described in this chapter). Notably, we show how p-like orbitals have been utilised in artificial graphene (section 8) and how the degeneracy was lifted between p_x and p_y like orbitals in the Lieb lattice (section 9).

2.6.4 Artificial atoms and molecules fabricated with the CO/Cu(111) platform: an example

Artificial atom

We now present and discuss a circular artificial atom created on a Cu(111) surface, see figure 2.4. Figure 2.4a shows the schematic of a circular corral that was constructed. $\frac{dI}{dV}$ vs. V (corresponding to the LDOS) spectra were acquired at the positions marked at the centre and close to the boundary, and are plotted in figure 2.4b. The spectrum taken in the centre shows a resonance at -0.17 V, while the one taken off-centre shows an additional peak at 0.21 V. The maps of $\frac{dI}{dV}(x, y)$ (figure 2.4c) show that the two resonances correspond to the $(n = 1, m = 0)$, and $(n = 1, m = -1)$ and $(n = 1, m = 1)$ states. The images are reminiscent of the probability density of $s-$, and degenerate $p-$orbitals, respectively. Consequently, these states will be referred to as $s-$like and $p-$like states.

Artificial molecule

The analogy of a quantum corral to an atom can be extended further - two corrals can be coupled together to form a dimer, resulting in an interaction between the on-site orbitals and the formation of bonding and antibonding molecular orbitals. In a dimer, there is an increased probability density in between the two nuclei at the energy of the bonding state. The reverse is true for the antibonding orbital; in this case a node exists between the corrals. The energies of bonding and antibonding orbitals are observed by measuring $\frac{dI}{dV}$ spectra at different positions in the artificial dimer, see figure 2.4d for the schematic with measurement positions. Because of the spatial extension of the molecular orbitals, a spectrum taken in between two sites only shows one peak (-0.24 V in the blue curve, figure 2.4e, attributable to the bonding orbital. The antibonding state is located at -0.14 V. Figure 2.4f shows differential conductance maps at the energies of the bonding and anti-bonding orbitals, respectively. This concept of coupling quantum corrals is the basis behind the construction of artificial electronic lattices.

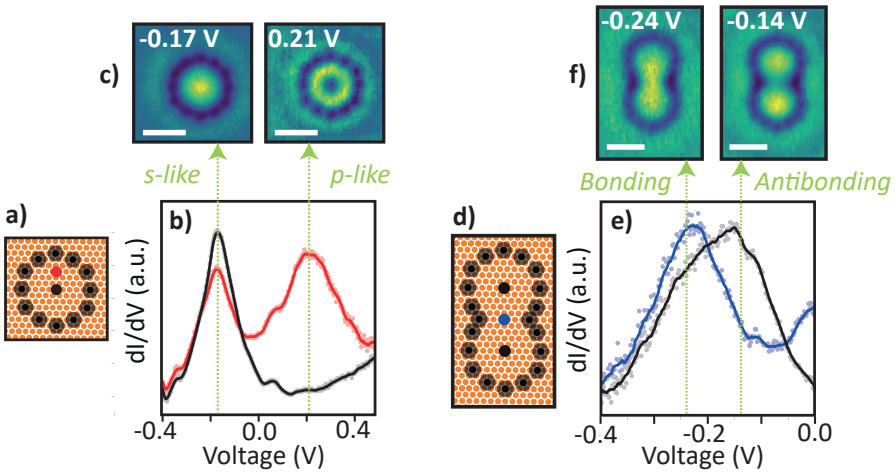

▲ Figure 2.4: **Quantum corrals behaving as 2D artificial atoms and molecules.**
(a) Scheme of the artificial atom and (d) artificial diatomic molecule. Black shaded dots represent CO molecules and orange dots represent the Cu(111) surface atoms. The positions on which the spectra were taken are marked in (a) black and red, and (d) black and blue.
(b,e) $\frac{dI}{dV}$ spectra, averaged over several measurements on each position, and divided by the average bare Cu(111) spectrum acquired with the same tip state. The light-coloured dots represent this data. The continuous lines represent the moving average.
(c) Differential conductance maps of the artificial atom showing the $m = 0$, $n = 1$, ($1s$) and the $m = 1$ or -1 (in-plane $1p$) states at -0.17 V and 0.21 V respectively. The spectra shown have been averaged over several measurements on the same (or equivalent) positions, and then divided by the average of many spectra on bare Cu (111).
(f) Differential conductance maps of the artificial dimer showing the bonding and antibonding combinations of two $1s$-orbitals at -0.24 V and -0.12 V respectively.

2.7 Simulation of the honeycomb lattice

A honeycomb lattice consists of two interpenetrated trigonal lattices (see figure 2.5) of one type of atomic sites. Its unit cell consists of two sites (A and B), thus a site of each trigonal sublattice. The coupling between nearest neighbor A and B sites in this geometry results in linear dispersion around the K, K' points of the Brillouin zone.[235] In the generic honeycomb system where each atomic site has s, p_x and p_y orbitals, several Dirac cones can be formed by facilitating $s - s$ coupling, $p - p$ coupling, etc, provided that mixing of the orbitals does not occur.[62,236] The

two orthogonal (p_x, p_y) orbitals cannot form conventional bonding – antibonding combinations; instead their interaction gives rise to complex interference patterns. As a result, the four in-plane p bands consist of a non-dispersive flat band, followed by two dispersive bands forming a Dirac cone at higher energy, followed by another flat band (see figure 2.6f). Since the kinetic energy does not vary with momentum in the flat bands, the main deviation in energy originates from interactions. It has been predicted that this will lead to new quantum phases, such as the p band quantum (spin) Hall effect, unconventional superconductivity, and Wigner crystals.[62] The physics of in-plane p-orbitals has been studied with ultracold atoms in optical lattices,[236–238] light in photonic systems,[239] and exciton-polaritons in semiconductor pillar arrays.[127,143] Natural atomic monolayer materials with honeycomb geometry include graphene, silicene, and germanene.[235,240–247] In graphene, the most studied electronic honeycomb lattice, the s- and in-plane p_x, p_y orbitals of the carbon atoms hybridize and form sp_2 electronic bands, the lower one being completely filled.[235] This filled band leads to a strong in-plane bonding between the carbon atoms, giving graphene its mechanical strength. However, this band is far below the Fermi-level and thus not electronically active. The remaining p_z orbitals (perpendicular to the graphene plane) form π bonds, resulting in two bands touching at the (K, K') Dirac points at which the Fermi energy is situated. The linear energy-wave vector dispersion (Dirac cone) around the (K, K') points is responsible for the high mobility of electrons in graphene. Solid-state electronic honeycomb systems can be realized in two-dimensional semiconductor materials by lithographic etching, giving access to genuine honeycomb semiconductors, hosting Dirac-type electrons and holes.[10,30–34,36,37,248–255] Alternatively, the self-assembly and epitaxial connection of nanocrystals at an interface has resulted in honeycomb semiconductors of II-VI materials.[256–260] The creation of 2D semiconductors with honeycomb nanogeometry with minimum disorder and the study of the opto-electronic properties is currently performed in several groups worldwide. This will be discussed in the outlook section of this work. First, the creation of electronic honeycomb systems will be described in detail.

2.7.1 Molecular graphene

An artificial honeycomb lattice engineered by manipulation of CO molecules on a Cu(111) surface in a scanning tunneling microscope was reported in 2012 by the group of Manoharan.[7,10] In this work, the lattice was coined "molecular graphene". This seminal work revealed the potential of quantum simulations with artificial lattices prepared in a scanning tunneling microscope. First, a graphene-type honeycomb lattice with a single Dirac cone was created. Second, by changing the size of the artificial atomic sites, the intrinsic Fermi-level (at the Dirac point) could be changed; the connection between two domains with a different intrinsic Fermi-level results in electronic equilibrium, simulating a "p-n" junction. Third, the manuscript

demonstrated that the bond strength between artificial sites could be modulated by appropriate positioning of CO molecules (introducing a Kekulé texture). Finally, it was shown that artificial lattices allow simulation of axial strain. For graphene, triaxial strain is equivalent to applying a magnetic field.

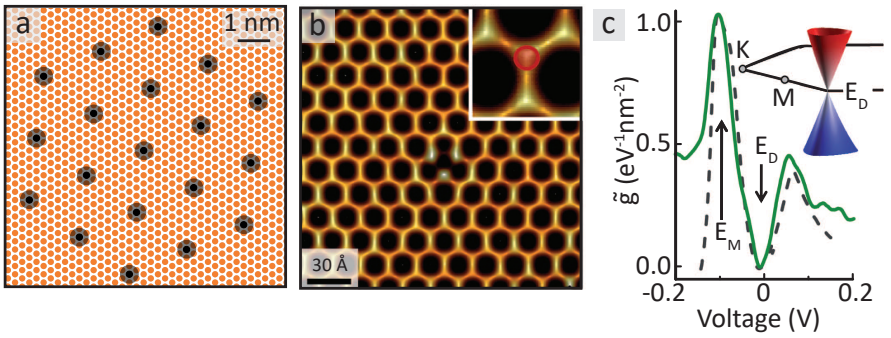

▲ Figure 2.5: **Design and realization of the first quantum simulation of a honeycomb lattice, "molecular graphene".** (a) Schematic of CO molecules (black; shaded area representing the approximate size as imaged in STM) atop the Cu(111) surface atoms (orange), as formulated in.[7] (b) STM topograph of the artificial graphene lattice. The LDOS is higher between CO molecules, which appear as black circles in the scan.[7] (c) Differential conductance as a function of bias (green line) with a tight-binding fit (dashed black line); The Dirac cone in momentum space is shown inset, calculated with the fit tight-binding parameters.[7] The dip in LDOS labelled E_D corresponds to the centre of the Dirac cone.

Figure 2.5a presents the design used by the Manoharan group; a hexagonal array of single CO scatterers (black dots) was prepared by atomic manipulation; this results in lattice vectors of 1.92 nm, considerably larger than in real graphene (0.246 nm).[235] Figure 2.5b shows a scanning tunneling microscopy image, in which a honeycomb network can clearly be seen. Scanning tunneling spectroscopy revealed the local density of states (LDOS) corresponding to a single Dirac cone (indicated by E_D). The width between the two maxima around the Dirac point, i.e. the two M-points is 180 meV, resulting in a hopping value of about 90 meV (ignoring orbital overlap). From the gradient of the linear dispersion $E(k) = \hbar v_F k$, the group velocity (Fermi velocity) of the electrons is found to be $2.5 \times 10^5 ms^{-1}$, considerably smaller than in real graphene. Perhaps the most compelling highlight of this work is the deformation of the lattice to simulate triaxial strain, and thereby a pseudo-magnetic field (gauge field) up to 60 Tesla. By such a field, a 0th order Landau state emerges on the A sites, while the B sites exhibit a Landau gap that gives

mass (widens the gap at the Dirac point) to the Dirac electrons with pseudospin B.

2.8 Simulation of the generic electronic honeycomb lattice with separated s- and p-orbital bands

Similar to the situation in real graphene, there is significant hybridization between s - and in-plane p-orbitals in the molecular graphene lattice shown in figure 2.6a.[261] To access the pure p-orbital physics, it is essential to increase the energy difference between s- and p-orbital bands, and to reduce next-nearest neighbor coupling. This can be done by tailoring the size of the artificial lattice sites, and by using "rosettes" of CO molecules instead on single CO molecules, respectively, see figure 2.6. Muffin-tin and tight-binding calculations predict a single Dirac cone for the lattice with single CO molecule scatterers, while a double ring rosette of CO molecules results in Dirac cones in both s- and p-orbital bands, as well as a (nearly) flat p-band. This suggests that such lattices can be used to study the in-plane p-orbital physics, unclouded by hybridization effects.
Figure 2.7a shows a scanning tunneling microscope image of the lattice shown in figure 2.6c, acquired with a Cu tip. The experimental and simulated LDOS spectra on the artificial lattice and bridge sites are presented in figure 2.7b; they agree well, indicating that the realized lattice indeed features the p-orbital band structure. Likewise, the experimental and simulated differential conductance maps agree well. The interaction of in-plane p-orbitals at the sites of a honeycomb lattice can best be described as orbital interference by geometric frustration.[62,236] Wannier-like eigenstates with the flat band energy can be constructed around each hexagon plaquette of artificial sites resulting in a local density of states on the bridge sites.[62] These results show that solid-state electronic honeycomb lattices can be designed in such a way that in-plane p-orbital physics fully emerges. The design is purely based on the lattice geometry and the degree of quantum confinement and inter-site coupling.

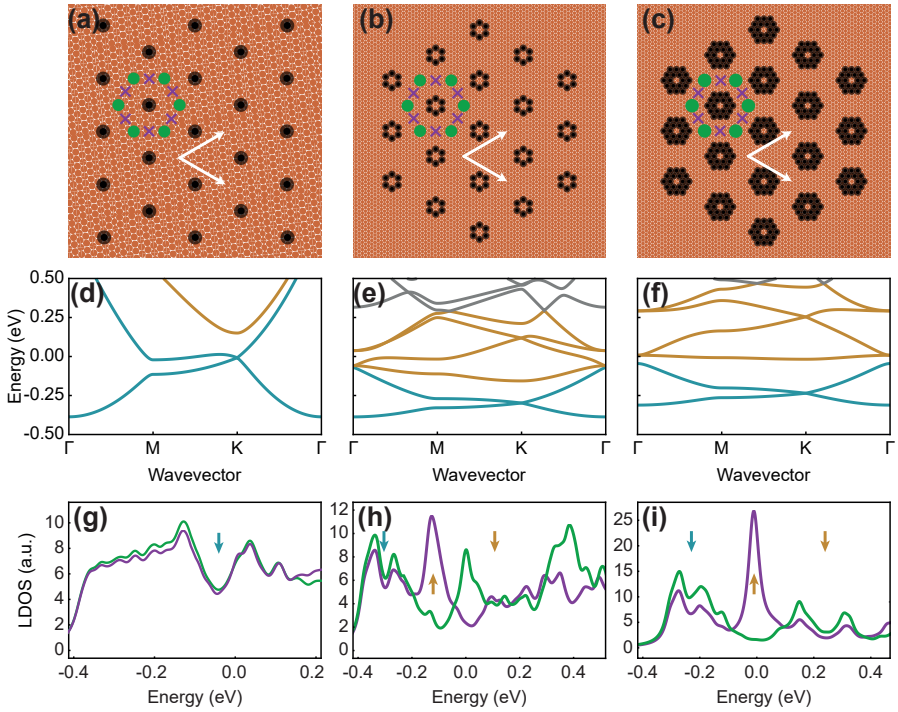

▲ Figure 2.6: **Designs for artificial atoms in a honeycomb lattice, corresponding band structures and LDOS spectra.** (a-c) Schemes of Cu(111) surface (orange) and the positions of the CO molecules (black) defining the on-site energies of the s-and p-orbitals and their inter-site coupling. The lattice sites are indicated in green, the bridge sites with purple crosses. (a) The lattice reported by Gomes *et al.*,[7] with a honeycomb lattice vector of 1.92 nm. (b) Lattice with single-ringed CO rosettes as scattering islands and a honeycomb lattice vector of 3.58 nm, corresponding to 14 Cu atoms, (c) lattice with double-ringed CO rosettes as scattering islands, the lattice vector is also 3.58 nm. (d-f) Corresponding band structures calculated by the muffin-tin approximation. The band structures for the designs (b) and (c) reflect (nearly) separated s (blue) and p (orange) orbital bands. (g-i) The LDOS for these three designs; green for the on-site positions, purple for the bridge positions between the sites. Blue arrows indicate the s-orbital Dirac point, orange arrows indicate the p-orbital flat band and the p-orbital Dirac point. The Gaussian broadening is 40 meV.

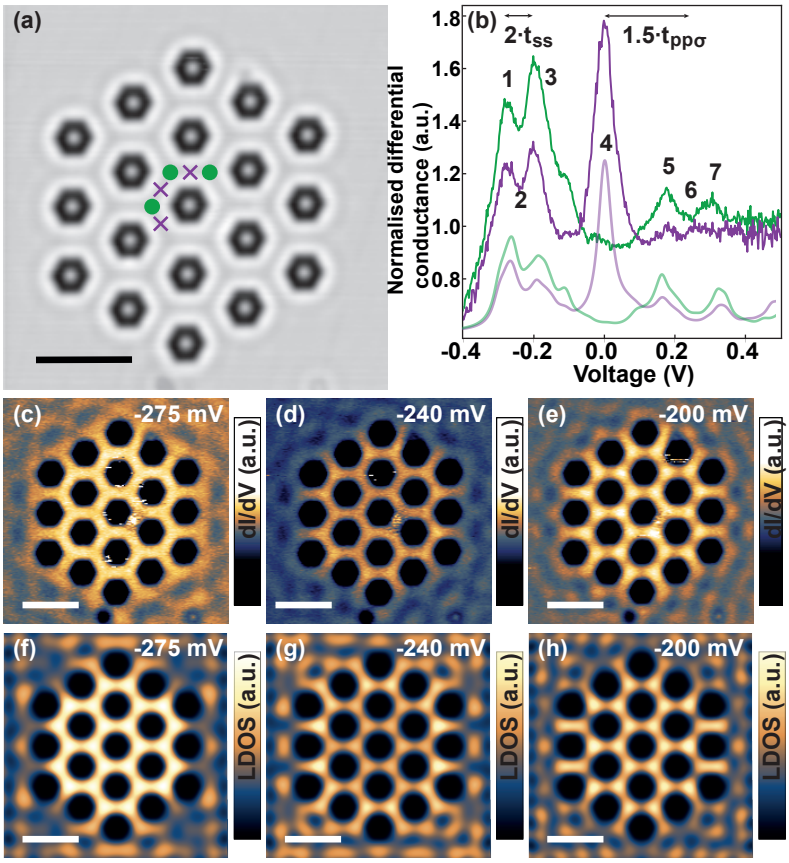

▲ Figure 2.7: **Experimental results obtained on the honeycomb lattice with the design shown in figure 2.6c.** (a) STM image of the lattice; the black hexagons are the double rosettes of electron-repelling CO molecules; the green dots indicate the lattice positions of the honeycomb lattice, the violet crosses indicate the bridge positions between the lattice sites. (b) Experimentally acquired LDOS(E) on the lattice positions and on the bridge sites; (1,2,3) reflect the first s-orbital Dirac cone, with 1,3 the M-points, and 2 the Dirac point; 4 shows the flat-band due to interference of in plane p-orbitals with high LDOS at the bridge sites; (5,6,7) shows the second Dirac cone due to the p-orbitals. (c,d) wave function maps at the energy of the flat-band showing the nearly zero electron probability on the lattice sites, and large probability on the bridge sites; (c) experimental LDOS(x, y) map; (d) muffin-tin calculation at the same energy. The black hexagons are the CO-rosettes.

2.9 Simulation of an electronic Lieb lattice

The geometry of the Lieb lattice is well-known from the AX_2 planes in the 3D ABX_3 perovskite structure, such as the superconducting CuO_2 planes in cuprate high-temperature superconductors,[262] but does not exist as such in a natural 2D material. It is thus valuable to perform an analogue quantum simulation of an electronic Lieb lattice. The Lieb lattice is a depleted square lattice, consisting of three (artificial) atoms per unit cell[262,263] (see figure 2.8a. The two edge sites (red) have two nearest neighbours and the corner sites (blue) connect to four nearest neighbours. The three-atom basis gives rise to three *s*-orbital bands (figure 2.8b; two bands converge to a Dirac cone at the Brillouin zone corners, which is intersected by a flat band). Similar to graphene, the photon-like linear dispersion in the Dirac cone leads to massless electrons which can propagate in the lattice at a constant velocity. On the other hand, the electrons in the flat band are entirely localized on the edge atomic sites of each unit cell. The realization of a flat band is particularly interesting for the investigation of electron-electron interactions,[264–267] the (fractional) quantum spin Hall effect[139,268] and superconductivity.[269] An optical equivalent of the Lieb lattice was theoretically proposed[118,270] and subsequently realized in bosonic and fermionic cold-atom lattices.[271,272] Additionally, photonic Lieb lattices have been realized and the band structures were mapped.[140,264,265,267,273,274] Only recently, exciton-polaritons were studied in a Lieb geometry.[127,275]

The electronic Lieb lattice has been realized via two approaches. Drost *et al.* manipulated chlorine vacancies in a chlorine monolayer on Cu(100),[21] the formation of these lattices was based on seminal work performed in the group of Otte.[98] It was shown that the vacancy states can couple to form a lattice. Scanning tunnelling spectroscopy and maps of a Lieb lattice with Cl-vacancies as artificial atoms corroborated the main characteristic features of the Lieb lattice. An advantage of this approach is that it allows the direct lattice to be patterned, in contrast to the inverse geometry required for the CO-on-Cu(111) platform. A disadvantage is that the on-site energy of the vacancy states is close to the Cl-conduction band, leading to a limited accessible energy range. As a consequence, the Dirac-band above the flat band and possible higher bands could not be resolved.

In our work,[230] the CO-on-Cu(111) platform was used. The Lieb lattice has a square-type geometry, which means that the lattice is not entirely commensurate with the underlying Cu(111). However, since the artificial atoms formed by CO molecules on top of Cu atoms comprises many Cu sites, good approximations to the Lieb lattice can be prepared, even on a hexagonal Cu(111) surface, see figure 2.8.[230,262,263,276,277] Since the Lieb lattice has no dual lattice, the inverse lattice was defined using crosses of five CO molecules, as indicated in figure 2.8b. The unit cell was chosen such that the on-site energy was near the Fermi energy and the anisotropy of the C4-symmetric Lieb lattice on the triangular Cu(111)-background was minimized. Scanning tunnelling spectroscopy resolved the bottom and top Dirac bands (blue) and a

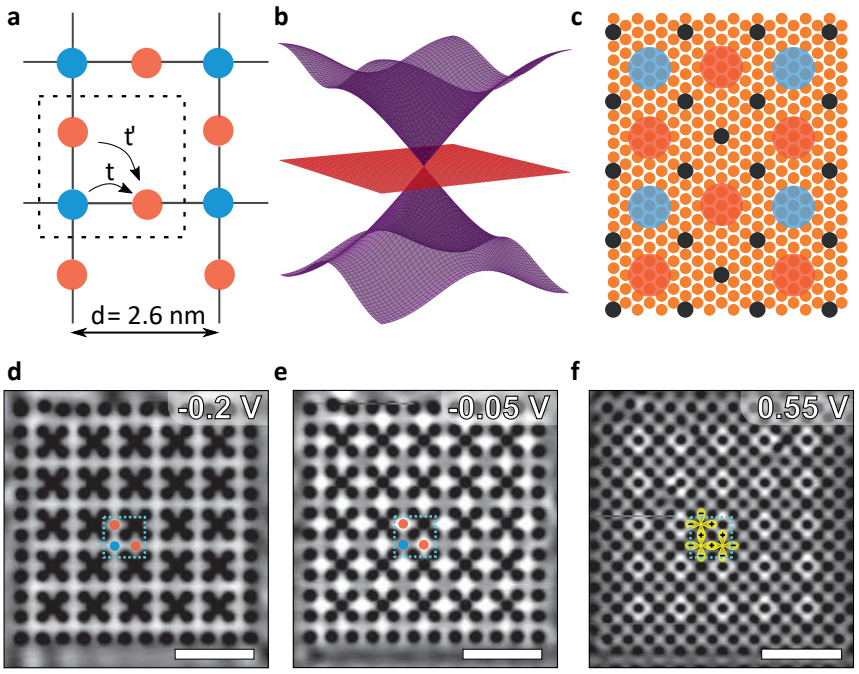

▲ Figure 2.8: **A simulation of the CO-on-Cu(111)-produced Lieb lattice** (a) Schematic of the Lieb lattice. The unit cell (contained in the dashed lines) contains two edge sites (red) and one corner site (blue). (b) The lowest three bands of the lattice, formed by s-orbitals. (c) Configuration of CO molecules (black) on Cu(111) (orange background) to corral the Cu surface-state electrons into the Lieb geometry. (d) Wave-function map at V = -0.2 V, corresponding to the energy of the lowest Dirac band, with high electron density at the corner states (e) Wave-function map at V = -0.05 V, the flat band energy, showing high electron density at the edge states of each unit cell. (f) Wave-function map at V = +0.55 V, showing the coupling of in-plane p-orbitals in the Lieb lattice.

nearly-flat band (red), see figure 2.8c. Furthermore, LDOS maps showed the localization of the Dirac bands on both the corner and edge sites (figure 2.8d) and the nearly-flat band only on the edge sites (figure 2.8e). The middle, nearly-flat band had acquired a dispersion due to a substantial next-nearest-neighbour hopping and coupling with higher-energy bands. At energies above these s-orbital bands, higher-orbital bands were observed (see figure 2.8f). This approach thus allows for the re-

alization and characterization of a large range of energy bands, as long as the inverse geometry of the lattice can be defined on the triangular Cu(111) background. The C4-symmetric Lieb lattice is a suitable candidate to describe p-orbitals in a convenient p_x- and p_y-orbital basis. The realization of p-orbital bands has long been established in cold-atom and lattices.[216,278] In addition, p-orbital honeycomb and Lieb lattices were realized in photonic and exciton-polariton lattices recently.[127,239,275] The first engineered p-orbital bands in artificial electronic lattices were presented in the p-orbital Lieb-like lattice.[279] Motivated by the higher-energy bands observed in the initial Lieb lattice, the artificial-atom sites were enlarged to decrease the on-site energy and thus shift the p-orbitals down to the appropriate energy range $-0.45 < E < 0.5eV$. LDOS maps displayed nodes on the artificial-atom sites and a finite DOS between the sites, characteristic for the low p_x- and p_y-orbital bands. In addition, the on-site energies of the p_x- and p_y-orbitals were tuned independently by creating an asymmetric Lieb lattice. This allowed to lift the spectral degeneracy of the p_x- and p_y-orbital bands. The work on s- and p-orbitals in the Lieb lattice established that the orbital degree of freedom is among the parameters that can be tuned in electronic lattices realized using CO on Cu(111). However, the four p-orbital bands exhibited a significant spectral overlap and were relatively close to the s-orbital bands. The previous section discussed how the p-orbital band structure was finetuned further and separated from the s-orbital bands for the example of the honeycomb lattice.

2.10 Simulation of aperiodic two-dimensional systems

The presence of long-range order and translational symmetry enables the use of periodic boundary conditions in electronic structure calculations. As such, it underpins our understanding of the electronic structure of materials. However, not all materials have translational symmetry. Notable examples are (i) amorphous materials, i.e. materials with no long range order, (ii) quasicrystals, which are aperiodic tilings built up using two or more well-defined unit cells, and (iii) fractals, patterns that are often described as self-similar on different length scales. Figure 2.9 shows an example of a quasicrystal (Penrose tiling) and fractal (Sierpinski triangle). Both types of structure are difficult to study. Many quasicrystals, experimentally discovered in the early 1980's,[280,281] were synthesized in the laboratory and are thermodynamically unstable. The few quasicrystals that have been found in nature have been formed in outer space.[282] Even though fractals are pervasive on the macroscopic scale - Romanesco broccoli, the cardiovascular system and coast lines are well-known examples - no naturally occurring geometric quantum fractals have been identified. Molecular self-assembly can be used to form fractals in a bottom-up fashion.[283] However, the coupling between the building blocks is too weak to result in a true electronic fractal. The ability to position adsorbates with atomic scale precision enables the formation of well-defined electronic quasicrystals

and fractals, as shown below. Synthetic quasicrystals have also been realized using cold atom gases and photonics.[284–286]

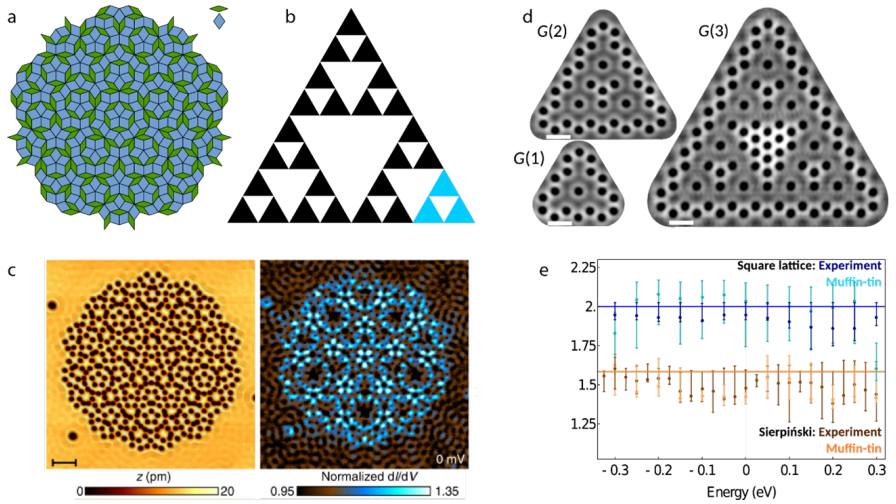

▲ Figure 2.9: **Aperiodic lattices created using the CO/Cu(111) platform** (a) Penrose tiling, built using two rhombi, indicated in blue and green. (b) Third generation Sierpinski triangle. The first generation is shown in light blue. (c) STM image (left) of an arrangement of CO molecules (black) that leads to a Penrose tiling for the surface-state electrons. The corresponding normalized $\frac{dI}{dV}$ map (right) shows that the LDOS also exhibits a Penrose geometry. Scale bar: 5 nm. (d) STM images of the first three generations of the Sierpinski triangle, indicated by G(1), G(2) and G(3), respectively. Scale bar: 2nm. (e) Plot of the dimension of the electronic states of a G(3) Sierpinski lattice as determined by applying box-counting to experimental $\frac{dI}{dV}$ maps and muffin-tin calculations. For reference, experimental and calculated data on a square lattice are also shown.

2.10.1 Formation of electronic quasicrystals and fractals

In 2017, Collins *et al* used the CO/Cu(111) platform to create an electronic Penrose tiling, see figure 2.9c.[287] Energy resolved maps of the local density of states revealed that the wave functions have the same symmetry as the geometric structure to which the electrons are confined. A Fourier analysis of these real-space differential conductance maps showed that the energy of the states is related to the local vertex structure of the quasicrystal. We have used the same CO/Cu(111) platform to create a geometric electronic fractal.[288] The light blue triangle in figure 2.9b shows the first generation of the Sierpinski triangle. By repeating this unit, two

additional generations of the Sierpinski fractal were realized, see figure 2.9d. The Hausdorff dimension of a Sierpinski triangle is $\log 3/\log 2 \approx 1.58$. The dimension of the electronic wave functions can be determined by analysing the differential conductance maps in segments in a process known as the box-counting method. Figure 2.9e shows the dimension of the electronic Sierpinski triangle and square lattice at different energies. The dimension of the electronic fractal is close to the expected value of 1.58 for all energies, while that of the square lattice is close to 2. This is consistent with the observation for the synthetic Penrose tiling that the Cu(111) surface state electrons are confined to the geometric structure defined by the CO molecules.

2.11 Beyond simulations: Two-dimensional semiconductors

The topics presented thus far concern quantum simulators produced on a site-by-site basis with STM. Although this allows one to fabricate and investigate materials with unexplored 2D geometries, materials built this way cannot feasibly be used in technology. The principles derived from these model studies could however be translated to systems that have application potential. In this section, we discuss semiconductors fabricated with pre-determined geometry, which are scalable and have real technological applications.

2.11.1 Brief history

In semiconductors, the chemical potential of free conduction band electrons (or valence band holes) can be varied with respect to the energy levels in the system. This is possible either by incorporating specific non-isovalent impurity atoms on specific atomic positions in the lattice, or by applying an external electric field, thus electrostatic doping or gating. The latter requires a capacitor structure between the semiconductor of interest and a metal electrode. In a more advanced form, electrostatic gating leads to complementary metal-oxide-semiconductor (CMOS) technology in transistor devices. More recently, electrolyte gating has also been applied. The ability to grow ultra-pure Si crystals, seed them with electron-donating or electron-accepting dopants and change the chemical potential has enabled our current information society, known as the "silicon age".
In parallel with the development of CMOS technology based on bulk silicon, low-dimensional, particularly 2D, semiconductors were developed and investigated.[289] The electrons in 2D semiconductors corresponds to Bloch type waves in the two lateral x, y directions, and are confined as standing waves in the short z direction. 2D semiconductor crystals, also known as quantum wells, can be grown on substrates and incorporated into devices by gas-phase deposition techniques such as chemical vapor deposition, molecular beam epitaxy, pulsed layer deposition, and methods derived from these. Two-dimensional semiconductors have boosted the opto-electronic

industry. In addition, fundamental research on electron gases in 2D semiconductors has resulted in paradigm-shifting breakthroughs in solid state physics. In 1980, the quantum Hall phenomenon was discovered,[23,290–292] now established as the first topological electronic band structure effect in the solid state. Around 1984, the fractional quantum spin Hall effect was discovered and analyzed,.[24,293–295] Further theoretical and experimental research revealed the existence of composite electronic quasi-particles, some of them with exchange statistics reminiscent of neither fermions nor bosons: non-Abelian anyons.

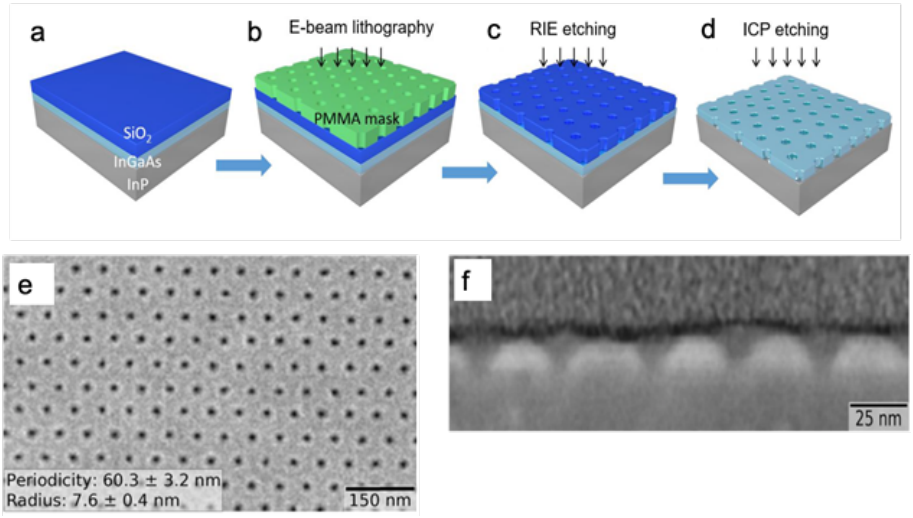

▲ Figure 2.10: **Fabrication of 2D InGaAs semiconductor with a nanoscale honeycomb geometry** (a-d) the consecutive steps in the nano-lithography procedure, with (a) growth of silica and PMMA layers on top of the InGaAS quantum well, after which (in (b) electron beam lithography is used to write a hexagonal periodic pattern in the PMMA. (c) presents the reactive ion etching to transfer the pattern as hole array in the silica layer, and (d) shows the inductive coupled plasma etching to transfer the hole pattern from the silica into the InGaAs layer. (e) SEM image of a honeycomb InGaAS crystal with a periodicity of 60 nm, (f) SEM cross section of the conical holes with periodicity of 39 nm

Another step in this field, more related to the contents of this review, was to modulate the lateral potential experienced by the electrons in a 2D semiconductor in a periodic way. The modulating potential creates a potential on the 100 nm scale superimposed on the atomic potential of the lattice. This superimposed potential results in the formation of electronic mini-bands and thus provides a powerful path-

way to alter the electronic band structure of well-known semiconductor materials by geometry. Technically, this is achieved with electron beam lithography; a periodic array of metal gates can be fabricated that exerts a repulsive or attractive potential, forcing the electrons to live in e.g. a honeycomb superlattice. The magnitude of the translation vectors is between 150 and 100 nm.[28,251] Alternatively, an array of nanoscale holes in a 2D semiconductor crystal can be fabricated,[248,250] resulting in a more robust honeycomb potential, also allowing for smaller lattice vectors. This latter method and the resulting 2D semiconductor with a honeycomb geometry with translation vector magnitudes of 40-60 nm is presented in figure 2.10. A much later development came from the field of colloidal nanoscience: self-assembly and oriented attachment of PbSe nanocrystals resulted in two-dimensional semiconductors with square or hexagonal arrays of nanovoids; the latter system is an atomically coherent semiconductor with a honeycomb geometry.[256,257] The advantage of nanocrystal assembly is the much smaller period in the range of 5-10 nm, resulting in broader, i.e. more dispersive electronic bands. Nanolithography for periodic superlattices in semiconductors is better established and applicable to more materials.

2.11.2 Prospects for semiconductors with massless Dirac carriers

Strong evidence for the existence of massless Dirac electrons in 2D honeycomb semiconductors has not yet been provided. The modulation of the effect of the arrays of metallic gates in the region of the electron gas is rather weak and is estimated to be in the 10 meV range. Moreover, the translation vectors have magnitudes in the 100 nm range, resulting in Dirac cones with a weak energy-wave vector dispersion. It is also clear that detection of the local density of states and energy-resolved wave function mapping with scanning tunneling microscopy and spectroscopy can provide more direct evidence for a Dirac-type band structures than non-local methods, especially in the early phases of the research and development.

Looking to the future of this field, it is worth mentioning that modern lithographic techniques and state-of-the art templating with block co-polymers allow the preparation of III-V semiconductors with a honeycomb periodicity in the 30 nm range. (see figure 2.10). This automatically results in more dispersive Dirac cones, now over an energy scale in the tens of meV. Furthermore, self-assembled nanocrystal honeycomb structures are predicted to have Dirac cones with widths in the 100 meV range, provided that the nanocrystal sites are well coupled.[36] This opens new perspectives for the creation of semiconductors in which electron and/or hole excitations are robust massless Dirac carriers. Understanding that intrinsic spin-orbit coupling is strong in these systems, flawless honeycomb semiconductors with small periodicity open an entire new materials field in which the band structure can be modulated by the nanoscale geometry, interactions and spin-orbit coupling.[37,92] Strong spin-orbit coupling could open topological gaps in the 30 meV range, offer-

ing quantum spin Hall edge states for technology under affordable conditions.

CHAPTER 3

STM IMAGE RECOGNITION USING NEURAL NETWORKS

This chapter was written for this thesis. Partially based on:
Scanning tunneling state recognition with multi-class neural network ensembles.
O. Gordon, P. D'Hondt, L. Knijff, S. E. Freeney, F. Junqueira, P. Moriarty, and I. Swart.
Review of Scientific Instruments 90, 103704 (2019)

3.1 Introduction

During this thesis, we describe moving atoms on the nanoscale. Mostly, this refers to moving atoms on the surface. The ultimate goal of this chapter involves reconfiguring atoms at the tip apex.
An atomic resolution scanning tunneling microscopy (STM) image can only be obtained if one atom at the tip apex is closer to the surface than any other atom by enough of a margin. Usually, during experiments, the tip is conditioned in-situ by applying voltage pulses between tip and sample or, if the surface is clean and conductive, by deliberately pushing the tip into the surface. During either of these processes, atoms at the tip apex reconfigure in an unknown fashion until the user (so far a human) is satisfied with the image resolution. However, obtaining a suitably sharp tip is often tedious and time consuming. From a brief survey of a few scanning probe microscopists, it can be estimated that roughly 30% to 40% of measurement time is dedicated to tip conditioning.
This is substantial, both on a personal level (most scientists would probably prefer more mental stimulation from their research), and on a societal level (not only is scientific progress impeded by this inefficiency, but science is funded by the taxpayer, and a significant fraction of the cost of running an STM is dedicated to tip preparation). The process itself requires no high-level thinking - it is merely an algorithmic decision that depends on the output of an image recognition task. Since the advent[296,297] and recent renaissance[298] of artificial neural networks, it has become possible for these "simple" tasks to be automated. Particularly, convolutional neural networks (CNNs) have been shown to be well equipped for image recognition tasks, because the convolutional layers act as automatic feature extractors that the network can learn from.[299] A few groups have made progress in this direction in recent years, as we outline below. The end-goal is to have a fully-automatic inbuilt "tip-condition" button in SPM software that works on any surface, and that allows for more efficient use of measurement time, e.g. tip preparation tasks could be performed overnight.
This chapter discusses the use of a convolutional neural network as a tool to classify different tip states automatically. We do not go into detail about how neural networks work because plenty of excellent learning resources already exist,[299–302] but in addition to citations, the reader is referred to the glossary at the end of this chapter for important definitions.

3.2 In literature

The bulk of the work carried out for this project was performed in mid-2018, however, at the time of writing, there have since been a plethora of exciting new entries on the topic of SPM image recognition and automation to varying degrees. Below, we chronicle the existing literature, giving honorary mentions to reports on adjacent

topics:

- January 2011: Philip Moriarty's group at the University of Nottingham used genetic algorithms to modify scan parameters and change the tip apex until the desired scan resolution was achieved. It suffered too many limitations to be implemented as a robust artificial intelligence to control an SPM system.[303]

- June 2016: Saoirsé Freeney's master's thesis at the University of Nottingham[304] demonstrated image recognition using principal component analysis, a type of "traditional" machine learning. It trained on only 39 images and achieved 69% accuracy. Synthetic data was also generated algorithmically and through the use of convolution to simulate different tip states. At this time, neural networks were a nascent hot topic, showing promise for all kinds of image recognition tasks.

- May 2017: Without the use of any artificial image recognition at all, a group in Leiden reported that the the STM tip can be made symmetrical/sharp simply by dipping it gently into an Au(111) surface hundreds of times.[305]

- April 2018: The start of the project at Utrecht university that forms the subject of this chapter.

- May 2018: The first appearance of a neural network-based STM image classifier was documented by Wolkow's group at the University of Alberta, Canada. They tried and reported several techniques for image assessment of an H-passivated Si(100) surface. Their CNN method was of particular interest, as it yielded over 99% accuracy for correct identification of non-sharp tips.[306]

- March 2019: Synthetic training data was generated using Ising models to emulate SPM images on strongly correlated systems where complex patterns form. By doing this, they could answer the question of which physical model could describe a certain pattern formation, i.e. the ML algorithm could tell the underlying physics of the system. No manual labelling was required.[307]

- September 2019: A collaboration, (based on this project) between the University of Nottingham and Utrecht university tested several machine learning methods on H:Si(100), Au(111) and Cu(111) (the Au(111) dataset was acquired in Utrecht and is discussed in this chapter). This included the aforementioned CNN from the Alberta group, however, of the CNNs tested, this algorithm performed worst. This highlights the point that a model that works well for one dataset is not necessarily one-size-fits-all.[308]

- February 2020: Using a CNN and by generating probe-particle models, molecular structure and orientation could be predicted from an AFM scan.[309]

- February 2020: The Nottingham group tested a few methods to detect the state of a tip using incomplete scans. Of particular note was the long-term recurrent CNN[310] which surprisingly achieved better accuracy on a rolling window of scanlines than the group's earlier project making CNN predictions on full scans.[311]

- March 2020: An algorithm was developed by the Alberta group again, this time a CNN was used in tandem with image segmentation to recognise small defects and their positions in a "large" scan of H-Si(100). The algorithm then picks a clean area in the large scan and performs what they call "hydrogen/ scanning probe lithography" to automatically pattern the surface.[312]

- March 2020: A program, DeepSPM, was created by groups in Germany and Australia that fully automates the tip preparation process, from selecting scan regions to image classification (again using a CNN), and, most innovatively, using reinforcement learning to choose the best tip conditioning action.[313] The source code is available on GitHub.

- May 2020: The Nottingham group produce an engaging, complete review of literature related to artificial intelligence applied in the field of nanotechnology, specifically STM.

- June 2020: Artificial neural networks were trained to distinguish structure in electronic quantum matter, and, interestingly, performed well where humans would have difficulty.[314]

- August 2020: The Nottingham group produced Synthetic AFM images with a Monte Carlo algorithm. This data was used to train a CNN, which proceeded to correctly identify features in real AFM data that the group already had. This was done without the need to label the experimental dataset.[315]

- August 2020 (unpublished at the time of writing): A state of the art CNN architecture called U-Net[316] can provide predictions on a pixel-by-pixel basis, and performs well at image segmentation. The Nottingham group attempted numerous traditional automated segmentation procedures, and found that U-net outperformed them at segmentation of AFM images of gold nanoparticles on silicon.[317]

3.3 Methods

To train a neural network, a dataset of preferably several thousand examples should be gathered. This should be split into training, validation and testing data. For supervised learning, the training data should be further split into categories. The larger the dataset, typically the better the network performs. We outline below the

simple techniques that were applied to augment the original dataset to expand it by several orders.

3.3.1 Data gathering

A total of 2470 STM images of a clean Au(111) surface were acquired with a Scienta Omicron LT-STM system at approximately 4.5 K. The images were acquired in constant current mode. Each pixel in the raw data represents the extension of the piezo, or the height of the tip, in metres. The scan size was 30 nm × 30 nm, with a resolution of 150 pixels × 150 pixels. The bias voltage was 0.1 V and the current setpoint was 0.1 nA. A script was written to acquire the images automatically in a grid with spacing 30 nm in each of the x and y directions. All images in the dataset were acquired with the same settings.

3.3.2 Data preparation

A series of steps were taken to prepare the data for training.

- The first and last rows of each image array were removed. This was because no settle time was specified between the acquisition of images, so it was common to see a sudden adjustment of the tip height in the first few pixels of each image. The leftmost and rightmost columns of each image were also removed to maintain a square image of 148 pixels × 148 pixels.
- A plane subtraction was applied, with step-edges taken into account. (Procedure outlined in[318])
- The extension of the piezo could range between -100 nm and +100 nm, however, the extension holds no relevance to the scan, which only varies by up to a few nanometres. To eliminate any possible effects this could have, the values were centred at 0, by subtracting the average value of the scan from the scan itself.
- All values were converted to Ångströms so as not to have small values on the order e-9.
- To expand the dataset, the original images were rotated 90, 180 and 270 degrees, and flipped horizontally and vertically. The amount of data contained in each class was balanced as much as possible, so not all augmented data was used. It is generally the case that if there is class imbalance, a neural network is more likely to incorrectly classify specimens in the minority class compared to the majority class.[319]

After these procedures, 72 images were separated to be used as validation data. The remaining images were divided in a 75/25 split between training/testing data.

3.3.3 Image categories

The 2470 original images were categorised by two people (Nadine van der Heijden and Ingmar Swart) to divide the labour. The Au(111) surface exhibits a distinct herringbone reconstruction, which gives some visual clues as to what the tip apex could be like. Figure 3.1 shows six categories into which the images were divided. The categories are as follows:

- **Sharp**: These images were taken with a tip apex with a small radius, preferably a single atom.
- **Double**: The name of this category implies repeated features, which can be the case when there are two atoms at the tip apex. We also incorporate images taken with blunt tips into this category, as they have multiple atoms at the end of the tip as well. The contrast between light and dark (which represents difference in tip height) is low compared to a sharp image; compare sharp and double images in figure 3.1. A blunt tip cannot render small details as finely because it doesn't "fit" as well into the grooves of the surface.
- **Unstable**: These images exhibit evidence that the tip has undergone a change at its apex, resulting in a sudden change in contrast. This can range from several pixels up to a "semi-permanent" change.
- **Step country**: This refers to a location that appears to have many step edges. It could either indicate a double/multiple tip, or the surface could genuinely have many steps.
- **Bad country**: Sometimes the surface isn't flat. When these areas are imaged, usually cloudy, lumpy structures are observed. We reserve images such as this for bad country.
- **Rubbish**: This is like an extreme form of the unstable category, but where nothing of the underlying surface can be discerned.

The number of images in each category after augmentation is listed in table 3.1

3.3.4 Network structure

We made use of an adapted VGG-16 network[320] on the basis that this architecture performs well for image recognition tasks (VGG achieved top results for image classification in the ImageNet Large Scale Visual Recognition Challenge of 2014[321]). The VGG-16 architecture performs well for large-scale image recognition because of its depth (16 layers) and because of the fact it uses small convolution kernels of size 3×3, which can capture fine details (and is the smallest that can still convey the sense of up/down/left/right). However, we found that using 16 layers resulted

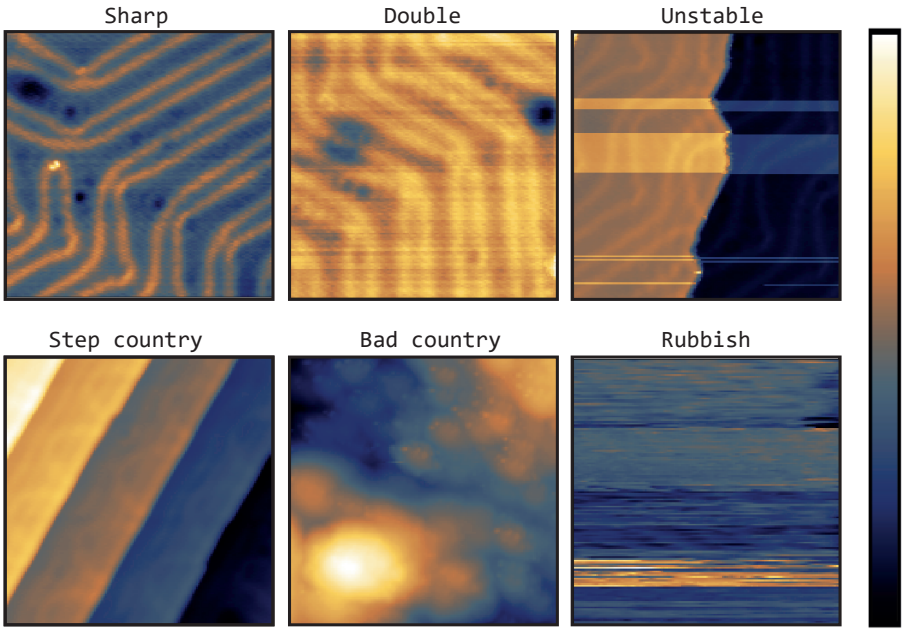

▲ Figure 3.1: Example STM scans of Au(111) from the six categories into which the data was classified. Each image is of size 30 nm × 30 nm and the colour scale is given on the right.

Class	Training data	Testing data(%)	Validation data
Sharp	1743	579	72
Double	1627	521	72
Unstable	3242	1054	72
Step country	1698	612	72
Bad country	379	137	72
Rubbish	2102	694	72
Total	10791	3597	432

Table 3.1: The number of images, post-augmentation, that the networks were trained on.

in overfitting, so the number of layers was reduced to 12. Note that the number of layers here refers to only those with associated weights. Figure 3.2 details the network architecture.

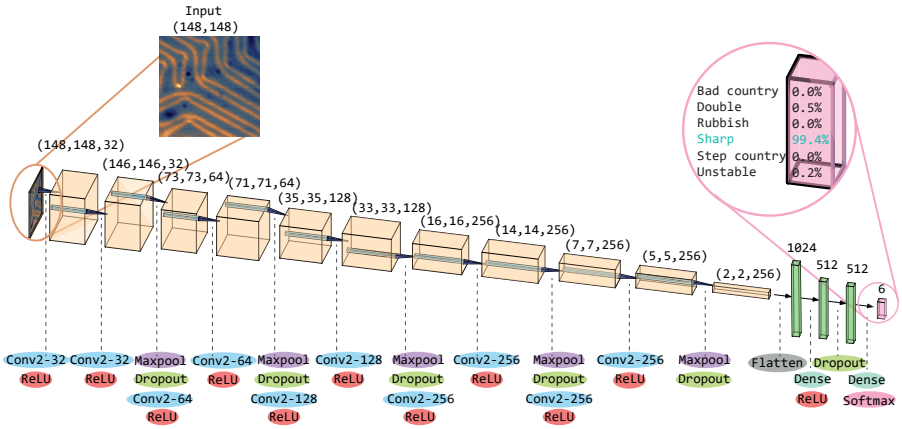

▲ Figure 3.2: The network used for training, based on the VGG architecture. The three dimensional blocks represent the output volumes from each prior operation, with dimensions given. The exact operations performed are specified below the arrows, and can be read in order top - bottom, left - right. An example is given of the output of the network (pink block) for a given input image. The probability distribution given by the network shows that it considers this particular image sharp.

Filters

The convolution filters were of size 3×3 with a stride of (1, 1) (as in the original design of the VGG network). The max pooling filters were of size 2×2, with a stride of (2, 2). Zero-padding of 1 pixel was applied. For this combination of filter size, image size, stride and padding, the spatial resolution after a convolution operation is preserved.[301]

Software and hardware

253 networks in total were trained using a Nvidia Geforce 1080 Ti GPU, using various hyperparameter combinations. We used Python with Keras 2.1.5, in tandem with TensorFlow 1.7.0.

Parameters

Adam was used as the optimizer.[322] The optimum learning rate was 0.0005, with the momentum set to 0.9 and the "learning deceleration" set to 0.999. We used ReLU as the activation function, for its known efficiency and efficacy. The networks were trained with up to 300 epochs, although there was no improvement in the network accuracy after approximately 175 epochs. Figure 3.3 shows the decline of the classification error as the number of epochs increases for one such network in the final ensemble.

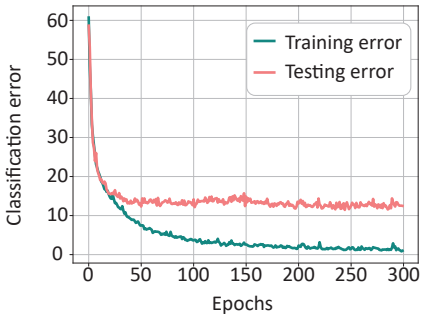

▲ Figure 3.3: The classification error vs number of epochs for one network in the final ensemble.

Dropout was applied after layers 2 and 4 at a rate of 0.25, layers 6 and 8 at a rate of 0.4, layer 10 at a rate of 0.45 and layer 11 at a rate of 0.5. This is visualised in figure 3.2
A batch size of 128 was used, which was the largest power of two that could be contained in RAM.

3.4 Results and discussion

3.4.1 Ensembles

To increase accuracy by a few percentage points, it is common to use the average prediction of an ensemble of networks.[323] A preliminary check was done to gauge how many networks should be used for the best performance. Eight ensembles of random networks were checked against validation data. The average recall (on validation data) is shown in figure 3.4 as a function of number of networks.
Compared to a single network, an ensemble of 5 networks enjoys a 3.5% increase in recall. There is a further increase of less than 1% as the number of networks in

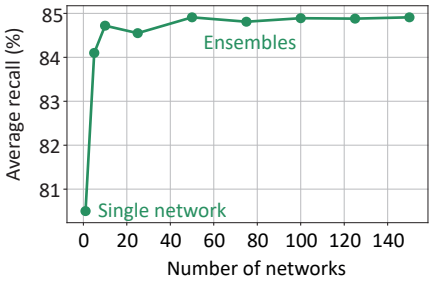

▲ Figure 3.4: The average recall plotted against the number of networks in the ensemble shows a sharp increase when going from one to five networks. This is followed by shallow general increase as the number of networks is increased to 150. There is a tradeoff to be made between ensemble accuracy and overall computation time.

an ensemble is increased to 150. Note that because these networks were validated on the validation data, which had few examples compared to the testing data, the networks randomly performed poorer. When checking the performance with testing data, which has a much broader range of examples, the performance appears to be a few percent higher still.

Ultimately, 20 networks were chosen, not randomly, but on the basis of having a accuracy higher than 75%. Comparing accuracies obtained on validation data, this ensemble saw an improvement of 5% over the ensemble of 10 random networks. Table 3.2 shows the accuracy that was achieved on testing and validation data for all classes with this ensemble.

Class	Testing data accuracy (%)	Validation data accuracy
Sharp	83	83
Double	80	88
Unstable	92	90
Step country	93	92
Bad country	82	89
Rubbish	99	100
Average	88	90

Table 3.2: The accuracies obtained on the ensemble of 20 networks that themselves achieved over 75% accuracy each.

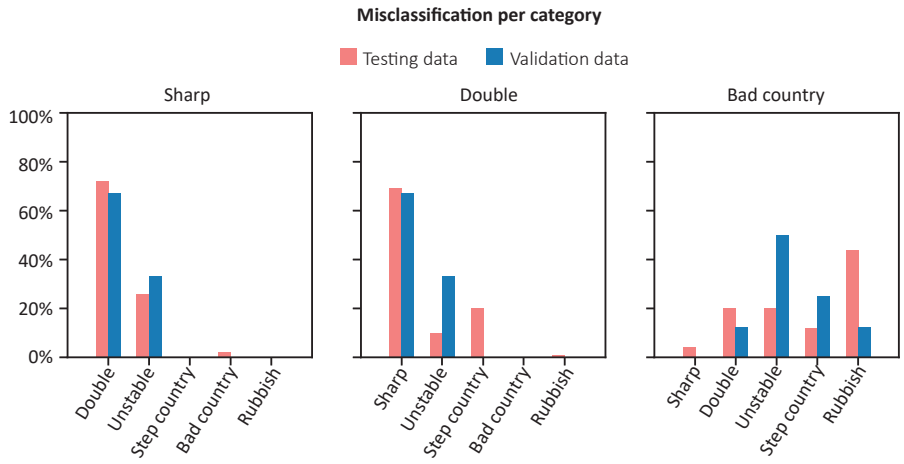

▲ Figure 3.5: Of the images with true labels sharp, double and bad country, but that the network predicted incorrectly, these plots show which categories the network "thought" they were.

The categories that had the lowest accuracy were sharp, double and bad country. To get some further insight into why this might be, we examined which categories the ensemble misclassified the data into. Figure 3.5 shows a breakdown by percentage of which categories the ensemble mislabelled sharp, double and bad country images. Note that the amount of validation data is small, thus testing data should be considered more representative of performance (also because of the fact that the testing data is used for the final evaluation of the network.)

In distinguishing certain categories, the ensemble performs exceptionally well, with close to 0% of sharp or double images being mislabelled as bad country or rubbish. The ensemble also performs quite well at distinguishing sharp and double from step country, except in the case where 20% of mislabelled testing data in the double category is mislabelled as step country. This miscategorisation has an intuitive explanation - multiple apparent step edges can either mean a double tip, or that the surface itself really has multiple terraces, as mentioned earlier.

The double and sharp categories get confused with each other the most frequently by the network. This comes as no surprise, given that we observed during the manual categorisation process that humans contradict not only each other, but also themselves. The difficulty of classifying sharp and double images in particular is because there is no clear-cut division between classes, but rather a spectrum where one must draw their own subjective line. This subjective line can shift depending on

the examples that the person has seen very recently, and of course standards vary from person to person.
While it's unlikely that a bad country image would be predicted as a sharp image (0% of validation data and 4% of training data is misclassified there), there is no single category that gets particularly confused for bad country. More images get misclassified into unstable or rubbish categories, which makes some sense because scans in these categories, together with bad country, have the largest variation in z-height. A possible explanation for the comparatively wide distribution of mislabels is that the bad country category had fewer examples than the other categories; only 379 in the training set, compared to over 1000 in each of the other categories.
To eliminate some bias in the manually classified data, one could consider

- letting one person reclassify the entire dataset multiple times, and using majority voting. However, manually labelling several thousand images is tedious and takes time away from the researcher.
- Alternatively, one could put a threshold on a measurable quantity in the image, such the slope of step edges or the Au(111) herringbone reconstruction.

3.4.2 Reclassifying dataset based on step edge slopes

We formulated a metric by which to distinguish sharp and double images in a more objective manner. Height profiles were measured perpendicular to the step edges. The criterion for an image to be sharp was defined as a transition from the higher terrace to the lower terrace in under 7 pixels. This agrees with the human perception of the two categories, and led to an equal division of data across sharp and double.
Fifteen networks were trained on the original data, and fifteen on the data reclassified based on the step edge metric. The networks were trained with the aforementioned structure and parameters, but with 175 epochs. Table 3.3 shows the average accuracy the two ensembles achieved for each category.
Interestingly, the accuracy was lowered by recategorising the images with this method. A possible reason for this is that the height profile measurement was unreliable; the angle of mearurement was not always at 90°to the step edge, and the automatic flattening procedure was not perfect.

Class	Original data accuracy (%)	Reclassified data accuracy (%)
Sharp	79	75
Double	76	71
Unstable	90	92
Step country	87	87
Bad country	78	77
Rubbish	99	99
Average	85	83

Table 3.3: Accuracies of ensembles of 15 networks trained on the original data, classified by humans, and the data reclassified by the step-edge metric that we formulated. The accuracy was lowered by using this metric.

3.5 Conclusion

An ensemble of convolutional neural networks based on the VGG architecture was built, and optimal parameters were found; 12 layers, with a learning rate of 0.0005, using Adam as the optimizer. Different numbers of epochs were used in the final 20 networks. Overall accuracy of the final ensemble of 20 networks was 88% on testing data and 90% on validation data.
One of the aspects that could be improved was the existence of bias in the manually classified data, particularly between the sharp and double category. An attempt was made to remove the subjectivity in the categorization by introducing a metric based on step-edge profile, but this led to a reduction in accuracy. Other ideas to improve are:

- Synthetically generate pre-categorised data, where the blur would be well-defined.
- One person could recategorise the data several times, and the ultimate labels could be based on a majority vote.
- More data of certain types could be acquired to better balance the amount of data in each category.
- Reconsider the categories based on the ultimate action that the SPM software should execute, rather than the state of the image (there is overlap in the action, e.g. a tip conditioning action and a lateral shift in position should be performed if a bad country or rubbish image is detected.)
- Testing different network architectures or parameters. For example, it is said that using ELU rather than ReLU as an activator may increase the network

performance slightly.[299]

3.6 Outlook

Convolutional neural networks have clearly shown themselves to be powerful tools to assess SPM image quality, both here, and in wider literature. Each group that has contributed to the burgeoning field of image recognition applied to SPM images; i.e. The University of Nottingham, The University of Alberta and others, have vividly demonstrated clear proofs-of-concept, but each for different substrates. The obvious conclusion is to build a generalised system that can correctly recognise the tip state for any given surface, and act upon its decision appropriately. This ambition may require a huge dataset that includes examples of all kinds of surfaces, and, to put a scale to it, it's not uncommon for publicly available datasets to have hundreds of thousands or millions of examples.[324–327] We see some potential for a collaborative, global effort across SPM groups to compile a large database of SPM images. These images already exist; they are out there collecting metaphorical and maybe literal dust on old hard drives, servers, CDs and floppy disks of SPM groups worldwide. These images are useful; they represent real use-cases, including incomplete scans and scans of various scales and resolutions, which the ultimate algorithm should be able to deal with. We note that one such data collection effort has already been initiated,[328] however, their focus is on molecular systems studied with functionalised tips rather than generic surfaces. The elephant in the room here is that this data would need to be labelled, which requires (a lot of) human input, and by extension introduces (a lot of) human bias. The alternative is to generate training data *in silico*, with classes pre-determined. To this end, efforts are being made at Utrecht University to create synthetic training data rather than collecting vast amounts of experimental data. In principle, an STM image of any surface could be simulated either algorithmically, or by using techniques like muffin tin, DFT or other physical models. That being said, however, neural networks can serve scanning probe microscopists in more ways than simple tip sharpening for imaging. The possibilities include automatic tip functionalisation, automatic surface patterning, tip conditioning for good spectra (a tip fit for imaging is not necessarily fit for spectroscopy[329]), continued improvement in molecule identification, feature recognition and "superhuman" pattern recognition ([314]). Researchers like Robert Wolkow and Philip Moriarty look to the distant future and imagine that AI used for scanning probe applications could even be used to create nanoprocessors on a large scale, or to create molecular machines. Looking perhaps even father afield, we could be on the cusp of a shift in the very way we do science, to use neural networks to help with discovering physical concepts.[330]

3.7 Glossary

Accuracy	Defined as (Number of correct predictions)/(Total number of predictions).[331]
Activation function	A function that determines the output of a node in a neural network. In the brain analogy, this is like whether a neuron fires, and with what strength.
Batch size	Since the amount of training data is so large, it cannot be fed through the network all at once. The batch size is the number of examples passed to the network at a time.
Dropout	Dropout is a form of regularization. With some probability, some nodes are randomly disconnected from one layer to the next.[332]
Epoch	One epoch means that the neural network has seen all the examples in the training set once.
Filter/Kernel	A small matrix that is used to perform an operation on an image (or other volume within the network) such as convolution.
Hyperparameters	Parameters that apply to the network that are not part of the training itself, but that should be adjusted to achieve peak performance, e.g. learning rate, decay, regularization.

Learning rate	The neural network learns by adjusting weights. The adaption of these weights as the network learns is determined by the optimizer. How fast this adjustment takes place is the learning rate.
Max pooling	A regularization technique that reduces the dimension from one layer to the next in a neural network. A filter is applied across the image with a certain stride, and only the maximum value within that region proceeds to the next layer.
Optimizer	The algorithm used to improve the weights and biases in a network, rather than changing them at random in the slim hope of producing a good prediction. The most basic algorithm is stochastic gradient descent. The one used here is Adam[322]
Overfitting	When the network performs well at categorising images that it has seen before (i.e. examples in the training set) but performs poorly on new data, the network is suffering from overfitting.
Padding	The data array can be expanded by placing values at the interfaces. The method used here is zero-padding, where zeros are placed at the edges of the image arrays. The purpose of this is to preserve information at the edges as the example proceeds through the network.
Recall	Of all positive identifications by the network, the recall is the proportion that the network got correct. It is calculated by (True positives)/ (True positives + False positives).

Regularization	Refers to any alteration to the neural network that reduces overfitting and improves its ability to generalize; that is, to perform well on data that it has never encountered before.
ReLU	This stands for Rectified Linear Unit. ReLU is an activation function that is defined by $f(x) = max(0, x)$. In other words, the input passes to the next layer unless it is less than 0.
Stride	A value that determines the movement of the filter as a matrix operation is performed.
Supervised learning	A type of machine learning where training data has been labelled according to classes, as opposed to unsupervised learning where no labels are given to the input data.[299]
Test Dataset	The sample of data used to provide an unbiased evaluation of a final model fit on the training dataset.
Training dataset	The sample of data used to fit the model.
Validation Dataset	The sample of data used to provide an unbiased evaluation of a model fit on the training dataset while tuning model hyperparameters.
VGG-16	VGG refers to the Visual Geometry Group at the University of Oxford, however it is used to refer to the CNN architecture that they produced in 2014 which performs exceptionally well on image databases.

CHAPTER 4

COUPLING QUANTUM CORRALS TO FORM ARTIFICIAL MOLECULES

This chapter is based on:
Coupling quantum corrals to form artificial molecules.
Saoirsé E. Freeney, Samuel T. P. Borman, Jacob W. Harteveld, Ingmar Swart.
SciPost Physics, 9, 085 (2020)

4.1 Abstract

Quantum corrals can be considered as artificial atoms. By coupling many quantum corrals together, artificial matter can be created at will. The atomic scale precision with which the quantum corrals can be made grants the ability to tune parameters that are difficult to control in real materials, such as the symmetry of the states that couple, the on-site energy of these states, the hopping strength and the magnitude of the orbital overlap. Here, we systematically investigate the accessible parameter space for the CO on Cu(111) platform by constructing (coupled) quantum corrals of different sizes and shapes. By changing the configuration of the CO molecules that constitute the barrier between two quantum corrals, the hopping integral can be tuned between 0 eV and ~ -0.3 eV and ~ -0.16 eV for *s*- and *p*-like states, respectively. Incorporation of orbital overlap is essential to account for the experimental observations. Our results aid the design of future artificial lattices.

4.2 Introduction

The scanning tunneling microscope makes it possible to position adsorbates and vacancies on surfaces with atomic scale accuracy.[333] This approach has been used to explore the limits of data storage,[334–337] to perform logic operations,[338–341] to study chemical reactions at the single molecule level,[342–345] and to study the electronic and magnetic structure of atomically well-defined structures.[346,347]

With respect to studying electronic properties of extended systems, two complementary approaches have been used. The first approach is based on coupling localized states of either adatoms, vacancies or dangling bonds,.[21,348–354] By positioning such species with atomic scale precision, artificial electronic molecules or lattices can be created and their electronic structure studied. Initial experiments focused on the evolution of the electronic structure with system size. However, more complicated and interesting phenomena can also be studied, such as topological states of matter and Majorana bound states.[21,355]

The second approach, following the ideas underpinning the quantum corral, is based on patterning a 2D electron gas (2DEG) with a (periodic) scattering potential. In particular, the CO on Cu(111) platform has been used to study the electronic structure of periodic and non-periodic systems.[7,230,279,287,288,356,357] Here, the CO molecules act as repulsive scattering centers for the surface state electrons of Cu(111).[358] By placing these scattering centers with atomic scale accuracy, a large variety of potential energy landscapes can be created for electrons. For example, by creating a triangular lattice of CO molecules, the electrons are confined to the anti-lattice, i.e. a honeycomb geometry.[7] Density of states measurements revealed the emergence of a Dirac cone in the 2DEG, as observed in graphene. Building on this approach, an electronic Lieb-lattice,[230] quasi-crystal[287] and electronic fractal[288] have been realized. Recently, it was shown that this material platform can also be

used to study topological states of matter.[357,359]

One of the advantages of using artificial lattices is that it allows control over parameters that cannot be controlled easily in real materials. These include the on-site energy, the strength of the hopping parameter, orbital overlap, and which orbitals couple. However, the values for the hopping parameter, on-site energy of each electronic site and overlap are not immediately obvious given a certain configuration of CO/Cu(111). Currently, determining these parameters is an involved iterative "reverse engineering" procedure which includes first designing the lattice and performing a muffin-tin calculation to check that the features of interest are observable, which may take several iterations of design changes. The resulting muffin-tin band structure is compared to the output of a tight-binding calculation. The tight-binding parameters are then adjusted such that the tight-binding band structure matches the muffin-tin result.[359]

In this work, we systematically investigate the accessible tight-binding parameter range for the CO/Cu(111) platform by coupling quantum corrals into artificial molecules. The report is arranged as follows. First, a background on the subject is given, and the experimental details are discussed. We show how changing the size of rectangular and triangular corrals affects their on-site energy and we determine the effective mass of the confined electrons. We specifically focus on rectangular and triangular corrals, as these allow for space-filling artificial lattices. Furthermore, we report experiments on coupling such units into dimers and trimers and extract the tight-binding parameters. We investigated the coupling of both *s*-like and *p*-like orbitals. The coupling strength is adjusted with different methods; both by changing the size of the potential barrier between the corrals, and by changing the size of the corrals themselves. Finally, we studied the coupling of orbitals with different symmetries.

Before describing our results, we discuss the similarities and differences between quantum corrals and real atoms. Artificial lattices built using CO/Cu(111) can be thought of as systems of coupled quantum corrals. The first quantum corral was created by positioning Fe atoms in a (nearly) circular ring on Cu(111).[333] The electronic behavior within the corral can be readily understood in terms of a particle-in-a-box model.[229,333] Figure 4.1a shows wavefunctions of a particle-in-a-circular-box for a combination of the first few quantum numbers. For circular corrals, the wavefunctions are characterized by the principle and angular quantum numbers, n, ℓ, respectively. $n-1$ defines the number of nodal lines in the radial direction from the center, while ℓ defines how many nodes occur angularly. For non-circular symmetric corrals,the angular momentum quantum number is not well-defined. However, the wave functions of circular, rectangular and triangular corrals exhibit alternation of sign and nodal line patterns that are reminiscent of nodal planes in atomic orbitals.[279] The lowest energy state has no nodal lines, the second lowest has one, etc.[360,361] Based on these similarities, we refer to these states of the quantum corral as *s*-like and *p*-like, respectively. The nodal line pattern of a particular

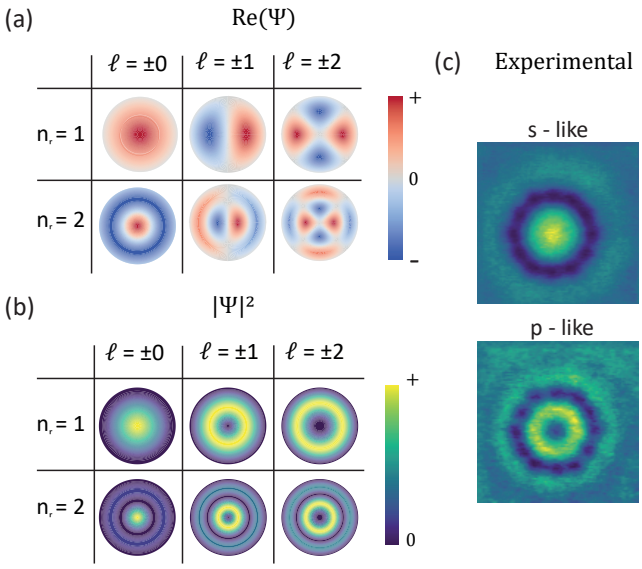

▲ Figure 4.1: Modeling a circular quantum corral with the particle-in-a-box model. (a) The real part of the wavefunction enclosed in a circular well, showing its shape for different quantum numbers. (b) $|\Psi|^2$, which is proportional to the differential conductance in STM. (c) Differential conductance maps of a small quantum corral at two energies; -0.17 V and 0.21 V. These correspond to the $\ell = 0$, $n = 1$ ($1s$) and $\ell = 1$, $n = 1$ ($1p$) states.

state of the quantum corral can be visualized by mapping the differential conductance at the energy corresponding to that state. In principle, the spin quantum number m_s is also common between a 2D particle-in-a-box and a real atom, because m_s only describes whether an electron has spin $+\frac{1}{2}$ or $-\frac{1}{2}$, and is a general property of electrons.

In contrast to 2D quantum corrals, three quantum numbers appear for real atoms. The magnetic quantum number is not present in 2D systems. However, as we show below, p_x- and p_y-like states do emerge in rectangular corrals.[279] Furthermore, the allowed values of the quantum numbers are different for quantum corrals and real atoms. For example, circular 2D quantum corrals feature $1p$-type states (see Fig 1a,b), whereas in real atoms a $1p$ state does not exist.

In addition to Fe atoms, a variety of other adsorbates can be used as scattering centers. Because of the ease and reliability with which they can be manipulated, CO molecules are often used.[338,362,363] Carbon monoxide molecules on the Cu(111) surface are imaged as depressions with standard metallic tips.[364] A DFT study has

suggested that this is due to destructive interference of the protruding orbital of oxygen atom with the states in the tip.[365]
Throughout this document, we show the designs of various corrals and indicate copper atoms as orange dots and CO molecules as black dots with shading that represents the apparent size of the CO molecule as viewed in STM. Corral dimensions are reported in terms of the Cu(111) lattice constant $a = 0.2556$ nm .[366]

4.2.1 Tight-binding description of dimers and trimers

To create artificial dimers, we construct two connected corrals with an opening between them to accommodate coupling. Figure 4.2a shows an example of a structure consisting of two coupled rectangular corrals.
The tight-binding parameters of interest are the on-site energy, ϵ, the nearest and next-nearest neighbor hopping parameters, t_1 and t_2 (not present for dimers) respectively, and the overlap integral, s,[367,368] see figure 4.2. It was previously reported that the next-nearest-neighbor hopping integral can be non-negligible in

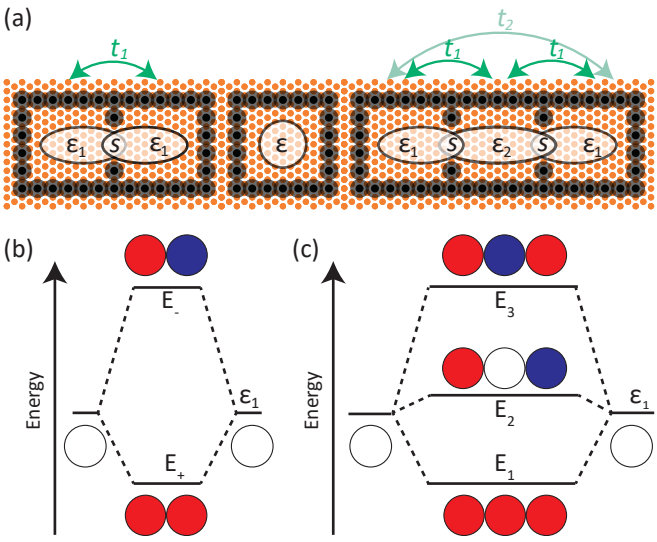

▲ Figure 4.2: Coupling quantum corrals. (a) Example placements of CO molecules (black) on Cu(111) (orange) to produce a dimer, a lone corral and a trimer. White ovals roughly represent the spatial extent of the wave functions of the individual quantum corrals. (b) and (c) show the molecular orbital diagrams for a dimer and a trimer, respectively. Red represents a positive value of the wavefunction and blue negative.

artificial lattices.[230,279,288,357,359] To determine the magnitude of t_2, we also constructed and characterized trimers, see figure 4.2c.
A tight-binding calculation of a dimer, taking into account only the lowest energy state of each corral, results in the following expressions for the two states of the dimer

$$E_+ = \frac{\epsilon_1 + t_1}{1+s} \tag{4.1}$$

$$E_- = \frac{\epsilon_1 - t_1}{1-s} \tag{4.2}$$

where the subscript indicates the sign with which the states of the corral are added. The values of E_+ and E_- can be directly extracted from differential conductance spectra acquired at suitable positions above the dimer (taking the shape and extent of the wavefunction into account). Since the spatial confinement of the electrons in the dimer is different from those of isolated corrals (there is an extra available area when the barrier between two corrals is removed, the on-site energy is different for coupled and individual corrals. The resulting set of two equations with three unknowns (4.1 and 4.2) cannot be solved. To determine values of ϵ_1, t_1 and s, we include calculations and measurements on a trimer, as represented in figure 4.2c. We make the assumption that the overlap integral is the same for the dimer and trimer.
In the case of a trimer, there are three energy states that correspond to bonding, non-bonding and antibonding orbitals in molecules, as illustrated in figure 4.2(e). The energies of these three states are given by equations 4.3, 4.4 and 4.5, respectively.

$$E_1 = \frac{\epsilon_1+\epsilon_2-4st_1+t_2-\sqrt{(-\epsilon_1-\epsilon_2+4st_1-t_2)^2-4(1-2s^2)(\epsilon_1\epsilon_2-2t_1^2+\epsilon_2 t_2)}}{2(1-2s^2)} \tag{4.3}$$

$$E_2 = \epsilon_1 - t_2 \tag{4.4}$$

$$E_3 = \frac{\epsilon_1+\epsilon_2-4st_1+t_2+\sqrt{(-\epsilon_1-\epsilon_2+4st_1-t_2)^2-4(1-2s^2)(\epsilon_1\epsilon_2-2t^2+\epsilon_2 t_2)}}{2(1-2s^2)} \tag{4.5}$$

where t_2 is the next-nearest-neighbor hopping parameter, ϵ_1 is the on-site energy of each of the outer two atoms (the same as in the dimer) and ϵ_2 is the on-site energy of the central atom, see figure 4.2c. Since E_1, E_2 and E_3 are also observable in experiment, we now have a system of five equations (4.1 to 4.5) and five unknowns. This allows us to obtain all tight-binding parameters ϵ_1, ϵ_2, s, t_1, and t_2.

4.3 Methods

All experiments were performed at $T \approx 4.5$ K in ultra-high vacuum with a ScientaOmicron LT-STM. A Cu(111) surface was prepared by several repetitions of sputtering with Ar^+ and annealing at 550° C. Carbon monoxide was leaked into the microscope chamber with a direct line of sight onto the Cu(111) crystal mounted in the microscope head to achieve a suitable coverage. Manipulation of carbon monoxide molecules was performed in feedback with a bias voltage of 20 mA and a current setpoint of approximately 50 nA, depending on the configuration of the tip apex. STM images were acquired in constant current mode. Differential conductance spectra and maps were acquired with the tip at constant height and using a standard lock-in amplifier technique. The frequency and amplitude of the applied modulation was 271 Hz and 10 mV r.m.s. respectively. Integration time for signal acquisition was 50 ms during spectra and 20 ms during maps. All differential conductance spectra shown have been averaged over several measurements acquired at the same position, and divided by an average of several spectra taken on bare Cu(111) with the same tip apex to minimise the LDOS contribution from the tip.[7] In each spectrum shown, the faded points represent the data after the aforementioned procedure, while the solid line represents the moving average of the same data.
Muffin-tin calculations were performed to corroborate and supplement the experimental data. This technique is well-established, and has been used before to simulate results on the CO/Cu(111) platform with reasonable accuracy.[230,279,288,357,359]

4.4 Results

4.4.1 Individual Corrals

We first characterize rectangular corrals. Note that because of the triangular symmetry of the underlying substrate, it is not possible to build perfectly square corrals. Figure 4.3a shows the schematic structure and $\frac{dI}{dV}$ spectra of a rectangular corral with size $8\sqrt{3}a \times 14a$. Spectra taken at different positions exhibit peaks at different positions, corresponding to specific eigenstates. For example, the lowest energy level (approximately -0.3 V) has the highest local density of states (LDOS) in the center of the corral (black), whereas the next highest energy level (-0.1 V) is mainly observed away from center (at red, blue and green sites). The differential conductance maps reveal the spatial extent of these states, see the top row in figure 4.3b. The corresponding simulated maps are shown in the bottom row of the same figure. In the case of degenerate levels, the modulus squared of the relevant eigenfunctions were summed. The simulations are in excellent agreement with the experimental observations.

For rectangular quantum corrals, there are two quantum numbers that determine the energy of the system and the shape of the wavefunction; n_x and n_y. By comparing the experimental data to the results of the particle-in-a-box model, we can assign wave functions to the differential conductance maps and peaks in differential conductance spectra. For the first few energy levels, we may draw an analogy to real atoms based on the number of nodal lines in Ψ that intersect the center of the corral. The $n_x = 1, n_y = 1$ (no nodal lines) resembles an atomic s-orbital. Similarly, the $n_x = 1, n_y = 2$ (and $n_x = 2, n_y = 1$) (one nodal line) and $n_x = 2, n_y = 2$ (two nodal lines), have a similar nodal line structure as p- and $d-$type orbitals in atoms. The next highest state is the $2s$-like state.

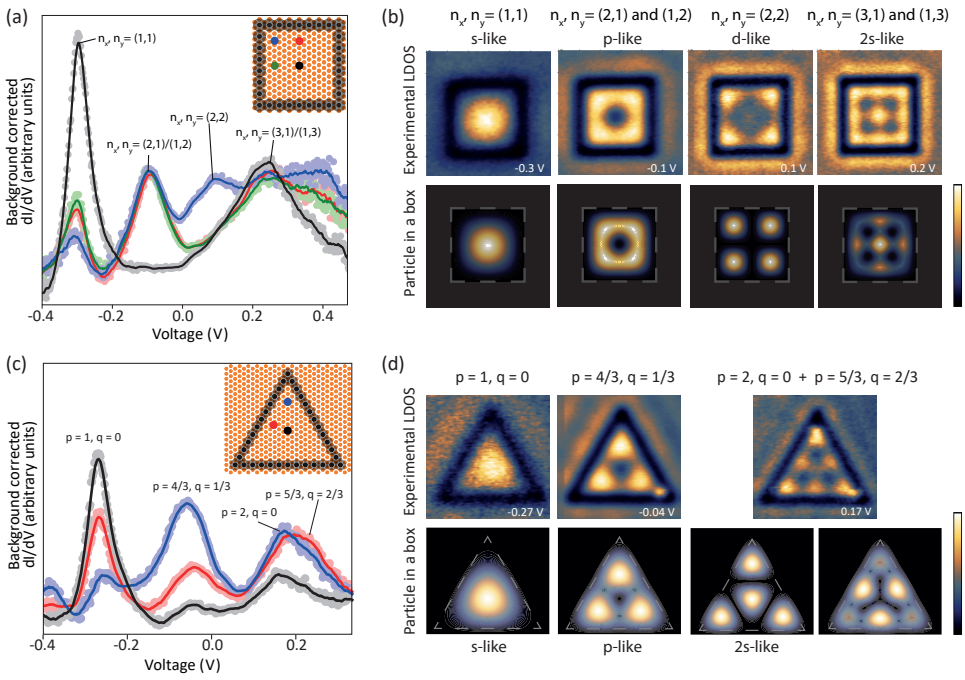

▲ Figure 4.3: Differential conductance measurements on rectangular and triangular quantum corrals. (a) dI/dV spectroscopy acquired at the positions marked in the inset figure. (b) Top: experimental differential conductance maps (of size 6 nm × 6 nm) acquired at the energies stated; bottom: $|\Psi|^2$ calculated according to the particle in a box model. The quantum numbers are labeled above each peak in the dI/dV and above each LDOS map. (c), (d) same as (a) and (b) but for triangular quantum corral. The images depict an area of 6.25 nm × 6.25 nm.

We now apply the same procedure to triangular corrals. An equilateral triangular corral is constructed with side lengths $12\sqrt{3}a$. $\frac{dI}{dV}$ spectroscopy was conducted at different positions, see figure 4.3c. The lowest energy peak is observed at approximately -0.27 eV and has the highest amplitude in the center of the corral ($s-$like). state. The second energy level is mainly localized near the corners (p-like orbital). $\frac{dI}{dV}$ maps acquired at the peaks observed in the $\frac{dI}{dV}$ spectra are shown in figure 4.3d. For a particle-in-a-triangular-box, there are two quantum numbers; p and q. The calculated eigenfunctions corresponding to the first four energy levels are shown in the bottom row of figure 4.3b. For the first two states, there is excellent agreement between experimental and simulated maps. The energy difference between the third ($p = 2, q = 0$) and fourth ($p = 5/3, q = 2/3$) lowest energy states of a particle in a triangular box is small. Consequently, both states contribute to the experimentally observed contrast at $V = 0.17$ V.

4.4.2 Corral size and on-site energy

We now consider how altering the size of a corral affects the energies of the lowest levels, *i.e.* the on-site energies. We first focus on rectangular corrals. Figure 4.4a shows a series of rectangular quantum corrals that were constructed. Differential conductance spectra acquired at the centers of the corrals are shown in figure 4.4b. As the corral is reduced in size, the ground state shifts to higher energies. The second peak for S1 at higher energies corresponds to a 2s-like orbital, *vide infra*. Note that peaks become progressively broader with increasing energy. We attribute this to two factors. First, the scattering potential of the CO molecules is finite (0.9 eV with respect to the onset of the surface state band when a radius of 0.3 nm is used). Hence, electrons with higher energy effectively experience a lower barrier height. Secondly, the number of CO molecules per unit area is larger for smaller corals, resulting in an increased coupling between surface and bulk states.[369]
To rationalize the experimental observations, we model our system using a particle-in-a-box model with finite potential barriers of height $V_0 = 0.9eV$.[361] For a 2-dimensional rectangular box with finite barriers, the energies are given by

$$E = V_0 - \frac{2\hbar^2}{m^*}\left(\frac{u_{n_x}^2}{L_x^2} + \frac{u_{n_y}^2}{L_y^2}\right) \tag{4.6}$$

where $m^* = 0.42m_e$, the effective mass of the Cu(111) surface state electrons, and L_x and L_y correspond to the length of the box in the x and y direction, respectively.[361] The variables u_{n_x} and u_{n_y} take the role of quantum numbers. Their values are the solutions to the following set of three equations (where i denotes the x or y direction of the rectangular box. The lengths in x and y are distinct from one another because our corrals are not perfect squares).

$$u_{n_i} = \sqrt{u_{0_i}^2 - v_i^2} \tag{4.7}$$

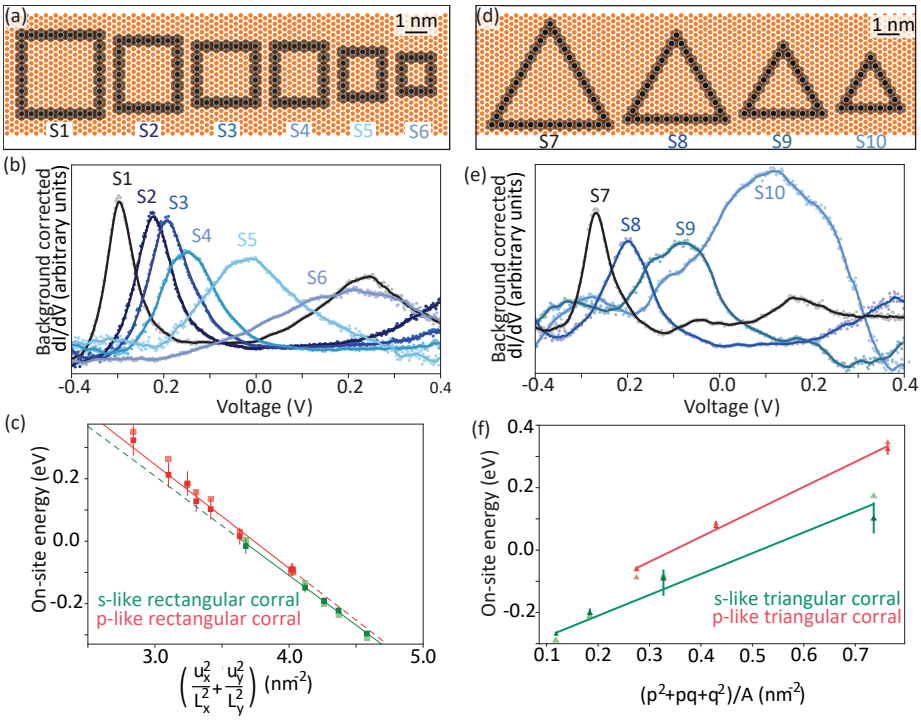

▲ Figure 4.4: (a) Geometries of the rectangular corrals investigated. (b) $\frac{dI}{dV}$ spectra taken at the centers of the rectangular corrals shown in (a). (c) On-site energy as a function of $u_{n_x}^2/L_x^2 + u_{n_y}^2/L_y^2$. Green and red points represent experimental data for s- and p- like states respectively. Light red and light green points represent the energies calculated using a muffin-tin model. Solid lines represent a linear fit to the experimental data. (d)-(f) Same as (a)-(c) but for triangular corrals.

$$u_{n_i} = v_i \tan(v_i) \tag{4.8}$$

$$u_{n_i} = -v_i \cot(v_i) \tag{4.9}$$

with $u_{0_i} = \frac{\sqrt{2m^* V_0} L_i}{2\hbar}$, $u_i = \frac{\sqrt{2m^*(V_0 - E)} L_i}{2\hbar}$ and $v_i = \frac{\sqrt{2m^* E} L_i}{2\hbar}$. See the appendix of this chapter for more detail on these equations. No analytical solutions exist for these equations and one has to rely on graphical or numerical methods. The solutions are given by the values of u_i where function (4.7) intersects function (4.8)

or (4.9), and are denoted u_{n_i}. For a given V_0, L_i and effective mass, the values of u_{n_i} are fixed, and can be thought of as analogous to the quantum number in the energy equation that describes a particle in a 2D rectangular box with infinite barriers. To calculate the values of u_n, we use $V_0 = 0.9$ eV[230,279,288,357,359] and $m^* = 0.42m_e$.[194,195] The values of L_x and L_y are determined by assuming that the dimensions of the boxes are defined by the edges of the CO molecules which have a diameter of 0.6 nm.[230,279,288,357,359]

Figure 4.4c shows a plot of the on-site energy versus $u_{n_x}^2/L_x^2 + u_{n_y}^2/L_y^2$ for the lowest and second lowest states. Dark (light) green and red (light red) correspond to experimental (muffin-tin) data of s-and p-like states, respectively. The experimental energies were determined by fitting Gaussian curves to each peak and finding the centers. The muffin-tin-derived energies were calculated with the aforementioned values for V_0, m^* and CO diameter. For both states, the energy depends linearly on $u_{n_x}^2/L_x^2 + u_{n_y}^2/L_y^2$. From the gradient, we determine the effective electron masses to be $0.48 \pm 0.01\mathrm{m}_e$ and $0.46 \pm 0.01\mathrm{m}_e$ for the s-like and p-like states, respectively. These values are close to the effective electron mass of the unconfined surface state electrons. A small offset is visible between the lines for the $s-$ and p-like data, which we attribute to the fact that the confining potential is effectively lower for higher energy states.

We applied a similar procedure to triangular corrals. Figure 4.4d shows the geometry of several triangular corrals that were realized, and figure 4.4e shows spectra acquired at the centres. The states of triangular corrals shift to higher energies the smaller the corral becomes. The data can be rationalized using a particle-in-a-box model using infinite barriers (analytical solutions for the finite barrier triangular corrals with finite barriers have not been reported)). The energy eigenvalues of a particle in an equilateral triangular box are given by

$$E_{p,q} = \frac{h^2}{2\sqrt{3}m^*A}(p^2 + pq + q^2), \tag{4.10}$$

where p, q are the quantum numbers, h is Planck's constant, m^* is the effective electron mass and A is the area of the triangle.[360,370,371] As shown in figure 4.4f, the experimentally determined on-site energy depends linearly on the inverse surface area, in agreement with equation (4.10).

4.4.3 Coupling Corrals

We now turn to coupled quantum corrals and show how tight-binding parameters can be extracted from experimental data. After a dimer is constructed (example shown in figure 4.5a), $\frac{dI}{dV}$ spectra are acquired on two positions. We do this to make use of the different spatial localization of the E_+ and E_- states. Specifically, the anti-bonding E_- state has a node between the two corrals (the position denoted by an orange dot in the inset of figure 4.5a). Only the bonding E_+ state appears

in the differential conductance spectrum taken at that site and we can fit the spectrum with a single Gaussian. Conversely, the anti-bonding E_- state has higher intensity at the outer regions of the dimer (red dot in figure 4.5a).

Differential conductance maps were acquired at approximately the energies of the centers of each of the two peaks. The state at lower energy is delocalized over the entire structure, whereas the state at higher energy has a node between the two corrals. This is reminiscent of bonding and anti-bonding molecular orbitals, respectively.

Next, a trimer is constructed from the same-sized units as the dimer. To determine

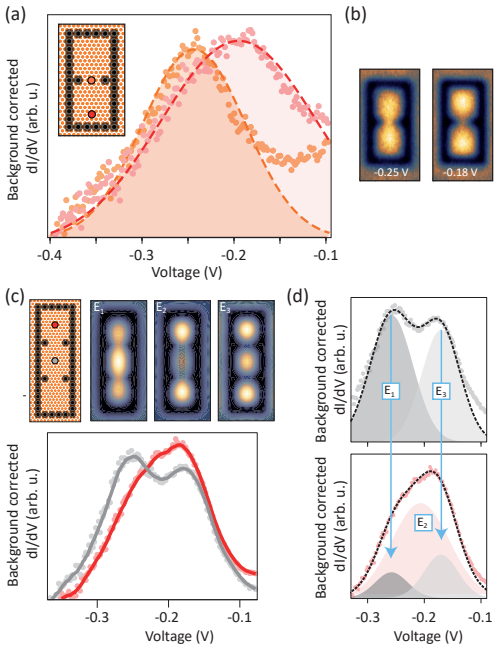

▲ Figure 4.5: (a) $\frac{dI}{dV}$ spectra on two different positions of a dimer. Locations indicated by dots in the inset. (b) Differential conductance maps were acquired at the approximate energies where the maxima of the peaks lie. (c) Bottom: $\frac{dI}{dV}$ spectra acquired at the positions shown in corresponding colors in the top left diagram. LDOS maps (from muffin-tin calculations) at E_1 = -0.26 eV, E_2 = -0.22 eV, E_3 = -0.18 eV, respectively. (d) Gaussian fitting procedure applied to the same two spectra to find the energies of interest. The shaded regions in each plot represent the individual Gaussians, which when summed, lead to the curves represented by dashed lines. The centers of the Gaussians correspond to E_1, E_2 and E_3 (labeled).

the experimental values of E_1, E_2 and E_3, we again exploit the different spatial distributions of these three states. Muffin-tin calculations show that the intensity of the E_2 state is very low at the center corral. Hence, the two peaks in the differential conductance spectrum taken at this position (grey curve in figure 4.5d) can be assigned to E_1 and E_3, respectively. The obtained energies can then be used in the fitting procedure of the spectrum acquired at a corral at the end of the trimer (red curve in figure 4.5c and d). Taking these values and solving equations 4.1 to 4.5 results in the tight-binding parameters listed in Table 4.1.

Parameter	Value
ϵ_1	-0.22 ± 0.02 eV
ϵ_2	-0.23 ± 0.01 eV
s	0.5 ± 0.3
t_1	-0.14 ± 0.06 eV
t_2	-0.02 ± 0.03 eV

Table 4.1: Tight-binding parameters extracted from figure 4.5.

The on-site energy of the individual corral of this size is -0.19 ± 0.02 eV, see figure 4.4c. We find an on-site energy of -0.22 ± 0.02 eV and -0.23 ± 0.01 eV for the sites in the dimer and central site in the trimer, respectively. This lowering of the on-site energy can be understood from the increased area that is available due to the removal of the CO molecules to couple the sites. Two CO molecules have been removed from the barrier, *i.e.* an additional area of $2 \times \pi(0.3)^2 = 0.56$ nm^2 is available for the electrons. The magnitude of the overlap integral, s, is significant and therefore must be included in tight-binding parameters to yield accurate answers. The same experiments and simulations were performed for coupling triangular corrals.

4.4.4 Tuning parameters

We now systematically investigate how the tight-binding parameters depend on changing the gap width between corrals for both s- and p-like states. For this, we created dimers out of rectangular quantum corrals with dimensions $6\sqrt{3}a \times 10a$ (same as in the previous section) and $8\sqrt{3}a \times 14a$. (Note that to calculate the area from these dimensions, the area that the CO molecules occupy must be subtracted). First, two corrals of equal size were constructed directly next to each other with the barrier fully closed; that is to say that the same barrier configuration that separates the two corrals separates the corrals from their surroundings. Figure 4.6a shows the schematic of a lone corral with dimension $8\sqrt{3}a \times 14a$, and the dimer with a full wall of CO molecules separating the corrals. The second column shows

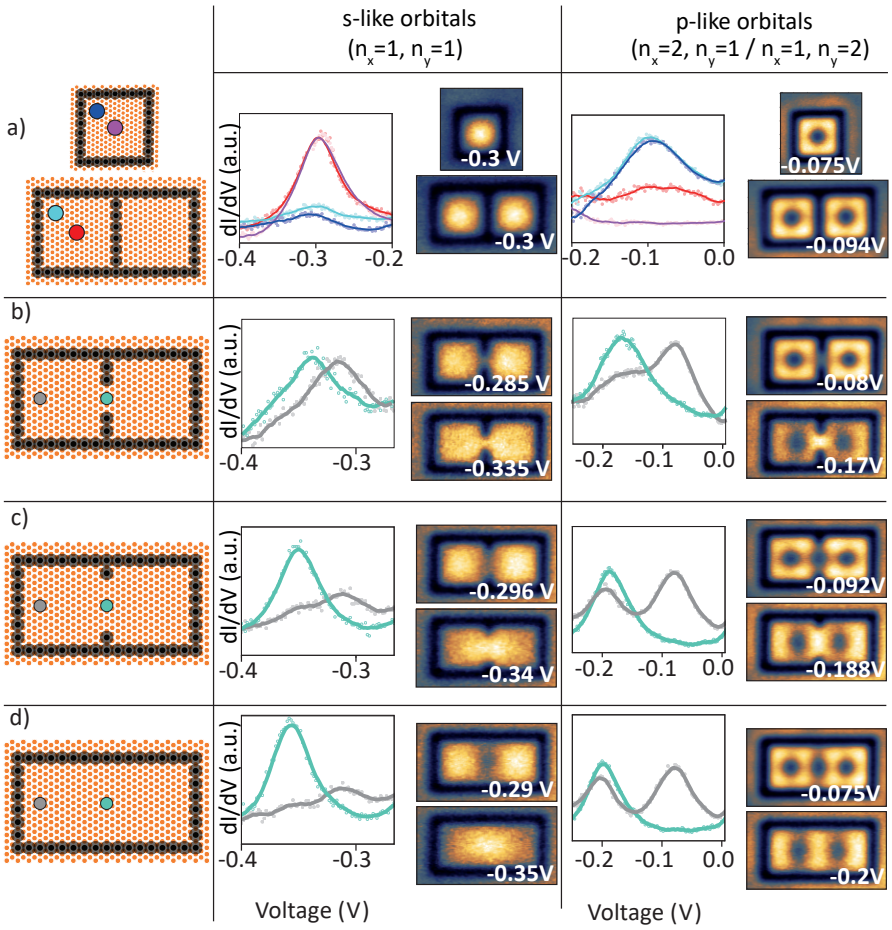

▲ Figure 4.6: Column 1: Schematics of the (coupled) corrals. Column 2: Coupling of s-like orbitals: $\frac{dI}{dV}$ spectra have been acquired at the positions indicated by the color code and corresponding $\frac{dI}{dV}$ maps taken at the indicated energies. Column 3: Coupling of p-like orbitals. The x-axis of each $\frac{dI}{dV}$ spectrum is voltage, and the y-axis is the background corrected $\frac{dI}{dV}$. Row (a) shows two corrals with a full barrier between them, and a comparison of measurements with a single corral. Rows (b-d) shows what occurs when the gap in the barrier is opened incrementally.

spectra taken at the positions marked in the designs. The peaks associated with the s-type orbitals occur at the same energy for the two systems, indicating that there is virtually no coupling between the corrals in the dimer with this barrier configuration (the hopping parameter is zero). The same observation is made for the p-type states (right hand side of the figure). This is significant because it has been assumed that coupling of electronic sites to the surrounding 2DEG plays a large role in broadening.[357] Our experiments provide an upper-limit to the coupling strength across a 'full barrier': any potential splitting of the bonding and antibonding states is smaller than the energy resolution of our experiments. A muffin-tin calculation using small broadening finds a peak splitting of 11 meV (suggesting an upper limit of the coupling strength of 6 meV).

Next, CO molecules are removed from the center of the barrier, see figure 4.6b-d. As described before, $\frac{dI}{dV}$ spectra were acquired at the barrier between the corrals, and near the outer edge. By fitting Gaussian curves and finding their centers, we determine the energy level spacing between the bonding and anti-bonding states. Differential conductance maps were taken to verify the resemblance of these states to bonding and antibonding orbitals. The difference in energy between the two states increases with increasing gap width in the CO barrier between the two corrals. Furthermore, the states shift down in energy due to the effectively larger area that the electrons can occupy.

The most natural interpretation of the experimental data for the system without barrier, figure 4.6d, is to use a particle-in-a-rectangular-box model. In this picture, the lower energy state corresponds to the ground state with quantum numbers $n_x = 1$ and $n_y = 1$. The second state is the $n_x = 2$, $n_y = 1$ state, etc. However, it is also possible to interpret the results in the framework of two coupled quantum corrals. The lowest energy state of the rectangle can be thought of as the bonding combination of s-like orbitals of the two quantum corrals. Similarly, the second lowest state would be the anti-bonding combination.

The bonding combination of the p_x-like states, where x is the horizontal direction, shows vertical nodal lines at the centers of the individual corrals and enhanced intensity in the barrier region between the corrals (see right hand side of figure 4.6). The nodal line pattern of the map at higher energy can be rationalized by assuming that both the anti-bonding p_x-like state as well as the p_y-like state contribute to the contrast. The energy difference between p-like bonding and antibonding states is larger than for the s-like states.

Similar experiments were performed for coupled $6\sqrt{3}a \times 10a$ dimers (data not shown). From the available data on both corral sizes, tight-binding parameters for coupling of both s-like and p-like states were derived. The results are shown in figure 4.7. The size of the gap in the barrier between the corrals is defined as the distance between the closest CO molecules of the barrier, minus two times the apparent radius of the CO molecules (0.3 nm, see figure 4.7a). For both s- and p-like states and for both corral sizes, the data points for the hopping parameter (t), the on-site energy

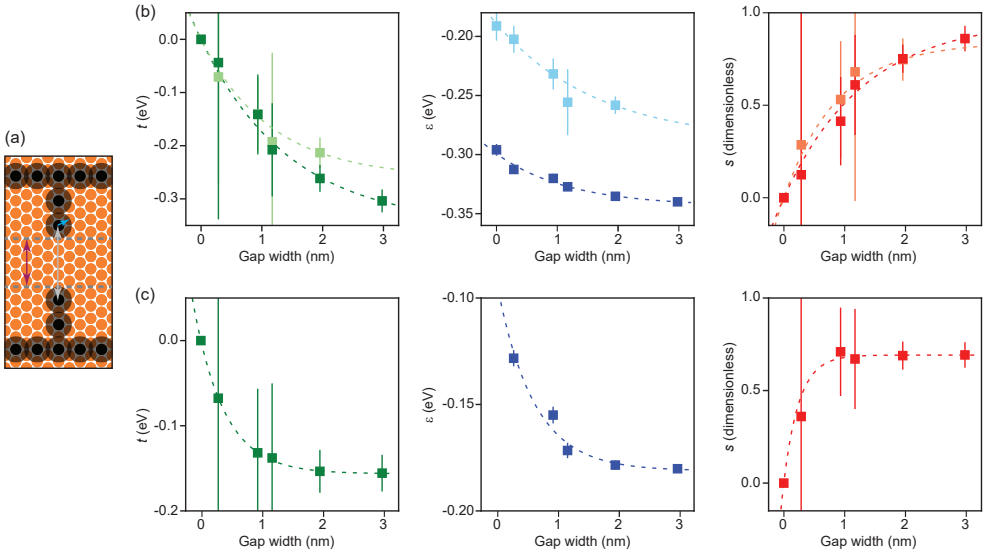

▲ Figure 4.7: (a) The size of the gap in the barrier between the two corrals (red arrow) is the distance between the closest CO molecules in the barrier (gray arrow), minus two times the apparent size of the CO molecules (gray circle, blue arrow, 0.3 nm). (b) From left to right: gap dependence of the hopping parameter, the on-site energy and overlap for s-like states, respectively. Dark and bright colors represent data from rectangular corrals with sizes $8\sqrt{3}a \times 14a$ and $6\sqrt{3}a \times 10a$, respectively. (c) Same as (b) but now for p-like states.

(ϵ), and the orbital overlap (s) can be fitted with an exponential function (dotted lines). By tuning the gap width, the hopping parameter can be varied between 0 eV and ~ -0.3 eV and ~ -0.16 eV for s- and p-like states, respectively. We find that the on-site energy depends on the width of the gap in the barrier. The parameters depend more sensitively on gap width for the smaller corral. This can be rationalized from the additional area that becomes available to the confined electrons upon removing CO molecules (the relative increase in available area is larger for the smaller corral). Finally, the magnitude of the orbital overlap increases with gap width. Note that for unconfined electrons (infinite gap width) the overlap should be one. Figure 4.7b suggests that at least up to a gap width of ≈ 1.5 nm, the hopping parameter and overlap are similar for the two different corral sizes.

4.4.5 State selective coupling

Since CO molecules can be removed selectively, it becomes possible to create geometries that allow coupling of p-type states only. Consider the geometries of coupled rectangular and triangular corrals shown in figure 4.8a and d. The amplitude of s-type wave functions is small at the position of the gaps in the barrier. Hence, coupling of s-type states should be small. In contrast, p-type states have significant amplitude at these positions and consequently these states should couple strongly. We first focus on the rectangular corrals. Figure 4.8b shows differential conductance spectra taken at the positions indicated in figure 4.8a. A total of three peaks are observed. The amplitude of each peak differs from position to position. The peak at lowest energy corresponds to the ground state, *i.e.* it involves s-type states. At the energies corresponding to the s-type states, we only observe one peak, indicating that these states do not couple (coupling strength below the detection limit of our experiment). In contrast, the spectrum of the barrier region (gray) features a peak around 90 mV, whereas the spectrum taken at the corner of the corral (blue) has a peak at 170 mV. The corresponding differential conductance maps, figure 4.8c, reveal that the spatial extent of these states can be understood by considering coupling of p_y-type states. For the triangular corral, similar observations are made. This confirms the idea that artificial lattices allow coupling between sites by one type of state only.[279] Note that this provides a degree of freedom that is not available in real materials.

4.4.6 Coupling corrals of different sizes

Finally, we investigate the coupling of two corrals of different sizes, *i.e.* with different on-site energies for the s- and p-like states. Fig. 4.9a shows the arrangement of such a polar dimer, with the barrier between corrals fully removed to maximize coupling. The $\frac{dI}{dV}$ spectra show the typical peaks associated with bonding and antibonding states. The corresponding differential conductance maps reveal that the lower (higher) energy state of the dimer is primarily localized on the larger (smaller) corral, see figure 4.9b and c. This is in agreement with a tight-binding model of a dimer with constituents with different on-site energy.
In general, electronic states couple if they spatially overlap and if they have a similar energy. Hence, if the sizes of the two corrals differ sufficiently, it is possible to couple the s-like state of a smaller corral with a p-like state of a larger corral. We therefore created a dimer consisting of a $6\sqrt{3}a \times 12a$ to a $4\sqrt{3}a \times 8a$ corral, see figure 4.9d. The $\frac{dI}{dV}$ spectra reveal two states with different spatial localization. The corresponding differential conductance maps show that the lower energy s-like state of the smaller corral couples with a p-like state of the larger corral. Similarly, the higher energy state can be thought of as an antibonding combination between s- and p-like states (note the nodal line at interfaces between the two corrals).

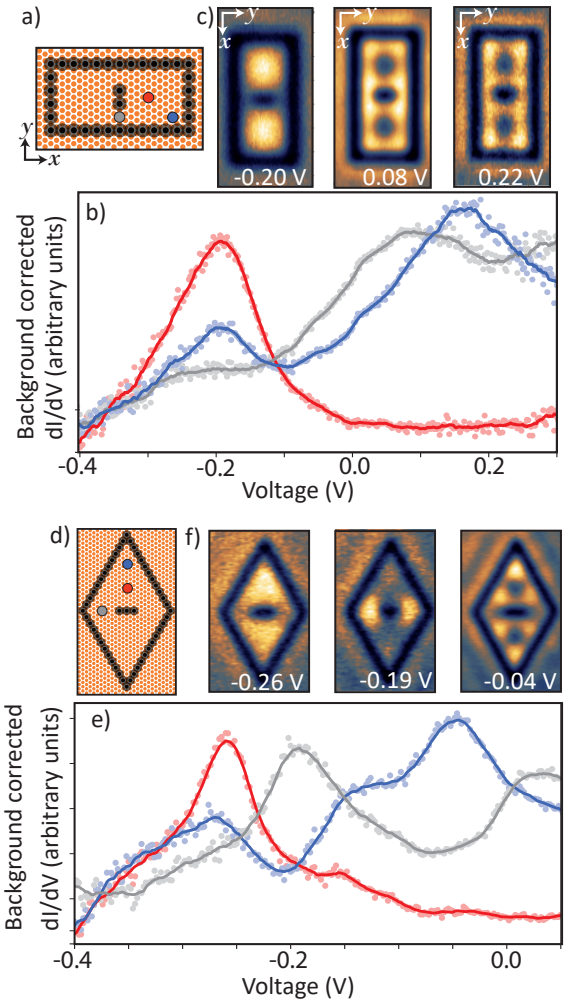

▲ Figure 4.8: (a) Coupled rectangular corrals with a barrier that largely inhibits the coupling of s and p_x-type states, while coupling of p_y-like states is clearly observed. x and y directions are specified in the figure. (b) Differential conductance spectra taken at the positions indicated in (a). (c) Differential conductance maps taken at the indicated energies. (d-f) same as (a-c) but for coupled triangular corrals.

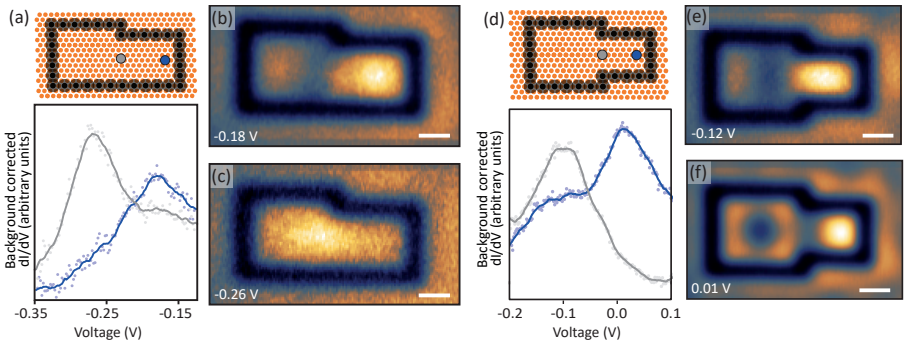

▲ Figure 4.9: (a) Schematic structure of anisometric dimer consisting of a $6\sqrt{3}a \times 12a$ corral coupled to a $5\sqrt{3}a \times 10a$ corral. Differential conductance spectra acquired on positions highlighted in the inset. (b),(c) differential conductance maps of the two states observed in the $\frac{dI}{dV}$ spectra (energies indicated in the figure). (d)-(f) same as (a-c), but now for a $6\sqrt{3}a \times 12a$ corral coupled to a $4\sqrt{3}a \times 8a$ corral. Inset scale bar (white) represents a length of 1 nm

4.5 Conclusion

To conclude, we have studied the coupling of rectangular and triangular quantum corrals into dimer and trimer structures. These shapes were chosen as they can be used as building blocks of artificial lattices. The electronic structure of the coupled corrals can be understood using a tight-binding model also used for the coupling of atoms to molecules. Importantly, we investigated the available tight-binding parameter space accessible with the CO/Cu(111) platform, and showed how these parameters depend on the configuration of the coupled quantum corrals.
We first verified that the particle in a box model provides a good qualitative description of the electronic structure of rectangular and triangular quantum corrals. We determined the on-site energies of *s*- and *p*- like states of different sized corrals to confirm the relationship between on-site energy of the corral and box size. From this, we determined the effective masses of electrons in rectangular corrals to be on the order of 0.48 m_e and 0.46 m_e for $s-$ and $p-$ like states respectively. These values are close to the value for unconfined Cu(111) surface state electrons (0.42 m_e). In the triangular case, we used a model that assumed infinite barriers, preventing us from determining a reliable value for the effective mass.
We outlined a method to extract tight-binding parameters (nearest and next nearest neighbor hopping parameters, overlap and on-site energy) by constructing dimers and trimers of corrals. By removing CO molecules from the barrier between corrals, exponential relationships were found between the tight-binding parameters and the size of the gap in the barrier between the corrals. The hopping integral can be tuned between 0 and -0.3 eV and -0.16 eV for *s*- and *p*-like states, respectively, by tuning the configuration of CO molecules in the barrier. In most cases, the overlap is not negligible and this term should be taken into account when modelling artificial molecules and lattices. Finally, we showed that in these coupled quantum corrals, one can control which states couple. For example, by appropriate placement of CO molecules coupling of $s-$ and p_x-like states can be inhibited, while allowing coupling of p_y-like states. Furthermore, it is possible to couple *s*- and *p*-like states. The results presented here are useful for future work on artificial lattices made using CO on Cu(111). A hypothetical lattice with certain desired coupling strengths and on-site energies can be designed by estimating the required unit size and barrier gap width from the trends reported here.

4.6 Appendix: Further description of the finite box model

The quantum corrals we investigate are described by a finite potential well model. In this case, the wavefunction penetrates the barrier and decays exponentially outside. The wavefunction is either symmetric (described by an even function) or asymmetric (described by an odd function) about the centre of the box in one dimension. This box has width L and is centred at 0. Its boundaries are at $-\frac{L}{2}$, $\frac{L}{2}$. The boundaries are defined by a potential barrier of height V_0. Figure 4.10 shows a finite potential well with equations of the wavefunction defined inside and outside of the box for even (ground state) and odd (second lowest state) functions.

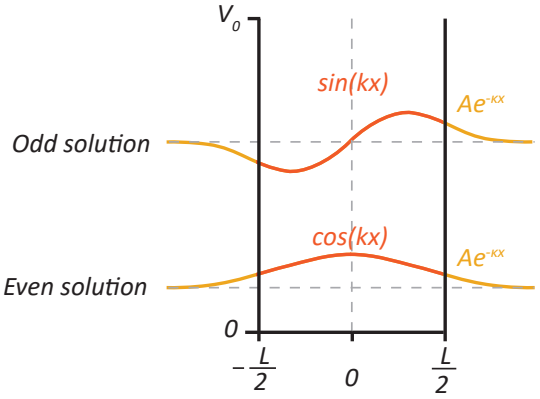

▲ Figure 4.10: The description of the potential well.

4.6.1 Symmetric solution

In the even case, the wavefunction (equation 4.11) and its derivative (equation 4.12) satisfy the following boundary conditions:

$$Ae^{-\kappa L/2} = \cos(kL/2) \tag{4.11}$$

$$-\kappa Ae^{-\kappa L/2} = -k\sin(kL/2), \tag{4.12}$$

where A is a normalisation constant, k is the wavevector and κ is the decay constant of the exponentially decaying wavefunction outside of the box.

Dividing (4.12) by (4.11) gives

$$\kappa = k\tan(kL/2). \tag{4.13}$$

4.6.2 Asymmetric solution

For the odd case, the wavefunction (equation 4.14) and its derivative (equation 4.15) satisfy:

$$Ae^{-\kappa L/2} = \sin(kL/2) \tag{4.14}$$

$$-\kappa Ae^{-\kappa L/2} = k\cos(kL/2). \tag{4.15}$$

Dividing (4.15) by (4.14) gives

$$\kappa = -k\cot(kL/2) \tag{4.16}$$

4.6.3 Finding k and κ

We can find expressions for both κ and k by substituting the second derivatives of the wavefunction inside and outside of the box into the Schrödinger equation. The time-independent Schrödinger equation can be written:

$$\frac{\partial^2\psi(x)}{\partial x^2} = \frac{-2m^*}{\hbar^2}(E - V(x))\psi(x). \tag{4.17}$$

Finding k

Inside the box, $V(x) = 0$ and $\psi(x) = \cos(kx)$ (arbitrarily taking the even function, though of course we could similarly use the odd function). We can insert these into (4.17), as well as the second derivative of the wavefunction, $\psi''(x) = -k^2\cos(kx)$, to give

$$-k^2\cos(kx) = \frac{-2m}{\hbar^2}(E - 0)\cos(kx) \tag{4.18}$$

$$k = \frac{\sqrt{2mE}}{\hbar}. \tag{4.19}$$

Here, k is the usual interpretation of the wavevector.

Finding κ

To find κ, we use the same logic but this time we consider the behaviour outside the box. In the region outside the box, $V(x) = V_0$, $\psi(x) = Ae^{-\kappa x}$ and $\psi''(x) = \kappa^2 Ae^{-\kappa x}$. Inserting these into 4.17 gives:

$$\kappa^2 Ae^{-\kappa x} = \frac{-2m}{\hbar^2}(E - V_0)Ae^{-\kappa x} \tag{4.20}$$

$$\kappa = \frac{\sqrt{2m(V_0 - E)}}{\hbar}. \tag{4.21}$$

4.6.4 Determining the "quantum numbers"

We now have expressions for κ and k, but if we insert these into equations 4.13 and 4.16, we would find that both sides depend on energy. We cannot obtain an analytical expression for energy as in the case of the infinite well. However, the energies can be found graphically or numerically. We let $u = \kappa L/2$ and $v = kL/2$, and find from the definitions of κ and k that $u^2 = u_0^2 - v^2$, where $u_0 = \frac{2mV_0}{\hbar}$. To obtain the energies, we must find the values of u that satisfy the following:

$$\sqrt{u_0^2 - v^2} = \begin{cases} v \tan v \text{ (even solutions)} \\ -v \cot v \text{ (odd solutions)} \end{cases}$$

The solutions are the graphical intersections between the function on the left hand side of the equation with the functions on the right (all three functions are functions of v). We label the values of u where the intersections occur u_{n_i}, where i denotes either the $x-$ or $y-$ dimension, since we have a 2D box. Figure 4.11a shows a plot of the functions of u vs v. Here, the lengths of the corral in the x-direction that were used in experiment were incorporated. This is seen in the radial functions of increasing radius, since the quantity L is included in u_0. Thus, the larger the radius of the quarter-circle seen in the plot, the longer the length of the box used in the equation. In assigning the box lengths, we assume that our boxes are experimentally defined by the edges of the CO molecules which have a diameter of 0.6 nm. The CO diameter was observed with STM, and this value is found to yield accurate energy predictions using muffin-tin. Note that in u_0, the quantities V_0 and m^* also appear. We assume the values $V_0 = 0.9eV$ and $m^* = 0.42m_e$, which have been used before to accurately simulate experimental results using the muffin-tin model. Intersections between the different functions of u are marked, with their colour indicating which energy level the solution is associated with.

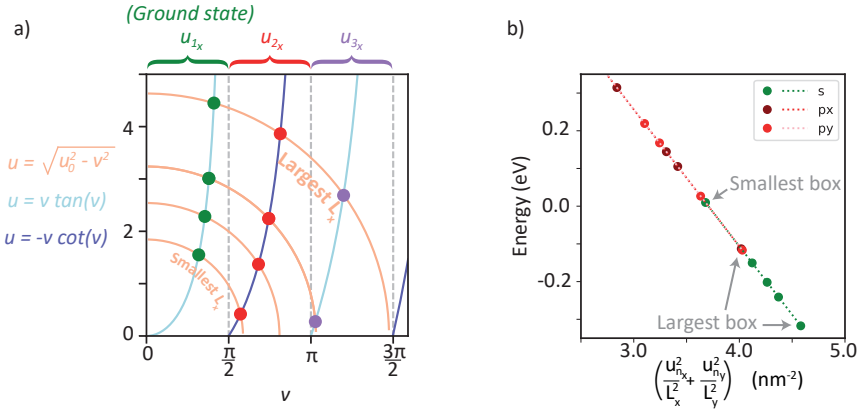

▲ Figure 4.11: (a) Plot of the functions of v with intersections shown, to calculate u_{n_x}. The relationship between u and v determined from the definitions of κ and k is shown in peach, and the relationship derived from even and odd solutions are in light blue and navy respectively. The intersections corresponding to the lowest energy state are shown in green, second lowest in red and third lowest in purple. (b) Using the intersections found in (a) combined with a similar calculation for u_{n_y}, the energies have been plotted for $s-$ and $p-$ like states. The energies match those found from experiment.

4.6.5 Finding energies

For a given V_0, L_i and effective mass, the values of u_{n_i} are fixed, and can be thought of as analogous to the quantum number in the energy equation that describes an infinite well. Using $u = \kappa L/2$, as previously defined, along with equation 4.21, the energy can be found from the intersections u_{n_i} using

$$E = V_0 - \frac{2\hbar^2 u_{n_i}^2}{m^* L_i^2}. \tag{4.22}$$

In 2-dimensions, this becomes

$$E = V_0 - \frac{2\hbar^2}{m^*}\left(\frac{u_{n_x}^2}{L_x^2} + \frac{u_{n_y}^2}{L_y^2}\right). \tag{4.23}$$

Figure 4.11b shows the energies calculated from equation 4.23 using the same box dimensions as in the experiment. An offset of 0.445 eV has been added to each energy, because in experiment, the bottom of the potential well lies at the surface state minimum, which sits at -0.445 eV compared to the Fermi energy that we mea-

sure from in STM. This gives remarkably close values to those seen in experiment as well as muffin-tin (compare figure 4.11b to figure 4.4c of the main text). Equation 4.23 shows that the effective mass can be found by determining the gradient of the graph E vs $(\frac{u_{n_x}^2}{L_x^2} + \frac{u_{n_y}^2}{L_y^2})$. In the main text, the experimental energies are plotted on the y axis while the x axis contains the values of u_{n_i} calculated as aforementioned. Note that the gradient of this plot is inherently negative and has an offset given by V_0. To compare energies to those measured in STM, the surface band minimum must also be considered in the offset.

CHAPTER 5

EDGE-DEPENDENT TOPOLOGY IN KEKULÉ LATTICES

This chapter is based on:
Edge-dependent topology in Kekulé lattices.
Saoirsé E. Freeney[†], Jette J. van den Broeke[†], Anthonie J. J. Harsveld van der Veen, Ingmar Swart, and Cristiane Morais Smith.
Physical Review Letters, 124:236404, 2020
[†] Both authors contributed equally.

5.1 Abstract

The boundary states of topological insulators are thought not to depend on the precise atomic structure of the boundary. A recent theoretical study showed that for crystalline topological insulators with given bond strengths, topological states should only emerge for certain edge geometries. We experimentally probe this effect by creating artificial Kekulé lattices with different atomically well-defined edge geometries and hopping ratios in a scanning tunneling microscope. Topological edge modes are found to only appear for specific combinations of edge geometry and hopping ratio.

5.2 Introduction

A common assumption concerning topological states of matter is that their existence should be insensitive to any detail, except the topology of the bands. This is indeed the case for the quantum Hall effect[23,372,373] or for the quantum spin Hall effect,[50,91,92] which are triggered by a magnetic field or by a strong spin-orbit coupling, respectively. However, theory predicts that the edges of crystalline topological insulators are important.[374,375] The reason is that the topological invariant depends on the choice of unit cell, which also determines the edge geometry. To establish the relation between edge geometry and the existence of protected boundary states in topological crystalline insulators experimentally, it is essential to work with systems that have atomically precise edges.

Electrons in engineered potentials can be used to study the electronic properties of a large variety of systems, ranging from artificial periodic lattices[7,230] and quasicrystals[287] to fractals.[288] Importantly, it is possible to control the hopping strength between different sites.[7,226] Vacancies in a chlorine monolayer on Cu(100) have been coupled together to realize topologically non-trivial domain-wall states in 1D Su Schrieffer Heeger (SSH) chains.[21] In addition, the manipulation of Fe atoms on the superconducting Re(0001) surface led to the realization of a topological superconductor.[219,376] Recently, the carbon-monoxide (CO) on Cu(111) platform has been used to create a so-called higher-order topological insulator.[357] This platform is therefore ideally suited to experimentally address the relation between the geometric structure of topological crystalline insulators and the emergence of non-trivial states.

We investigate this relation by focusing on the Kekulé lattice, see figure 5.1. The lattice consists of a triangular array of hexagonal molecules with intra-hexagon bond strength t_0 (light blue lines), connected to each other by bonds of strength t_1 (navy lines). Gapless edge modes appear when the edge is connected only via weak bonds to the rest of the lattice, and are protected by sublattice and mirror symmetry.[377,378]

Here, we experimentally show that the same Kekulé structure may be trivial or

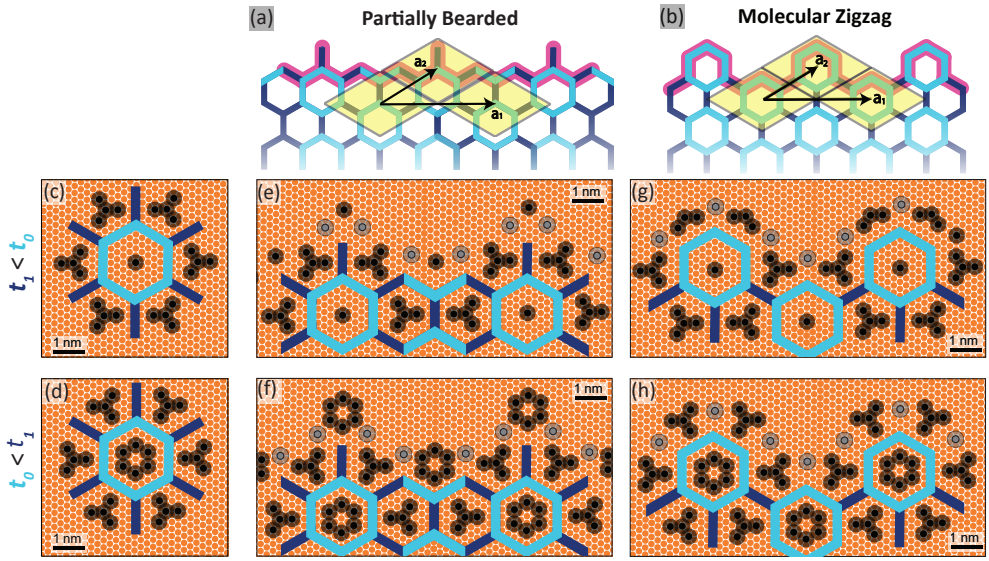

▲ Figure 5.1: (a) and (b) give the geometries of the partially bearded and molecular zigzag edges. The light blue and navy lines indicate the intra- and inter-hexagon hopping parameters respectively. The edges are highlighted in pink. The unit cell is defined by one yellow rhombus. Lattice vectors $\boldsymbol{a_1}$ and $\boldsymbol{a_2}$ are shown. To form the edge, translation is performed along the $\boldsymbol{a_1}$ direction. (c) and (d) depict configurations of CO molecules that lead to hopping regimes $t_1 < t_0$ and $t_0 < t_1$, respectively. (e-h) show the configurations of CO molecules to realize the partially bearded and molecular zigzag edges in both hopping regimes. The gray circles represent additional CO molecules that reduce the interactions with the surrounding 2D electron gas.

topological, depending on the termination of the sample. The experimental observations are corroborated by theoretical calculations using muffin-tin and tight-binding approaches for the specific experimental realization, as well as investigations of the underlying crystalline symmetries protecting the topological phase.

5.3 Methods

To experimentally realize Kekulé lattices with atomically well-defined edges, we pattern the surface of a Cu(111) crystal with CO molecules, such that the surface state electrons form the desired structure.[7] All experiments were performed using a commercially available Scienta Omicron Low Temperature - Scanning Tunneling Microscope (STM). Experimental and theoretical procedures used were the same as

described previously.[230, 288, 357] Details are provided in the appendix.
We generate finite lattices with two different hopping parameter ratios and two different edge terminations (bearded or molecular zigzag[377]). The design of the lattices is shown in figure 5.1a and figure 5.1. The leftmost column of the pictographic table in figure 5.1 shows the precise positioning of the CO molecules on Cu(111) for a single Kekulé unit cell. For $t_0 < t_1$, the repulsive potential introduced by the central six CO molecules diminishes the strength of t_0 (light blue). In contrast, for $t_1 < t_0$, there is less repulsion about the single central scatterer. Additionally, for $t_0 < t_1$, each triangularly shaped collection of four CO molecules reduces the bond strength between hexagons, while for $t_1 < t_0$ they are rotated 60° with respect to the opposite design. This allows for a stronger t_0, while simultaneously impinging on the connection between hexagons, decreasing t_1. Since the lattice has triangular symmetry, we have chosen the overall shape of the lattice to be a triangle to allow for the same type of edges on all sides. Symmetry is locally preserved at the edges, including at the corners, where there is local resemblance to the edges. Interactions with the surrounding 2D electron gas was minimized by adding additional CO molecules, see the appendix.
To verify that the configuration of CO molecules leads to the appropriate hopping regime, and to find the hopping parameters for use in tight-binding calculations, the band structures calculated within the tight-binding were matched to those calculated using the muffin-tin method. Besides the hopping parameters t_0 and t_1, orbital overlap and next-nearest neighbor (NNN) hopping between and within hexagons were considered in making the fit. The full list of obtained parameter values and a detailed description of the matching procedure and muffin-tin calculations is given in the appendix. Although the orbital overlap deforms the band structure and is therefore of vital importance to fully understand the experimental results, it was numerically verified that it does not break the topological protection of the edge states in the Kekulé lattice. The NNN hopping however, breaks chiral symmetry. It was found that most NNN hopping parameters were small ($\leq 0.02\, t_0$) due to the clustered CO structure. Only the NNN hopping within the hexagon for the $t_1 < t_0$ design ($0.2\, t_0$) is larger, as there is only one CO in the middle of the hexagons. Therefore, we expect that the chiral symmetry is weakly perturbed for this case.
Two different types of termination have been investigated for each lattice: the partially bearded edge and the molecular zigzag edge, as introduced in the first row of the pictographic table in figure 5.1.[377] Below each, the blueprints for the precise arrangement of the CO molecules used to achieve such edges are shown for both $t_1 < t_0$ and $t_0 < t_1$.

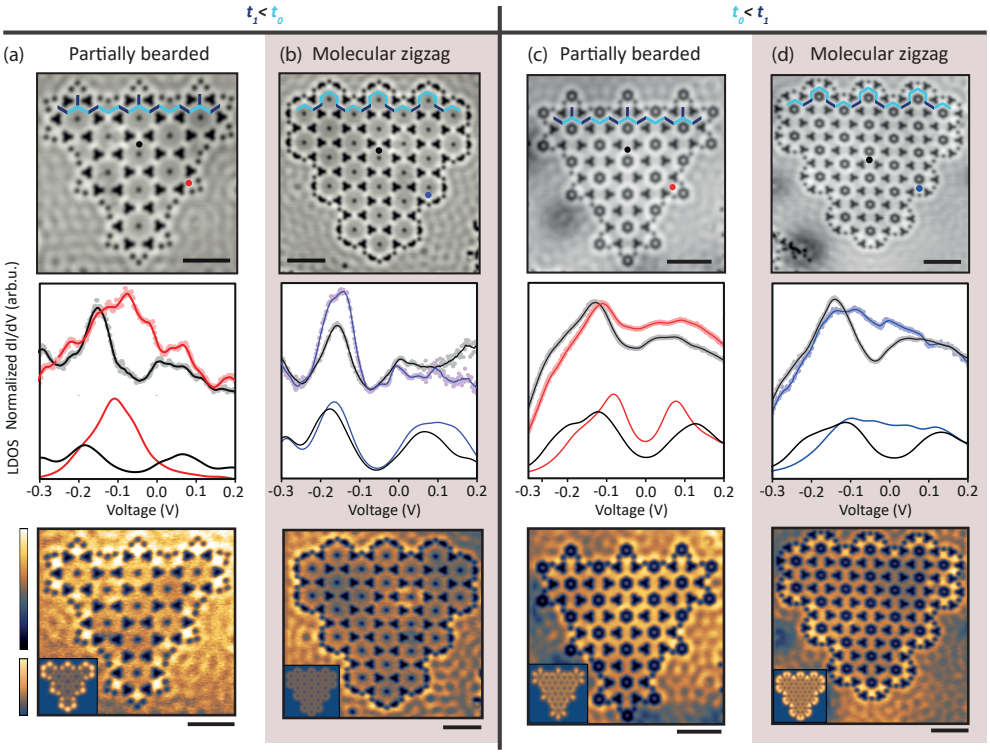

▲ Figure 5.2: (a) Top: STM topograph of a Kekulé lattice with partially bearded edges and in the $t_1 < t_0$ regime ($V_{gap} = 100$ mV, $I_{set} = 10$ pA). Navy and light blue colors indicate bonds as depicted in figure 5.1. Middle: experimental differential conductance spectra acquired at bulk (black) and edge (red) sites, normalized by spectra taken on Cu(111). Positions where spectra were acquired are indicated by colored dots in the top panel. The bottom curves depict the local density of states calculated using tight-binding. The bottom panel shows a differential conductance map acquired at a voltage close to the middle of the bulk gap ($V = -65mV$). The inset shows the tight-binding LDOS map. (b) is arranged the same way as column (a), but now for a lattice with a molecular zigzag edge in the $t_1 < t_0$ regime. Settings for the topograph: $V_{gap} = 100$ mV, $I_{set} = 100$ pA. (c) and (d) provide the same information as (a) and (b) but now for the opposite regime of hopping parameters, *i.e.* $t_1 > t_0$. Scan parameters for the topographs in (c) and (d): $V_{gap} = 100$ mV and $I_{set} = 30$ pA. Differential conductance maps were acquired at -20 mV and the local density of states was calculated at -20 meV. Scale bars (black) are 5 nm. All experimental differential conductance spectra were processed by averaging over numerous equivalent sites or repeated measurements within the same site, then dividing this average by the average of many spectra on bare Cu(111) with the tip in the same state.

5.4 Results and discussion

Two lattices with $t_1 < t_0$ are shown in the constant-current topographic images in figure 5.2a and figure 5.2b. They have the same bulk but are terminated with a partially bearded and molecular zigzag edge, respectively. Differential conductance spectra of bulk and edge sites of both lattices are shown in the middle panels of figure 5.2a and figure 5.2b (locations indicated by the colored dots in figure 5.2a and figure 5.2b). The spectra of bulk and edge sites of the molecular-zigzag terminated lattice are similar, *c.f.* black and blue curves in the middle panel of figure 5.2b. In contrast, the local density of states (LDOS) of bulk and edges sites of the lattice with the partially bearded edge are markedly different. The spectrum of bulk sites (indicated in black) shows two peaks associated with the valence (at $V = -0.15$ V) and conduction bands ($V = 0.05$ V), separated by a gap. The spectrum of the site indicated in red shows a large peak positioned at the energy of the bulk gap.

The experimentally observed features are reproduced in the tight-binding (lower curves in the middle panels of figure 5.2a and figure 5.2b) and muffin-tin simulations, see the appendix. For the calculated LDOS, a broadening of 80 meV was added to account for the coupling between surface and bulk states, as was done before.[230,279,288,357]

The spatial extent of the in-gap state is probed by taking differential conductance maps at energies corresponding to the middle of the gap (approximately the on-site energy of the system). By comparing the maps, shown in the bottom panels of figure 5.2a and figure 5.2b, it is immediately clear that the bearded edge features a well-defined edge localized mode, whereas the lattice with molecular zigzag edges in the same hopping regime does not. Again, the experimental features are reproduced in the simulations, see the insets in the bottom panels of figure 5.2a and figure 5.2b. This edge localized state is robust with respect to the introduction of defects, see the appendix.

These results support the theoretical prediction based on calculation of the topological invariant (the mirror winding number)[377] that the edge mode at the partially bearded edge is topological when $t_1 < t_0$.

The situation is reversed when the hopping strengths are inverted. Figure 5.2c and 5.2d show topographs and LDOS spectra for the Kekulé lattice in the opposite regime of hopping parameters, $t_0 < t_1$. In this case, for the partially bearded edge lattice (topograph shown in figure 5.2c), the experimental spectra at different edge positions match the behavior of the spectrum in the bulk of the crystal (figure 5.2c, middle panel): there is a dip in the experimentally measured LDOS around $V = -20$ mV for all positions measured, which implies trivially insulating behavior throughout. At the molecular zigzag edge (topograph in figure 5.2d) for the same $t_0 < t_1$ case, there is a markedly higher LDOS at the edge positions at energies corresponding to the bulk gap (figure 5.2d, middle panel). The differential conductance maps confirm that for this parameter regime, the molecular zigzag terminated

lattice features a topological edge mode. The theoretical spectra and maps agree with the experimental data, see inset in the bottom of figure 5.2d.

From these results, we conclude that non-trivial edge modes in crystalline topological insulators in a given regime of hopping parameters only emerge for specific edge geometries. The topological protection occurs at the Γ point and remains robust as long as the bulk states do not mix with the edge states in the middle of the bulk gap. Our experimental broadening is not large enough that we expect it to influence the topological protection.

Finally, we turn our attention to finite-size effects. We first study how edge states are protected in the ribbon geometry, and then investigate how these features change for the finite structures built experimentally. Kariyado et al.[377] found that the mirror winding number protects the zero energy crossing of the edge modes in the Kekulé system. As the calculation of this invariant requires both chiral symmetry and reflection symmetry M_y along the line passing through two directly opposite sites in a hexagon, both symmetries need to be present to protect the edge states. This has been confirmed by Noh et al.[378] by numerically adding perturbations to the Hamiltonian. In case of armchair terminated Kekulé lattices, the M_y symmetry is broken and the edge modes become gapped.

When a system can be divided in two subsystems that only couple to each other and never to themselves, the system possesses chiral symmetry. The chiral symmetry leads to a spectrum that is symmetric around zero energy. This means that zero modes can only move away from zero energy in pairs. If there are more sites of one subsystem than of the other on the edge, but not in the rest of the structure, this can result in zero modes on the edge, as in graphene ribbons with a zigzag termination.[379,380] The edge geometry considered here contains equally many sites of each sublattice. Thus, chiral symmetry alone does not enforce the existence of edge states. To understand the protection of zero modes in the system, we should therefore also consider the reflection symmetry M_y. At the Γ point in the Brillouin zone, M_y commutes with the Hamiltonian. Hence, the Hamiltonian needs to have the same eigenstates as M_y, and states which are even and odd under M_y cannot mix. This mechanism can prevent two zero modes on the edge of a Kekulé ribbon to mix, thus pinning them at zero energy due to the chiral symmetry.

The Kekulé lattices realized here have (approximate) chiral symmetry, since the NNN hopping is small. The M_y symmetry is preserved locally. In the experimental designs, the lattice sites are locally affected by the same environment as they would be in an infinitely long ribbon, as illustrated in figure 5.3a. However, the global mirror symmetry present in the ribbon is broken in the finite lattice: the boundary is not fully periodic due to modulations to form the corner. Moreover, the lattice is relatively small; thus the momenta are not continuous and a state with zero momentum (the Γ point) does not need to exist. By performing tight-binding calculations on finite molecular zigzag terminated lattices, we determine the evolution of the energy levels upon tuning the ratio t_0/t_1. Figure 5.3b and figure 5.3c show

this for lattices with 28 and 163 hexagons respectively. Upon increasing the system size, the states become more dense, compare figure 5.3c and figure 5.3b. Therefore, the in-gap energy levels obtained for a fixed ratio of t_0/t_1 are continuous lines for infinite systems, but become discrete dotted lines (coarse-grained) for finite sized systems. The smaller the system, the larger the distance between the dots. Nevertheless, the spreading and the number of edge states do not change with the size of the system. The finite size of the system also leads to hybridization, thus moving the zero-energy modes away from zero in parameter space: while the zero modes already deviate from zero energy at roughly 0.7 t_0/t_1 in figure 5.3b, in figure 5.3c, they remain close to 0 up to a larger value, about 0.9 t_0/t_1. For comparison, the molecular zigzag terminated lattice with $t_0 < t_1$ that we realized experimentally has 0.67 t_0/t_1 and 28 hexagons. More detail is given in the appendix. Note that since the edge states here are dispersive, they span the entire bulk band gap.

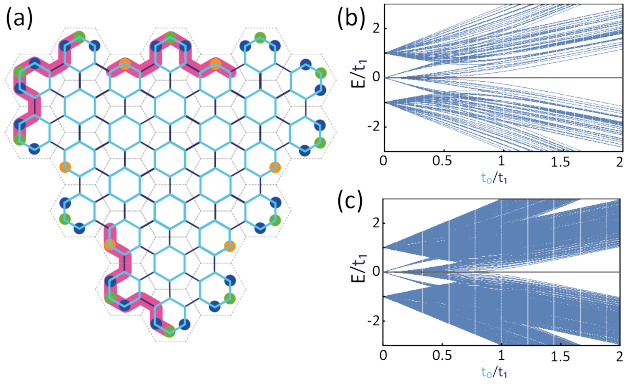

▲ Figure 5.3: **Finite size effects.** (a) Illustration of the finite molecular-zigzag terminated lattice. Green represents protruding sites that couple weakly to two blue sites, orange represents sites sitting in a "cove" at the edge of the lattice. The sections shown in pink have the same local environment. (b), (c) Energy spectrum as a function of t_0/t_1. The spectrum is shown for the system size used in the experiments with 28 hexagons in total (b) and for a theoretical structure that has the same corner and edge, but contains 163 hexagons ((c)).

5.5 Conclusion

In conclusion, we have experimentally realized four lattices by nanoscale patterning of CO adatoms on the surface state of Cu(111) using the tip of an STM. Kekulé lattices with two different bulks and two types of edge termination were realized to

investigate the influence of the boundary shape on the existence of topological edge modes in crystalline topological insulators. We found that for the same bulk, edge modes exist or not, depending on the termination of the sample. The detection of edge modes in this finite-size system is surprising. In translationally invariant ribbons, the mirror and chiral symmetries pin the edge modes to zero energy at the Γ point in the Brillouin zone. However, here we investigate a finite and relatively small system, without translational symmetry and for which a Brillouin zone cannot be defined. Furthermore, in the $t_1 < t_0$ regime chiral symmetry is not strictly enforced due to a non-zero NNN hopping, and the mirror symmetry is not globally preserved. This indicates that the edge modes are remarkably robust to weak symmetry breaking and finite-size effects.

Our experimental observations, which are corroborated by theoretical calculations in the continuum (muffin-tin) and in a discrete lattice (tight-binding model) confirm that the existence of a topological phase in symmetry protected topological insulators is a subtle issue. It does not depend uniquely on the form of the bulk, and sets a boundary of validity to a naïve interpretation of the bulk-boundary correspondence. Our results indicate that devices made from the same bulk, in which the termination is adjusted accordingly, could be used to create valves and manipulate the edge modes at will. Since all the results presented here are generic, they could be promptly transferred to other kinds of condensed-matter setups, in semiconductors or metallic surfaces, thus extending our findings to other kinds of electronic systems. Finally, this work highlights the potential of using artificial lattices to study topological states of matter.

5.6 Appendix: Further details on the Kekulé lattice

5.6.1 Experimental methods

Atomic manipulation, scanning tunnelling microscopy and spectroscopy were performed using a commercially available Scienta Omicron LT-STM. A Cu(111) surface was prepared to atomic flatness by repeated cycles of sputtering with Ar^+ and annealing at approximately 550 °C. Carbon monoxide was then deposited onto the Cu(111) surface within the cooled microscope head at a pressure of 1.3×10^{-8} mbar for 1 minute to achieve a coverage of roughly 0.5 CO molecules per nm^2. Following this, the microscope head was kept at constant UHV (in the range of 10^{-11} mbar) and at a temperature of 4.5 K during construction of the lattices and measurements. An STM tip was cut from platinum-iridium wire, which was conditioned in-situ by repeatedly dipping the tip into the surface and/or applying voltage pulses between tip and sample. This procedure leaves the tip with a randomly shaped apex made from copper atoms, and the process was considered complete when the tip satisfactorily performed the desired task (either atom manipulation, imaging or spectroscopy). STM topographs were acquired in constant current mode. Plane subtraction was performed on the topographs. Atom manipulation was performed with a bias voltage of 20 mV and constant current maintained with a feedback loop ranging from 10 nA to 60 nA depending on the condition of the tip. Differential conductance spectra and maps were acquired in constant height mode with bias modulation provided by a lock-in amplifier. The amplitude of the modulation was 10 mV r.m.s at a frequency of 273 Hz. Integration time for signal acquisition was 50 ms at the lock-in amplifier for spectra and 20 ms for each pixel in the differential conductance maps.

5.6.2 Data processing

The differential conductance spectra were processed by averaging over numerous sites of equivalent type or repeated measurements within the same site, then dividing this average by the average of many spectra on bare Cu(111). The purpose of the division by spectra on bare Cu(111) is to eliminate LDOS contributions from the tip and from the copper itself. Figure 5.4 shows an example of average dI/dV spectra acquired with the same tip on bare Cu(111) and at a position in the edge. Certain aberrations are common in both datasets, for example the dip at 0V. These are features of the tip. In the normalised data, these features have been removed. Processing of the differential conductance maps included alignment of the forward and backwards scans, then averaging the two. A small amount of Gaussian blurring was applied to reduce the appearance of noise in each map, except for the trivial partially bearded edged lattice, for which this was not necessary. The "sky" color map, which is perceptually uniform, was used from the freely available open

source program Gwyddion[381] (with which all experimental image processing was performed).

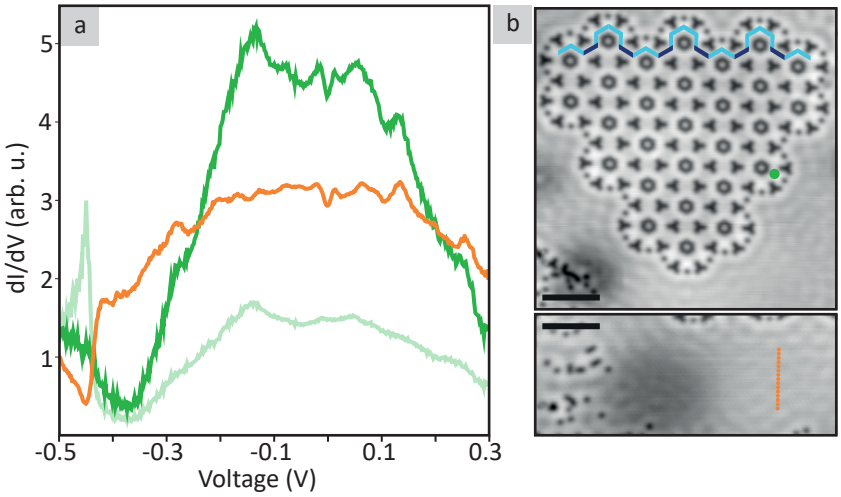

▲ Figure 5.4: **Data normalisation**. a) Bright green: dI/dV acquired on an edge site, averaged over several measurements. Orange: dI/dV averaged over numerous positions on bare copper. Pale green: Normalised and averaged dI/dV at the edge site. b) Positions where spectra were taken marked in corresponding colours. Scale bar is 5 nm.

5.6.3 Theoretical methods

Tight-binding: Finite-size tight-binding calculations were performed to simulate the experimental LDOS spectra and maps. To maximise the accuracy with which we could describe the experimental results, not only the nearest neighbour (NN) hopping parameters were taken into account, but also the orbital overlap and next nearest neighbour (NNN) hopping. To start with, the tight-binding parameters are unknown, which presents an obvious difficulty when trying to model experiments. To estimate these parameters, band structures were calculated using a periodic tight-binding model, and using the muffin-tin approximation (described in the next section). The tight-binding parameters were adjusted until the band structure calculated from it matched that from muffin-tin. These parameters were then inserted into the finite-size tight-binding model to produce LDOS spectra and maps, which ultimately parallel the experimental observations.
To produce realistic spectra and maps from the finite-size tight-binding model, sev-

eral things were taken into account. The first effect is the broadening of the peaks in the experimental differential conductance spectra, arising dominantly from the finite lifetime of surface electrons. The presence of CO molecules allow an additional means by which the surface electrons can enter bulk states, which decreases the lifetime of surface electrons and broadens the LDOS. The extent of the broadening depends on the concentration of CO molecules in the immediate vicinity of the measurement; the more CO molecules per unit area, the larger the broadening. Here, we use a broadening of 80 meV.[230,279,288,357] Without broadening, the local density of states (LDOS) for an energy ϵ is determined by the wave function Ψ and given by

$$\mathrm{LDOS}(x, y, \epsilon) = \sum_i |\Psi_{\epsilon_i}(x, y)|^2 \delta(\epsilon - \epsilon_i), \qquad \text{(Equation 1)}$$

where i iterates over the energies. The broadening can be described by replacing the delta function in Equation 1 by a Lorentzian. The LDOS is now described by

$$\mathrm{LDOS}(x, y, \epsilon) = \sum_i |\Psi_{\epsilon_i}(x, y)|^2 \frac{b}{(\epsilon - \epsilon_i)^2 + (\frac{b}{2})^2}. \qquad \text{(Equation 2)}$$

where $b = 0.08$ eV in this setup. A second significant effect is orbital overlap, which describes the non-zero overlap between the orbitals of neighboring sites. This leads to the generalised eigenvalue equation $H\Psi = ES\Psi$, where H is the Hamiltonian, E is the energy, and S is the overlap matrix. In order to limit the number of parameters to match and to avoid overfitting, we only considered NN overlap. Thus, there are two orbital overlap parameters for each design: the orbital overlap of two sites in the same hexagon, and overlap between sites of two different hexagons. If all orbitals are orthogonal, the generalised eigenvalue equation reduces to the standard eigenvalue equation, $H\Psi = E\Psi$.
Finally, NNN hopping was also included. This again gives two extra parameters, NNN hopping within and between hexagons. The magnitude of both NNN parameters in the $t_1 > t_0$ lattice are small due to the use of clusters of CO molecules. In the $t_0 > t_1$ design, however, a single CO molecule is used in the centre of the hexagon, resulting in a non-negligible intra-hexagon NNN hopping of 0.2 t_0.
LDOS maps were obtained from the tight-binding eigenvectors Ψ_ϵ with energy ϵ according to:

$$\begin{aligned} \mathrm{LDOS}(x, y, \epsilon) \quad = \quad & \sum_{\epsilon'} | \sum_i \exp\left[-(x - x_i)^2 1.15a\right] \\ & \times \Psi_{i,\epsilon}(x, y)|^2 L(\epsilon - \epsilon'), \end{aligned}$$

where a is the lattice constant of the Kekulé lattice, L is the Lorentzian broadening function, i enumerates the sites and x_i is the position of site i.

Muffin-tin: The CO molecules in each lattice were approximated as disk shaped "protrusions" in an otherwise constant 2D potential landscape. This is the foundation of a muffin-tin calculation. For the calculations done here, a disk diameter of 0.6 nm (based on observation from STM scans) and a potential height of 0.9 eV were used to describe the CO molecules, as used by Slot et al.[230]
The periodic tight-binding Hamiltonian was expanded up to the 5th Fourier component in the plane wave basis, making use of Bloch's theorem. This was then solved numerically using the analytically known Fourier components of the muffin-tin potential.[382] The resulting band structures were then used to identify the tight-binding parameters (see figure 5.5, where the muffin-tin band structure and the corresponding tight-binding match are shown for both designs used).

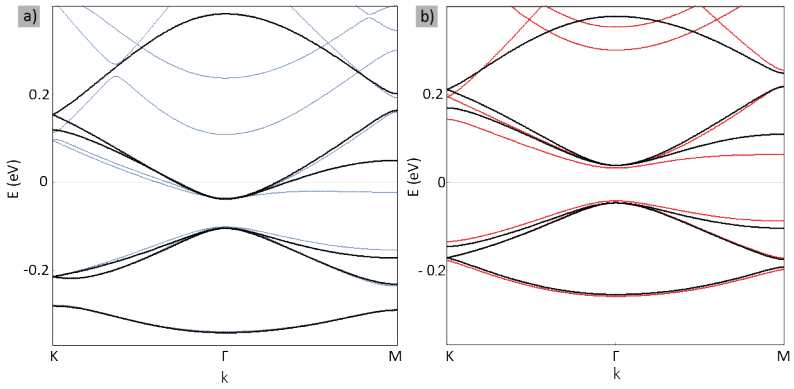

▲ Figure 5.5: **Band structure for the periodic Kekulé lattice**. (a) $t_1 < t_0$ and (b) $t_0 < t_1$. The tight-binding fit is displayed in black, and the muffin-tin band structure in colour (blue and red, respectively).

When comparing muffin-tin and tight-binding derived band structures, the low energy bands match each other well. For the bands at higher energy, the match becomes less accurate due to the interference with p-bands that are not included in the tight-binding description, but are present in the muffin-tin model. The tight-binding parameters that were obtained from this procedure are displayed in Table 5.1.

The experimental results (LDOS spectra and maps) were also simulated using the muffin-tin model. For a finite system, we numerically solved the non-interacting

Design	t_0	t_1	t_{n_0}	t_{n_1}	s_0	s_1	e
$t_1 < t_0$	-0.13 eV	0.7 t_0	0.2 t_0	0.02 t_0	0.2	0.12	-0.105 eV
$t_0 < t_1$	0.67 t_1	-0.13 eV	0	0	0.1	0.15	-0.005 eV

Table 5.1: Tight-binding parameters obtained by matching to muffin-tin band structures. Here, e is the on-site energy, t_0 and t_1 are NN hopping parameters, t_{n_0} and t_{n_1} are NNN hopping parameters, and s_0 and s_1 are orbital overlaps, each of them intra- and inter-hexagon, respectively.

Schrödinger equation for the muffin-tin potential. A flat potential landscape surrounds each lattice, and the edges of the defined area are given by von Neumann boundary conditions. After including broadening in the same way as for the tight-binding model described above, we find that the muffin-tin results closely match the experimental findings, as shown in figure 5.6 for the local density of states maps and in figure 5.7 for the local density of states spectra. In these figures, tight-binding results have also been included for comparison. Spectra on additional edge sites are also included compared to those shown in the main text.

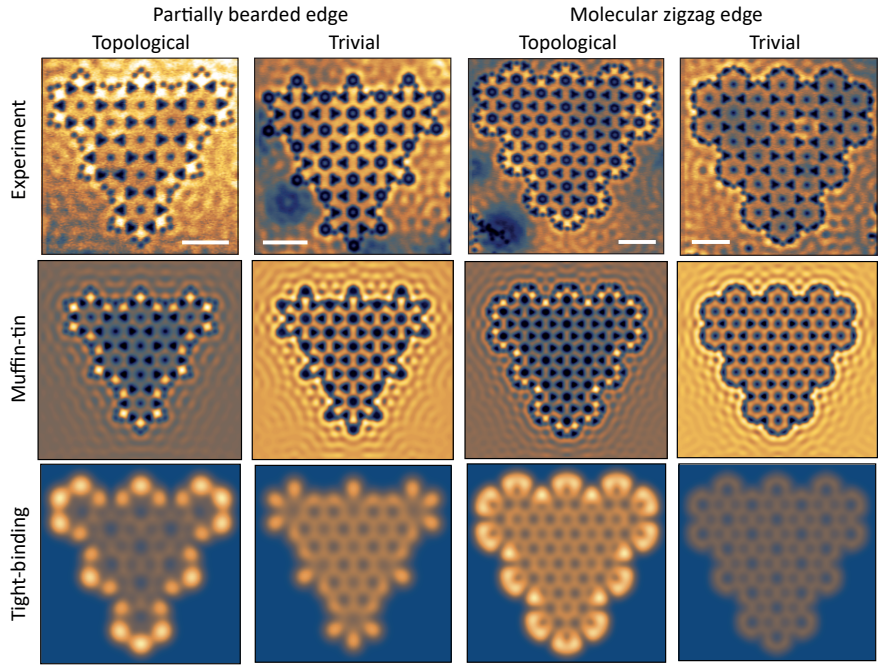

▲ Figure 5.6: **Comparison of LDOS maps.** Local density of states maps at the gap energy for both edge types obtained experimentally (top row), with muffin-tin (centre row) and with tight-binding (bottom row). Scale bars in white indicate 5 nm.

5.6.4 Limiting interactions with the surrounding 2DEG

At the edge of artificial lattices built by confining the surface state of a metal, there can be significant broadening as a result of the states within the lattice interacting with the surrounding free surface state. Minimizing this interaction can be achieved by placing additional CO molecules at the boundaries of the structure. However, care should be taken because the positioning of CO molecules outside their regular anti-lattice may change the on-site energy of edge sites, which could lead to a spurious modulation of the spectrum. In order to find suitable positions to place the "blocker" CO molecules, several potential designs were calculated for each of the four lattices using muffin-tin, and those that yielded the best fit to the tight-binding predictions were chosen. An example using the molecule zigzag edge for $t_0 < t_1$ is shown in figure 5.8. Here, multiple blocker positions (and an edge with no blocking) are shown alongside the corresponding muffin-tin spectra. As before,

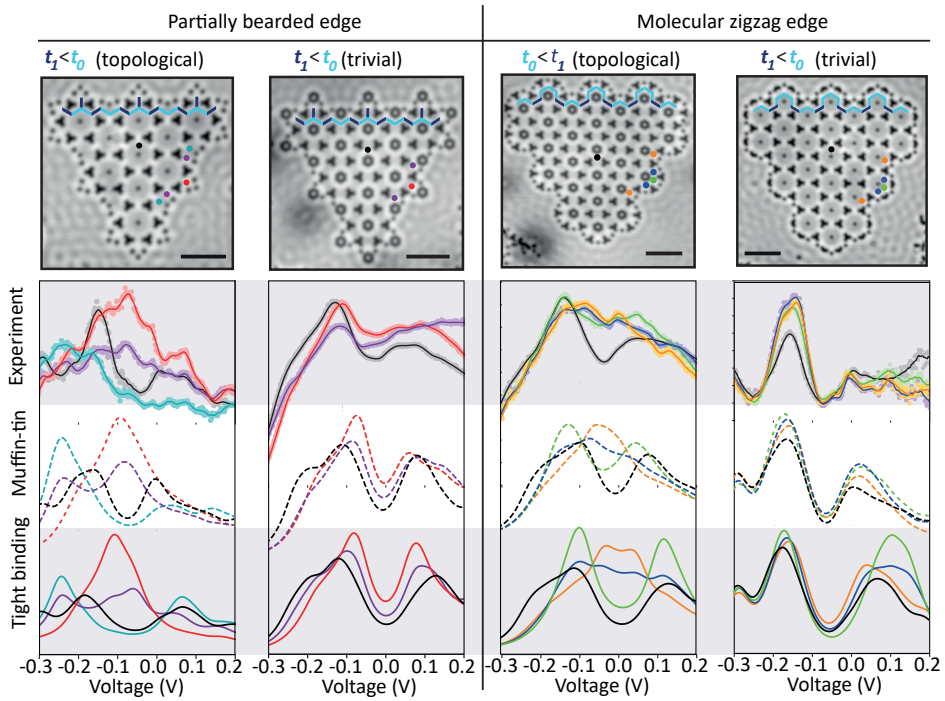

▲ Figure 5.7: **Comparison of LDOS spectra.** Local density of states spectra for both edge types obtained experimentally (top row), theoretically using a muffin-tin calculation (middle row) and with tight-binding (bottom row). The y axis in each plot is the local density of states in arbitrary units. Each colour refers to a type of site, as illustrated in the STM topographs.

broadening of 80 meV was added to each plot to describe the scattering of the surface state to the bulk. The additional broadening as a result of interactions of the edge states with the surrounding 2DEG is plain to see in the LDOS calculated for the design with no blocking (figure 5.8a) – no clear similarities to the tight-binding calculated LDOS are seen. When blockers are introduced too far away as in figure 5.8b, similar behaviour is observed, except the on-site energy of the edge sites are shifted to lower energies because the edge states are less confined. Upon repositioning the blocker-CO molecules one Cu(111) atom distance closer (figure 5.8c), the on-site energies of the sites are shifted towards higher energies. Finally in figure 5.8d, after shifting the blockers one site closer still, the on-site energy becomes approximately comparable to the bulk minimum. Thus, this was the design chosen

for our investigation. Similar calculations were performed for the three remaining lattices to find the best position for CO blockers.

5.6.5 Defects at the edges

One of the most exciting aspects of topological insulators is the resilience of the edge modes to non-symmetry breaking defects. To test this, we introduce CO molecules into the edge to behave as defects. Figure 5.9 shows experimental differential conductance maps, where defects have been introduced. Sites on opposite sides of the defect should only couple very weakly via the defect, possibly affecting the shape of the edge. By examining figure 5.9, it can be seen that the edge modes still exist despite the defects, even in close proximity to them, thus substantiating the topological character of the edge.

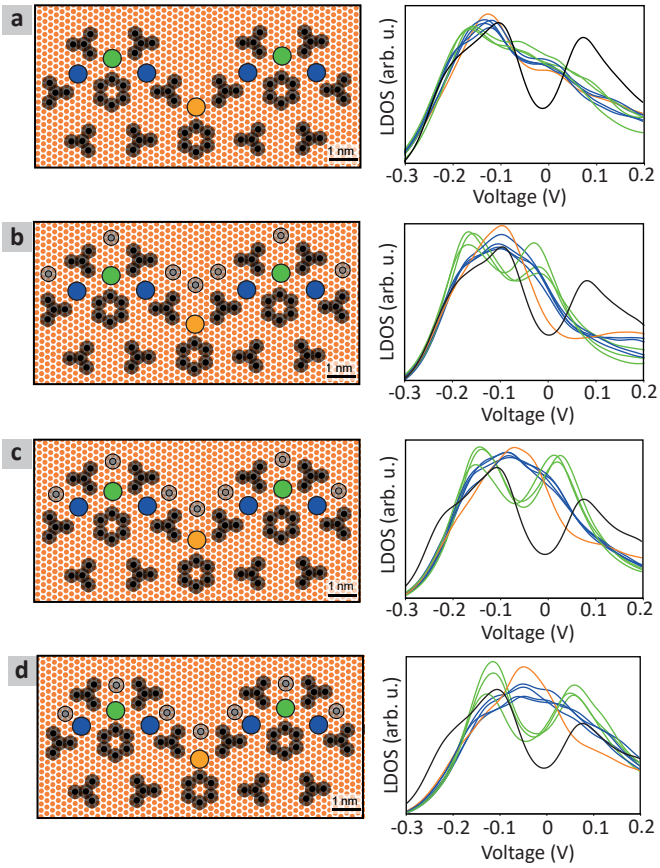

▲ Figure 5.8: **The effect of protective "blocker" CO molecules.** The left column shows positions of CO molecules (black circles) on the Cu(111) surface (orange dots) to form the molecule zigzag edge of the Kekulé lattice. Grey dots represent CO molecules that are used to shield the electronic states in the lattice from unwanted interactions with the surrounding 2DEG. The spectra were calculated on the dots of corresponding colour, except the black line, which was calculated for the bulk. A spectrum was taken for equivalent sites at the corner and edges, thus there are multiple spectra of each colour. (a) The lattice with no blocking CO molecules and the corresponding spectra. (b) Blocking at distant positions, leading to a shift of the edge modes to lower energy. (c) An improvement on (b), where the blocking CO molecules are shifted one Cu(111) atom distance closer. (d) The final design used in our investigation, where the CO molecules are pushed one additional site closer and the on-site energy of the edge mode is comparable to the energy of the bulk gap.

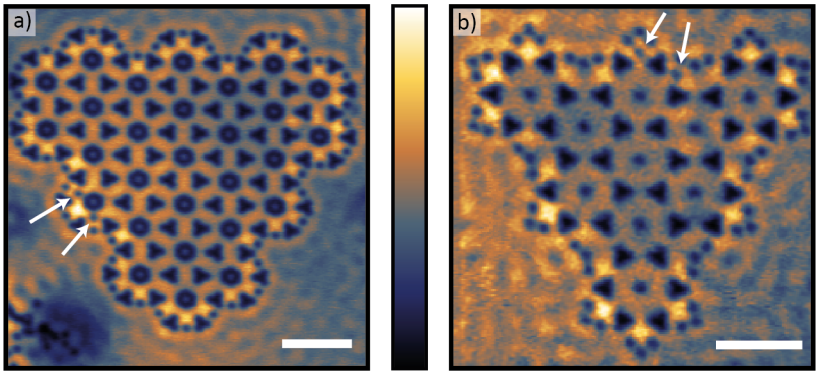

▲ Figure 5.9: **Defects in edges.** Experimental differential conductance maps showing the effect of defects in the edge modes of the lattices. Brighter pixels represent higher LDOS. White arrows point to the defects. Scale bars represent 5 nm. (a) The molecular zigzag edge with $t_0 < t_1$ (acquired at -40mV). (b) The partially bearded edge with $t_1 < t_0$ (acquired at -65mV).

CHAPTER 6

EXPLORING TWO-BODY PHYSICS IN A 1D SSH CHAIN

This chapter was written for this thesis.

6.1 Introduction

In this chapter, we experimentally investigate the marriage of two physical concepts; two-particle interactions and non-trivial topology.

The first ingredient in this investigation concerns bound states. When a bound pair of particles is formed, either through attractive or repulsive interactions, states outside of the allowed single particle bands appear.[383,384] Usually in free space, attractive forces drive the formation of composite objects, while for a repulsive force, the particles diverge from one another. However, in certain environments, such as in a periodic potential, stable composite objects can be formed for repulsive interactions. A doubly-occupied site is known as a doublon. Doublons may manifest as a pair of particles bound in the presence of repulsive interactions. The physics of doublons can be modelled with a Hubbard model for on-site interaction only, or an extended Hubbard model when interactions between particles are present beyond a single site. In the experimental realm, doublons have been directly observed in optical lattices[385] (though not referred to as such). Doublons can exhibit interesting behaviour even without introducing additional physics.[386–389]

The second ingredient in this investigation is non-trivial topology. We make use of the Su-Schrieffer-Heeger (SSH) model for a linear chain, which is well-described for single particles and is known to exhibit topologically protected end states.[58,390] Within the last decade, there has been interest in combining interactions and topology in theoretical studies,[391–396] as well as experimental investigations.[13,397] In combining topology and interactions, one must consider three cases: single-particle topological systems in which interactions (i) do or (ii) do not break the topology; or (iii) systems that are non-topological in the single-particle regime, but in which interactions can result in topological protection, such as the interaction induced topological Kondo insulator[113,395,396] Note that interactions leading to topologically non-trivial states is not a new concept; it is the underlying driver behind the fractional quantum hall effect,[294,398] although sometimes interactions can adversely affect the non-trivial state.[399]

Here, we show a method of experimentally *simulating* two body interactions by making use of a mapping from two particles occupying a 1D chain to one particle on a 2D lattice.[400–402] We realise this 2D lattice using the CO/Cu(111) platform with STM (scanning tunnelling microscopy). The lattice of interest here has a square geometry, with bonds modulated in a fashion akin to the 1D SSH chain. An altered on-site energy along the diagonal of this lattice is analogous to the interaction strength between two particles on one site on the 1D chain. The 2D SSH lattice has been realised before as a higher order topological insulator to manufacture corner modes with excess fractional charge using the same experimental system.[403] In addition to the well-known topological end modes that occur in this lattice, Di Liberto *et al*[395,396] predicted a variety of other phenomena when interactions between particles are considered, such as a Feshbach resonance, a doublon end state,

and an edge bound state that appears at the strongly coupled edge (note that no edge state is found on this edge for single particles). The Feshbach resonance in particular leads to a signature in the 2D analogue of the 1D lattice that is possible to observe in STM, see below.

6.2 The SSH model

The Su-Schrieffer-Heeger (SSH) chain consists of sites coupled via alternating strong (t_s) and weak (t_w) hoppings.
First, we consider a single-particle model. The 1D SSH chain is presented in figure 6.1a. In each unit cell, there are two types of sites that can be distinguished based on their environment. We denote the two sublattice sites A and B. One has a choice to make when defining the unit cell. It could either be centred on a strong bond, with inter-cell bonds being weak, or vice versa by shifting the cell by a single site (blue and green cells respectively in figure 6.1a). The termination of a finite chain differs depending on the choice of unit cell. If the final bond in the chain is weak, an isolated end mode is manifested, and the system is considered topologically non-trivial.[390] If the final bond in the chain is strong, the site at the end is fully coupled to the rest of the lattice, and every site contributes to the bulk spectrum. In this case, the system is considered topologically trivial. We use D_s and D_w to denote configurations that are terminated with strong and weak bonds respectively.

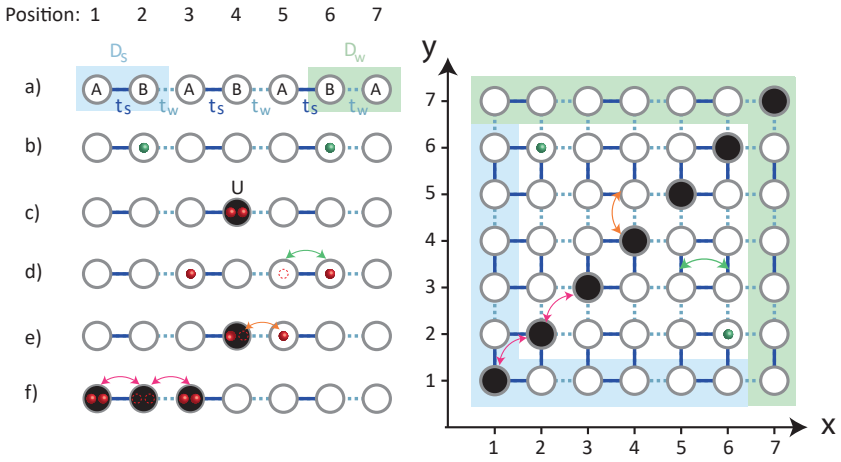

▲ Figure 6.1: Schematic to assess the analogy between the two-body 1D SSH model to the non-interacting 2D SSH model. (a) The 1D SSH lattice labelled with A and B sites coupled with alternating strong (solid line) and weak (dashed line) bonds. The light blue and light green shaded regions on the 1D chain highlight the two unit cell definitions that would give rise to termination in strong or weak bonds respectively. Strongly and weakly coupled edges are highlighted on the 2D lattice (right) in light blue and light green respectively. (b) Positions of two particles on sites 2 and 6 on the 1D lattice are analogous to site $x = 2, y = 6$ on the 2D lattice, and, since the particles are indistinguishable, $x = 6, y = 2$ also. These are indicated by green spheres. (c) The on-site interaction between two particles is given by U and represented in black. This is also the on-site energy of a single-particle state on the diagonal of the 2D lattice (right), with respect to the on-site energy of off-diagonal sites. (d) Single particle hopping (green arrow) in the 1D case is represented by off-diagonal hopping in 2D. (e) When a particle hops out or into its on-site doublon state in 1D, this is represented by hopping from/to a diagonal site to/from an off-diagonal site in 2D (orange arrow). (f) Hopping of the entire doublon in 1D is represented by hopping along the diagonal in 2D (magenta arrow).

If we use an odd number of sites in the chain, then we obtain both terminations. Here, we consider chains of 7 sites.

The 1D SSH chain with two particles can be described by a Hubbard Hamiltonian, $H_0 + H_U$. The following description with full details can be found in reference 14.[395] H_0 is the kinetic term, and corresponds to the Hamiltonian of the non-interacting

system.

$$H_0 = -t_s \sum_i c^\dagger_{A,i} c_{B,i} - t_w \sum_i c^\dagger_{A,i+1} c_{B,i} + H.c. \tag{6.1}$$

where $c^\dagger_{X,i}$ and $c_{X,i}$ are the creation and annihilation operators for an electron on lattice site $X = A, B$ within cell i. H_0 describes the D_s case; strong (in-cell) hopping from site B to site A, and weak (inter-cell) hopping from site B to site A in the preceding cell. *H.c.*, the Hermitian conjugate, describes the particle "hopping" in the reverse direction.
H_U describes an on-site potential due to the electrostatic repulsion between two particles at that site. The on-site interaction is described by

$$H_U = \frac{U}{2} \sum_i (c^\dagger_{A,i} c^\dagger_{A,i} c_{A,i} c_{A,i} + c^\dagger_{B,i} c^\dagger_{B,i} c_{B,i} c_{B,i}), \tag{6.2}$$

where U is the on-site interaction strength. Note that the two electrons considered must have opposite spins in order to occupy the same lattice site.
In the fully dimerised case $t_w = 0$, the Hamiltonian consists of three different states; where both particles exist on site A, where one particle exists on A and one on B, or where both particles exist on B. We let the Hilbert space of this in-cell Hamiltonian be spanned by $|A_i A_i\rangle$, $|A_i B_i\rangle$ and $|B_i B_i\rangle$, which respectively correspond to the aforementioned states. When considering only on-site and nearest neighbour interactions, the two-particle Hamiltonian is given by

$$H_i^{cell} = \begin{pmatrix} U & -\sqrt{2}t_s & 0 \\ -\sqrt{2}t_s & 0 & -\sqrt{2}t_s \\ 0 & -\sqrt{2}t_s & U \end{pmatrix} \tag{6.3}$$

which corresponds to three dimer states, d_α, with energies $\epsilon_{1,3} = \frac{1}{2}(U \mp \sqrt{16t_s^2 + U^2})$ and $\epsilon_2 = U$. These are bound states. When t_w is finite, these states delocalize and form narrow bands.
To calculate the band structure, the Lippmann-Schwinger equation is used, which allows one to calculate scattering of quantum states.[404] The kinetic part of the Hamiltonian (equation 6.1) can be transformed into a basis that depends on what could be considered a centre of mass between two particles on the chain. If particle 1 is at position x on the chain and particle 2 on position y, this maps to a single particle on a 2D lattice at position (x, y), and the Hamiltonian is equivalent for both, see.[395,396] An example is given for two particles (green) in figure 6.1b and their equivalent position on the 2D lattice for $x = 2, y = 6$ and $x = 6, y = 2$. The on-site interaction in the 1D chain, where both particles are on the same site (figure 6.1c), maps to a modified potential along $x = y$ in the 2D lattice. This potential is labelled U, and is given with respect to the off-diagonal sites. A single particle hopping from one site to the adjacent site is represented by the green arrow in figure

6.1d. This is mapped to off-diagonal interactions in the 2D lattice. A single particle hopping out of or into its on-site doublon state in 1D (orange arrow, figure 6.1e) is represented in 2D as hopping between a site on the diagonal and an off-diagonal site. Doublon hopping in 1D is represented by hopping along the diagonal in 2D (magenta arrows, figure 6.1e).
The non-interacting SSH model produces three scattering continua, which Di Liberto *et al* label type I.[395] Two additional continua are generated for D_w around energies $\pm t_s$, labelled type II. These type II continua correspond to states of two particles, consisting of one particle localised at the edge (which is only permissible on D_w, not D_s) combined with a freely propagating particle along the 1D chain. In this scenario, one can imagine a dynamic process whereby the first particle travels towards the weakly coupled edge where the second particle is localised. Once it arrives, the two particles may form an edge bound pair if the bound pair energy is aligned with the scattering continuum corresponding to the initial state. The two particles can then travel back into the bulk of the chain together as a bound pair. Figure 6.2 shows a spectrum calculated for the D_w case as a function of U/t_s, where the five (types I and II) scattering continua (black) are visible, along with bound states (green in the left figure) which vary in energy as U (the interaction strength between two particles) is varied. The degree to which the bound pair is localised at the edge is conveyed by the shade of green; lighter means more localised at the edge. At the condition $U = t_s$, the bound state with second-lowest energy crosses a type II scattering continuum, resulting in a mixing of states corresponding to the aforementioned dynamic process. This is known as a Feshbach resonance, which is a resonance between bound states and free scattering states.[405] The free states in this case are the aforementioned pair of particles that give rise to type II continua, and the bound states are the result of when the two particles meet.
By considering the mapping from 1D to 2D (see figure 6.1), one may deduce the equivalent picture of the dynamics in 2D. The resonance can be envisaged as two particles (one on each of the weakly bound edges), moving along the edges and meeting each other at the weakly bound corner. There, it forms a bound pair which then travels along the diagonal of the lattice. A wavefunction map of this resonance is shown inset on the right of figure 6.2. This translates to an elevated local density of states along the diagonal and along the weakly coupled edges at the same energy, which is observable with scanning tunnelling spectroscopy measurements. Note that the signature of the Feshbach resonance should only be observed within some margin of $U = t_s$ (the bands have a certain width, so the condition does not have to be exactly met to see the resonance).

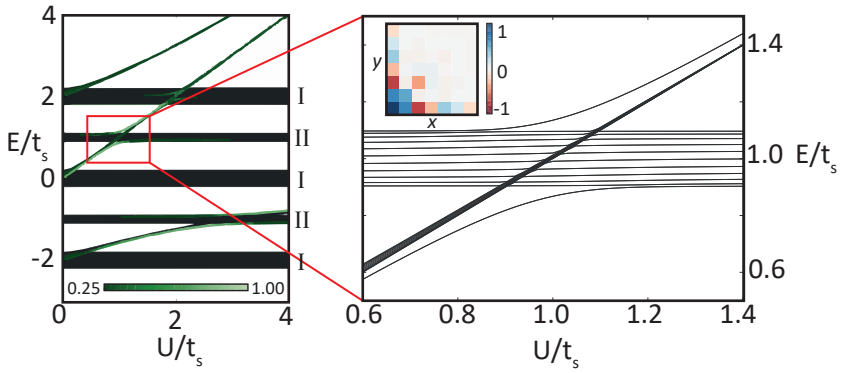

▲ Figure 6.2: **Energy spectrum of the D_w system calculated using exact diagonalisation and open boundary conditions, for $t_w = 0.1t_s$.** Energy is plotted as a function of U/t_s. Left: There are five scattering continua (black horizontal lines). The bound states (green) vary in energy as U is varied. The green colour bar represents the density of states in the first two lattice cells and highlights the localization of edge bound states. The energy region of interest in our experiment is enclosed in the red rectangle. This is where the second lowest bound state intersects the scattering continuum shown. Right: Zoomed in region of interest of the spectrum. Inset shows a calculated wavefunction map of the bound state of interest for $U = t_w$ and energy $E \approx 0.8t_w$ obtained also through exact diagonalisation. x and y extend to 7 lattice sites here. This figure has been adapted with permission from Di Liberto,[395]

6.3 Methods

To realise the 2D variant of the SSH lattice, we used the CO on Cu(111) system, whereby the CO molecules act as scattering centres for the Cu(111) surface state electrons. Each electronic site is a pool of surface electrons that have been confined by the CO molecules.[6,234] These electronic sites can be coupled to one another, and the hopping strengths can be tailored by altering the positions of CO molecules between sites.[234] This system has demonstrated in recent years to be useful to investigate electronic behaviour within engineered potentials.[7,230,279,287,288,357,406]

Figure 6.3a shows the bond layout and figure 6.3b shows the placement of CO molecules used to define the electronic sites. Different gap widths between CO molecules allow for strong or weak coupling, as discussed in chapter 4 and reference 29.[234] An STM

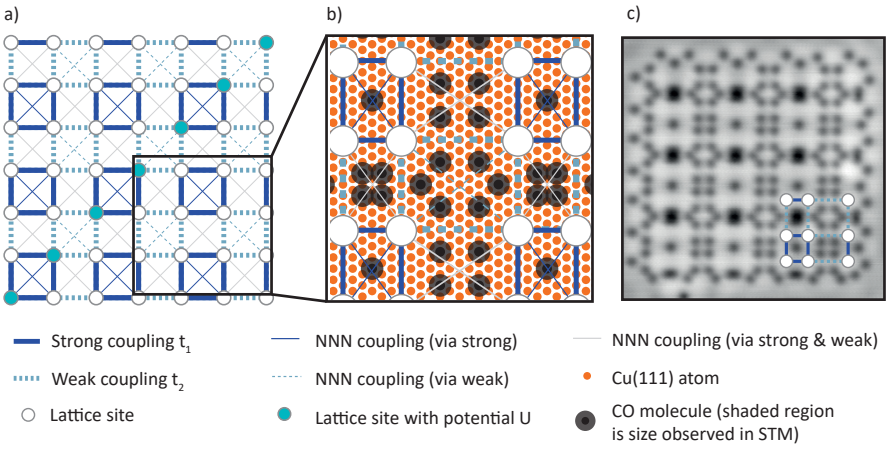

▲ Figure 6.3: **The lattice design.** (a) The full bond arrangement throughout the lattice. The potential U is altered. (b) Diagram of how the CO molecules are to be arranged atop the Cu(111) surface to produce the lattice with weak and strong bonds. (c) An STM scan of a 7×7 lattice with diagonal sites equivalent to bulk sites, i.e. $U = 0$. The CO molecules confine the electrons that constitute the artificial lattice sites.

scan of the complete 7×7 structure is shown in figure 6.3c. The top and right sites are connected weakly to the rest of the lattice, while the bottom and left sites are connected strongly. To change the on-site energy of sites along the diagonal, extra CO molecules were added to strengthen the confinement of the electronic states. This elevated on-site energy compared to the on-site energy of the surrounding sites simulate the on-site interaction between two particles on the 1D chain. Ultimately, we produce four variations of different U, see figure 6.4. In order of increasing on-site energy, we label them $U0$, $U1$, $U2$ and $U3$. $U0$ represents the lattice with the diagonal sites at the same on-site energy as the bulk sites.

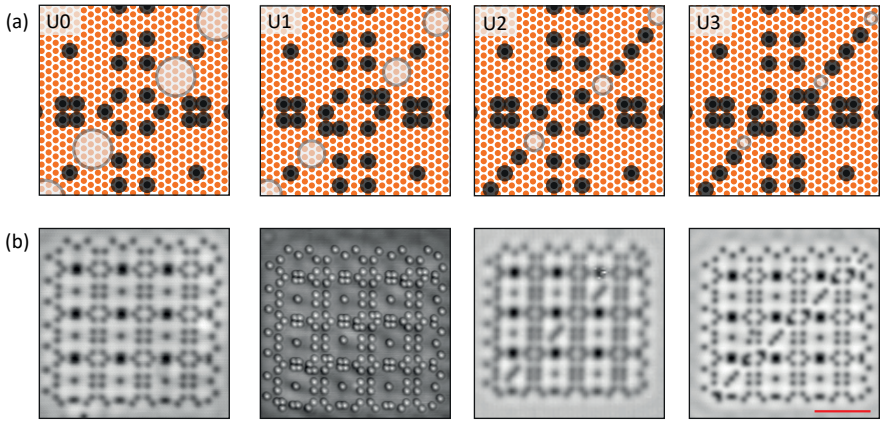

▲ Figure 6.4: **Realising the system with CO on Cu(111).** (a) Diagrams of CO placement that confines electrons along the diagonal for each different U. The white/grey circles loosely represent the size of the electronic sites along the diagonal. (b) STM topographs of the fully realised lattices with different U. The image of the $U1$ lattice was acquired with a CO tip, thus the CO molecules appear as protrusions rather than dips. The red line in the $U3$ image represents 5 nm.

6.3.1 Calculations

To help find a configuration of CO molecules that would lead to the desired physics, muffin-tin calculations were performed. From such calculations, one can predict the LDOS at each position in the lattice. Numerous designs were considered before settling on the one shown in figure 6.3b.

Sites at the edge of the lattice require additional CO molecules for two reasons. Firstly, to reduce broadening due to interaction with the surrounding 2D electron gas (see e.g.[406]). Secondly, to make sure there is no shift of on-site energy due to a difference in size of an edge site compared to a bulk site (the on-site energy of an electronic site is inversely proportional to its size[234]). In addition to aiding the principal design, muffin-tin calculations were used to find the best positions for these outer CO molecules that (partially) block interactions with the surrounding 2DEG. They were chosen in such a way as to align spectra at the edges with spectra in the bulk.

In these calculations, cylindrical potentials of height 0.9 eV and radius 0.31 nm were used to model CO molecules. The band minimum of the Cu(111) surface state was set to -0.445 eV. The effective electron mass was assumed to be 0.42 m_e. Ar-

tificial broadening of 40 mV (full width at half maximum) was applied. The LDOS plots generated from these muffin-tin calculations can be compared to experiment, and in previous work, has modelled the results quite closely.[230,234,279,288,357,403,406] Muffin-tin calculations also allow us to estimate the tight-binding parameters for the lattice we built. To find the tight-binding parameters, a band structure calculated with the muffin-tin approach was compared to the band structure calculated with the tight-binding approach. This was done for the periodic lattice with all sites at potential $U0$. The tight-binding Hamiltonian is identical to the one found in.[403] The tight-binding parameters were adjusted until an adequate fit was found. Figure 6.5 shows the final fit compared to the muffin-tin-derived band structure. Three types of next-nearest neighbour coupling were included to find the best fit. These are next-nearest neighbours (NNN) coupled "via" two strong bonds, two weak bonds, or one weak and one strong bond, see figure 6.3b. The tight-binding parameters for the basic lattice were estimated as follows.

Parameter	**Value**
On-site energy	-0.135 eV
Weak hopping t_w	0.031 eV
Weak overlap	0.08
Weak NNN hopping t_w	0.005 eV
Strong hopping t_s	0.072 eV
Strong overlap	0.08
Strong NNN hopping	0.015 eV
Other NNN hopping	0.005 eV

The on-site energy here refers to off-diagonal sites, i.e. those which have not been modified. The "other" NNN hopping refers to hopping via one weak and one strong bond, see the thin grey lines in figure 6.3.
As mentioned earlier, the condition at which a mixing of states leads to a Feshbach resonance is at $U = t_s$. The strong hopping found here was 0.072 eV, thus we expect the Feshbach resonance at $U = 0.072$ eV. Since U is defined relative to the on-site energy of bulk sites, the on-site energy of sites along the diagonal should be 0.072 eV + -0.135 eV = -0.063 eV.

6.3.2 Experimental procedure

Experiments were performed using a Scienta Omicron LT-STM at pressures below 10^{-10} mbar and a temperature of approximately 4.5 K. The Cu(111) was cleaned by repeated cycles of sputtering with Ar^+ and annealing at 550° C. Carbon monoxide was deposited onto the Cu(111) surface while the sample was in the microscope head at 4.5 K. Differential conductance spectra and maps were acquired in constant height mode. The modulating bias was provided by a lock-in amplifier, using an amplitude of 10 mV r.m.s., a frequency of 273 Hz, and an integration time of 50

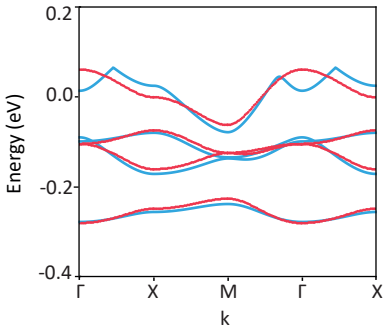

▲ Figure 6.5: **Finding the tight-binding parameters.** The lowest four bands of the periodic 2D SSH system with no modification of diagonal sites ($U0$) are shown. The blue lines represent the muffin-tin calculation. The red lines represent the tight-binding calculation with optimised parameters.

ms per point for spectra and 20 ms per pixel for maps. Each spectrum shown has been averaged over varying numbers of spectra on equivalent sites. Macroscopically speaking, the same tip was used for all experiments, but the tip apex changed unavoidably on the nanoscale during measurements. The differential conductance measured depends on states in the sample as well as those in the tip.[407] To reduce the effect that the tip state has on the measurement, we divided the spectra taken by the average Cu(111) spectrum acquired with the same tip.[7]

6.4 Results and discussion

Differential conductance spectra were measured experimentally and calculated with muffin-tin at each electronic lattice site, for each of the four lattice variations. The spectra can be separated by type, see the colour-labelled STM topograph in figure 6.6. The bulk and edges of the lattice are the same for all diagonal variations, while the diagonal sites, upper right and lower left corner sites have different on-site energy for each configuration. The colours in figure 6.6 represent the positions at which the averaged muffin-tin LDOS and averaged, normalised (divided by bare Cu(111) spectra) experimental $\frac{dI}{dV}$ were obtained. Differential conductance maps were also acquired experimentally and calculated with muffin-tin. In the following sections, we go into further detail on these results.

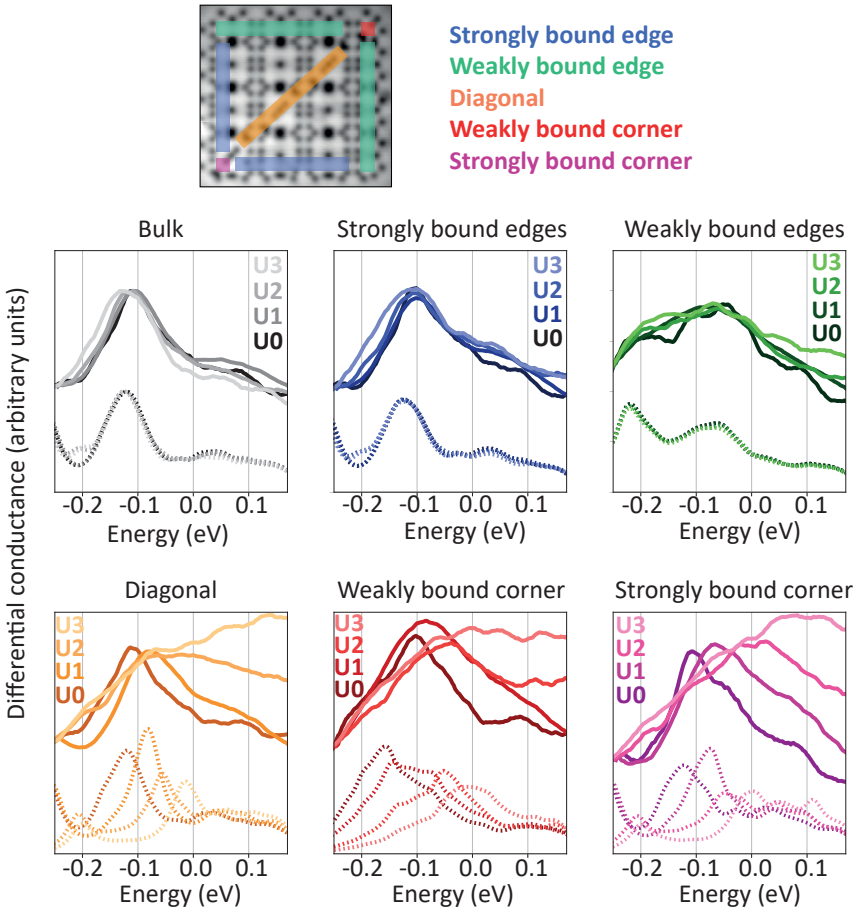

▲ Figure 6.6: **Spectra per site type.** The top figure shows an STM topograph of the $U3$ lattice as a visual aid, with colours overlaid. Below, the calculated and experimentally acquired spectra correspond to these colours. The solid lines are experimentally acquired differential conductance spectra and the dashed lines represent LDOS calculated using muffin-tin. For each site type, the four different diagonal on-site energies (U) are represented by shades (brightness) of colour. The experimental differential conductance has been scaled in such a way that the value of differential conductance is approximately the same at -0.25 eV for each value of U.

6.4.1 Examination of the LDOS spectra

The experimentally acquired differential conductance spectra are the upper spectra shown as solid lines of each plot in figure 6.6. The local density of states (LDOS)

calculated using the muffin-tin model are the lower spectra shown as dashed lines in figure 6.6.

We observe from the muffin-tin LDOS that spectra on bulk (black/grey) and edge (blue and green) lattice sites do not vary in shape or magnitude when varying U. This is intuitive as locally, these sites remain identical upon changing U. In addition, spectra on the strongly bound edge (blue) and the bulk (black/grey) closely resemble one another. In both, the highest peak is at approximately -0.13 eV. This holds true for the experimentally measured spectra. This similarity can be attributed to the fact that the connectivity of the sites is similar.

The spectra on the weakly coupled edge sites are expected to have two peaks, which are in fact visible in the muffin-tin calculated spectra (green dashed lines, figure 6.6). These two peaks are attributed to the fact that these sites are only weakly connected to the rest of the lattice, and couple mainly to each other via a strong bond, which yields dimer-like behaviour/a Peierls distortion. In the experimental spectra measured at the weakly coupled edge sites, these two peaks are only visible for the $U0$ lattice. In the $U1$, $U2$ and $U3$ lattices, there is too much broadening to resolve the two peaks with certainty. Note that the resonance observed in these spectra is much broader than the resonance observed in spectra on bulk sites. We expect that the weakly coupled edges would yield the same spectrum for all U, however, while their overall positions do not shift much from one another, the shape of each spectrum is quite dissimilar, suggesting a tip effect. This could be due to imperfect background division of the spectra (e.g. due to tip changes during the experiment). The presence of highly mobile contaminants in the measurement chamber at the time of the experiment could also have influenced the measurements, see the appendix of this chapter for details.

The rest of the sites; the diagonal, weakly bound corner and strongly bound corner; are those that change depending on U. In the lower three plots of figure 6.6, the peaks in the diagonal, weakly and strongly bound corner spectra shift rightwards (to higher energy), both for experimental and muffin-tin derived LDOS. Increasing U is represented by increasingly lighter colours. Recall that U is increased by confining the diagonal sites with extra CO molecules. In the 1D picture, U represents an on-site doublon interaction, which increases from $U0$ to $U3$. At a certain point, the doublon bound state crosses the scattering continuum, resulting in a Feshbach resonance. As mentioned earlier, this should occur when U is 0.072 eV greater than the bulk on-site energy. This would be in the region of -0.063 eV (with some leeway, given that there is a particular bandwidth associated with the scattering continuum, and also that there exists broadening in the experiment). figure 6.7 shows LDOS acquired only at the bulk, weakly coupled edge and diagonal sites. It can be observed that spectra on diagonal sites (orange) shift upwards with increasing U, and the higher peak overlaps the higher peak of the weakly bound edge in the $U1$ or $U2$ case, which occurs close to -0.063 eV in both cases. This is the signature of the Feshbach resonance.

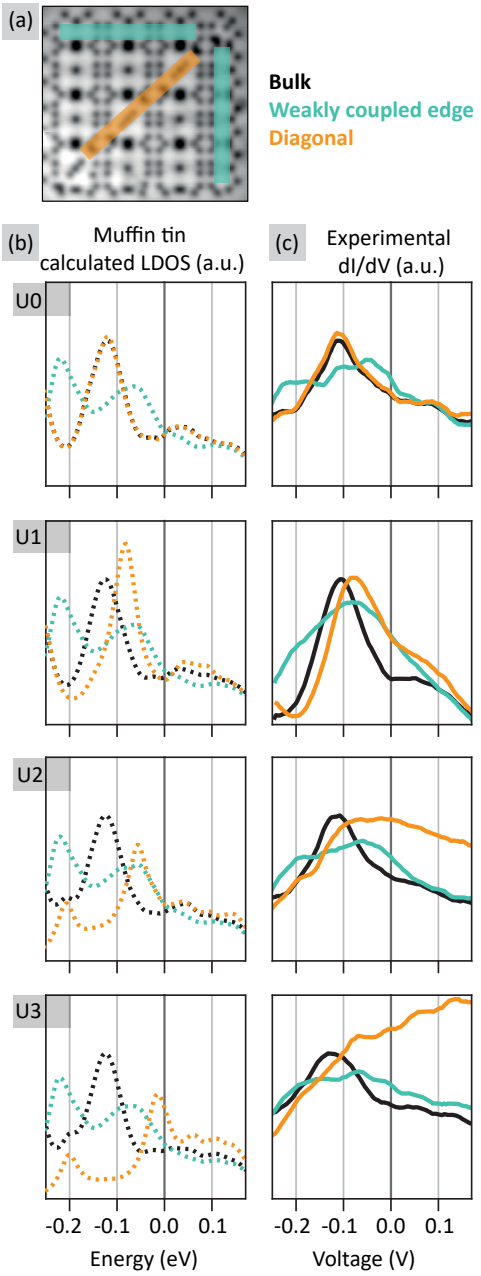

◀ Figure 6.7: (a): STM scan of the lattice with overlaid colour scheme representing the positions where spectra were acquired.
(b): LDOS as a function of energy at the positions corresponding to the marked colours, averaged over sites of the same type and calculated using the muffin-tin model.
(c): Experimentally acquired $\frac{dI}{dV}$ spectra averaged over sites of the same type, and divided by the average spectra acquired on clean Cu(111).
For the calculated spectra, the y-axis is the LDOS, and for the experimental spectra the y-axis is $\frac{dI}{dV}$, both in arbitrary units. The x-axis is the same for all plots and defined at the bottom

A note about broadening

There is considerable broadening in all spectra which is seen to increase for the diagonal sites when U is increased. This is an expected phenomenon that occurs either because the additional CO molecules mediate scattering of surface electrons to the bulk, thereby reducing their lifetime, or because surface electrons with higher energy are less confined within the finite potential barrier formed by the CO molecules, see chapter 4 of this thesis as well as references 29 and 38.[234,408] In spite of this, some observations can be made. One clearly observes that the on-site energy of diagonal sites increases as U is increased, and remains unchanged for off-diagonal sites. A signature of the Feshbach resonance is observed for configuration $U1$ or $U2$.

6.4.2 LDOS maps

Figure 6.8 shows LDOS maps produced with muffin-tin. The energies that the maps were generated for are those where there is a peak in LDOS on specific parts of the lattice. All variations of the lattices are shown. The first and third columns contain maps produced at approximately the energies of the two peaks of the weakly bound edge spectrum, -0.22 eV and -0.06 eV, both highlighted in green. As explained earlier, sites at the weakly bound edges appear as a series of dimers aligned along the edges - the maps at -0.22 eV and -0.06 eV appear to show the bonding and antibonding orbitals of these dimers, respectively.
Sandwiched in between these two columns are LDOS maps at -0.12 eV, corresponding to to the bulk and strongly bound edge peaks, highlighted in black.
The maps highlighted in orange in figure 6.8 are at the energy of U for each lattice. At -0.06 eV, where the Feshbach resonance is expected to lie, the eigenstates of the diagonal and the weakly bound edges co-exist for $U1$. This is an indication of the Feshbach resonance. A similar image is observed for $U2$ at -0.046 eV. This is because the on-site energy of $U1$ and $U2$ are closer than can be resolved with the 40 mV broadening applied.

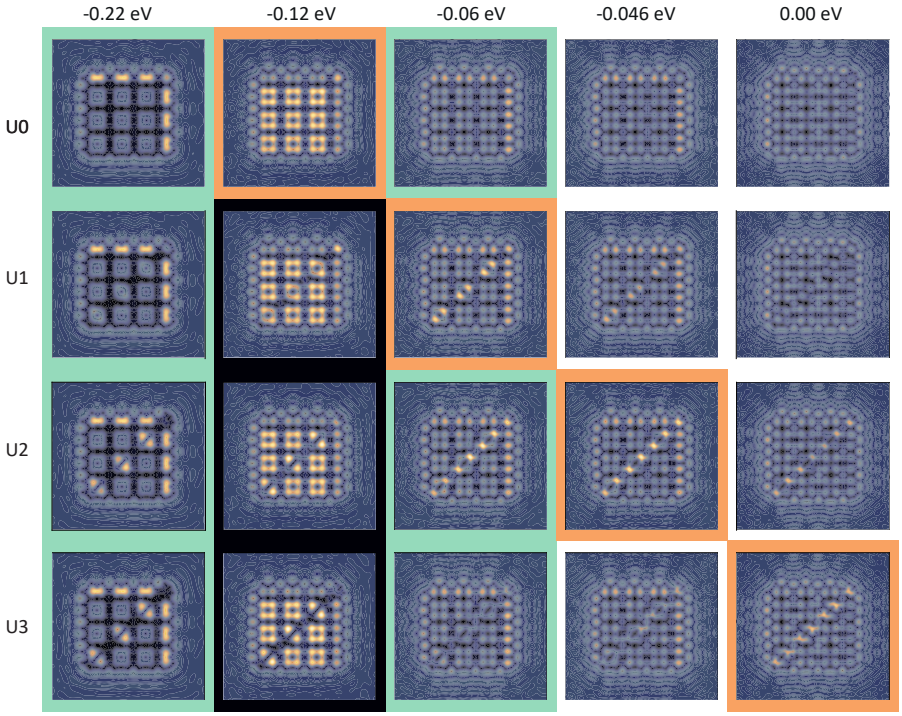

▲ Figure 6.8: LDOS maps calculated using muffin-tin. The energies selected correspond the particular peaks in the spectra (figure 6.7). The two green columns refer to the two peaks in the spectra acquired at the weakly bound edges of the lattice. The black column contains spectra acquired at the energy of the bulk (and strongly bound edge) peak. Orange highlights the on-site energy of the diagonal of each lattice. For $U0$, the diagonal sites are no different from the bulk sites.

Figure 6.9 shows experimentally acquired maps on the $U0$ and $U1$ configurations of the lattice at two different energies. In figure 6.9a, one observes the bonding-like state of the weakly bound edge with reasonable clarity. The gradient in the image is due to use of an incorrect plane during acquisition of this constant-height map. That is to say, the tip was raster scanning in a plane which was at some angle (not parallel to) the plane of the surface during the acquisition of this image. The differential conductance map of the $U1$ lattice is shown in figure 6.9b. Due to the large broadening, a rather homogeneously distributed density of states is observed.

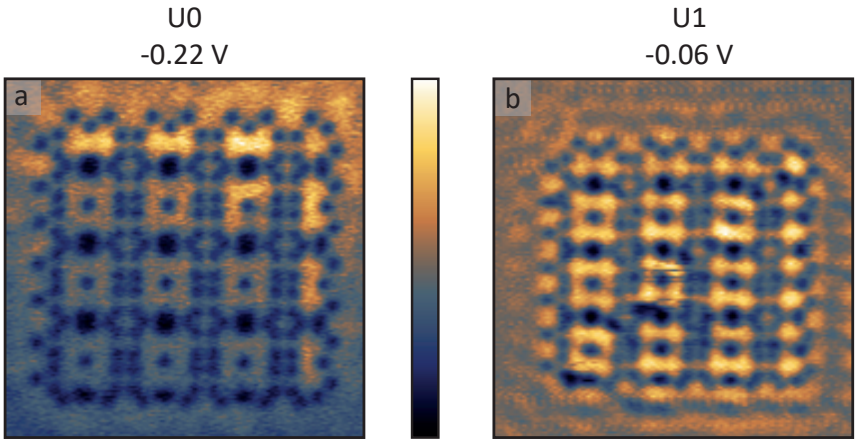

▲ Figure 6.9: 20 nm x 20 nm experimental $\frac{dI}{dV}$ maps of (a) The $U0$ lattice at -0.22 V and (b) the $U1$ lattice at -0.06 eV. No evidence of the Feshbach resonance is observed in (b), likely due to deficiencies of the tip, given that the bonding-like state of the weakly coupled edge is quite clearly visible in (a).

6.5 Conclusion

To conclude, we have attempted to experimentally probe two body interactions in an SSH chain by making use of a mapping to a free particle in two dimensions. We created a 2D SSH lattice with a modified on-site energy along the diagonal to simulate doublon physics in 1D, with the hope of observing the Feshbach resonance that was predicted to arise in this system.[395,396] In muffin-tin calculations, we observe a clear split in energy of the weakly coupled edge due to its dimerisation, and we see that for two values of U, there is overlap between the higher energy of the weakly coupled edge and the onsite energy of the diagonal, which is indicative of the Feshbach resonance. Due to the broadness of the experimental peaks and aberrations in the $\frac{dI}{dV}$ spectra, we see only a hint of this behaviour. To reduce the broadening in a future experiment, one could use larger lattice sites. This would result in a downward shift in energy of all the states, leading to narrower peaks (see figure 4.4 of chapter 4). Alternatively, another material platform could be considered (e.g. monolayer Ag/Si(111))

6.6 Appendix: mobile adsorbates

The presence of mobile adsorbates on the surface could have obscured results during this project. Figure 6.10a shows an STM topograph of the $U3$ lattice. The CO molecules appear as dips in the surface and remain static during the scan as usual. The mobile adsorbates appear brightly across the lattice, as well as elsewhere in the scan. Their structure is not well-defined and the motion of the tip appears to cause them to shift to the left and right, evidenced by horizontal streaks. The chemical identity of such entities remains unknown, but since they are mobile at 4.5 K, possible culprits are hydrogen or helium. The entities typically appeared after performing $\frac{dI}{dV}$ spectroscopy, and were never seen on bare Cu(111), preferring to congregate near clusters of CO molecules (thus were attracted to lattices). Sudden shifts and sharp peaks in $\frac{dI}{dV}$ spectra (figure 6.10b and 6.10c, respectively) were a common occurrence during experiments, and could potentially be attributed to the entities between the tip and sample. In attempts to mitigate these effects, large clusters of CO molecules were constructed close to the lattice to trap the mobile adsorbates, much like the cluster on the left of figure 6.10a, which has already been populated with these adsorbates. The mobile adsorbates could be manipulated from the lattice to the CO clusters using a current setpoint of approximately 10 nA and bias voltage of 20mA without disrupting the CO molecules of the lattice (much).

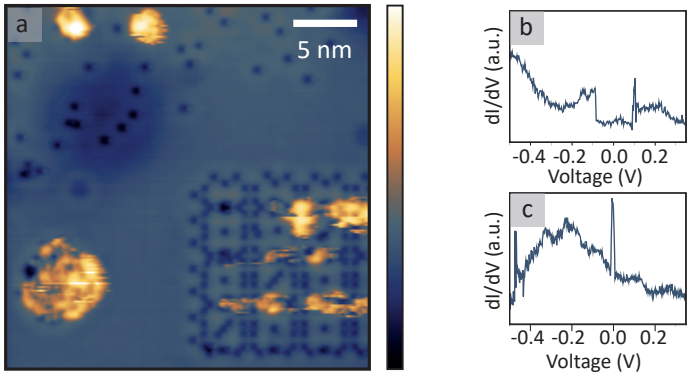

▲ Figure 6.10: **Mobile adsorbates.** (a) Mobile adsorbates are represented as gold amorphous entities in this STM topograph. (b,c) Examples of spectra taken on the lattice exhibiting undesirable features, possibly owing to the entities.

BIBLIOGRAPHY

[1] Thomas Arthur Rickard. The nomenclature of copper and its alloys. *The Journal of the Royal Anthropological Institute of Great Britain and Ireland*, 62:281–290, 1932.

[2] Russell Young, John Ward, and Fredric Scire. The topografiner: an instrument for measuring surface microtopography. *Review of Scientific Instruments*, 43(7):999–1011, 1972.

[3] Gerd Binnig and Heinrich Rohrer. Scanning tunneling microscopy. *Surface science*, 126(1-3):236–244, 1983.

[4] Donald M Eigler and Erhard K Schweizer. Positioning single atoms with a scanning tunnelling microscope. *Nature*, 344(6266):524–526, 1990.

[5] MF Crommie, Ch P Lutz, and DM Eigler. Imaging standing waves in a two-dimensional electron gas. *Nature*, 363(6429):524–527, 1993.

[6] Michael F Crommie, Christopher P Lutz, and Donald M Eigler. Confinement of electrons to quantum corrals on a metal surface. *Science*, 262(5131):218–220, 1993.

[7] Kenjiro K Gomes, Warren Mar, Wonhee Ko, Francisco Guinea, and Hari C Manoharan. Designer Dirac fermions and topological phases in molecular graphene. *Nature*, 483(7389):306, 2012.

[8] Immanuel Bloch, Jean Dalibard, and Sylvain Nascimbene. Quantum simulations with ultracold quantum gases. *Nature Physics*, 8(4):267–276, 2012.

[9] Christian Gross and Immanuel Bloch. Quantum simulations with ultracold atoms in optical lattices. *Science*, 357(6355):995–1001, 2017.

[10] Marco Polini, Francisco Guinea, Maciej Lewenstein, Hari C Manoharan, and Vittorio Pellegrini. Artificial honeycomb lattices for electrons, atoms and photons. *Nature nanotechnology*, 8(9):625–633, 2013.

[11] Immanuel Bloch and Markus Greiner. Exploring quantum matter with ultracold atoms in optical lattices. *Advances in Atomic, Molecular, and Optical Physics*, 52:1–47, 2005.

[12] Alán Aspuru-Guzik and Philip Walther. Photonic quantum simulators. *Nature physics*, 8(4):285–291, 2012.

[13] Ching Hua Lee, Stefan Imhof, Christian Berger, Florian Bayer, Johannes Brehm, Laurens W Molenkamp, Tobias Kiessling, and Ronny Thomale. Topolectrical circuits. *Communications Physics*, 1(1):1–9, 2018.

[14] Yiwen Chu, Prashanta Kharel, William H Renninger, Luke D Burkhart, Luigi Frunzio, Peter T Rakich, and Robert J Schoelkopf. Quantum acoustics with superconducting qubits. *Science*, 358(6360):199–202, 2017.

[15] Thomas Aref, Per Delsing, Maria K Ekström, Anton Frisk Kockum, Martin V Gustafsson, Göran Johansson, Peter J Leek, Einar Magnusson, and Riccardo Manenti. Quantum acoustics with surface acoustic waves. In *Superconducting devices in quantum optics*, pages 217–244. Springer, 2016.

[16] Tim Byrnes, Patrik Recher, Na Young Kim, Shoko Utsunomiya, and Yoshihisa Yamamoto. Quantum simulator for the Hubbard model with long-range Coulomb interactions using surface acoustic waves. *Physical review letters*, 99(1):016405, 2007.

[17] N Nilius, TM Wallis, and W Ho. Development of one-dimensional band structure in artificial gold chains. *Science*, 297(5588):1853–1856, 2002.

[18] Stefan Fölsch, Per Hyldgaard, R Koch, and KH Ploog. Quantum confinement in monatomic Cu chains on Cu (111). *Physical review letters*, 92(5):056803, 2004.

[19] Cyrus F Hirjibehedin, Christopher P Lutz, and Andreas J Heinrich. Spin coupling in engineered atomic structures. *Science*, 312(5776):1021–1024, 2006.

[20] Alexander Ako Khajetoorians, Jens Wiebe, Bruno Chilian, and Roland Wiesendanger. Realizing all-spin–based logic operations atom by atom. *Science*, 332(6033):1062–1064, 2011.

[21] Robert Drost, Teemu Ojanen, Ari Harju, and Peter Liljeroth. Topological states in engineered atomic lattices. *Nature Physics*, 13(7):668–671, 2017.

[22] SR Schofield, P Studer, CF Hirjibehedin, NJ Curson, G Aeppli, and DR Bowler. Quantum engineering at the silicon surface using dangling bonds. *Nature communications*, 4(1):1–7, 2013.

[23] Klaus Von Klitzing. The quantized Hall effect. *Rev. Mod. Phys.*, 58(3):519, 1986.

[24] Horst L Stormer. Nobel lecture: the fractional quantum Hall effect. *Reviews of Modern Physics*, 71(4):875, 1999.

[25] Kamran Behnia. Charged with smuggling heat. *Nature*, 414(6865):696–697, 2001.

[26] Han-Dong Chen, Oskar Vafek, Ali Yazdani, and Shou-Cheng Zhang. Pair density wave in the pseudogap state of high temperature superconductors. *Physical review letters*, 93(18):187002, 2004.

[27] Christopher B Murray, a CR Kagan, and MG Bawendi. Synthesis and characterization of monodisperse nanocrystals and close-packed nanocrystal assemblies. *Annual review of materials science*, 30(1):545–610, 2000.

[28] A Paul Alivisatos. Perspectives on the physical chemistry of semiconductor nanocrystals. *The Journal of Physical Chemistry*, 100(31):13226–13239, 1996.

[29] Louis E Brus. Electronic and optical properties of semiconductor nanocrystals: from molecules to bulk crystals. In *Nanophase Materials*, pages 433–448. Springer, 1994.

[30] Marco Gibertini, Achintya Singha, Vittorio Pellegrini, Marco Polini, Giovanni Vignale, Aron Pinczuk, Loren N Pfeiffer, and Ken W West. Engineering artificial graphene in a two-dimensional electron gas. *Physical Review B*, 79(24):241406, 2009.

[31] Achintya Singha, M Gibertini, B Karmakar, S Yuan, M Polini, Giovanni Vignale, MI Katsnelson, A Pinczuk, LN Pfeiffer, KW West, et al. Two-dimensional Mott-Hubbard electrons in an artificial honeycomb lattice. *Science*, 332(6034):1176–1179, 2011.

[32] Diego Scarabelli, Sheng Wang, Aron Pinczuk, Shalom J Wind, Yuliya Y Kuznetsova, Loren N Pfeiffer, Ken West, Geoff C Gardner, Michael J Manfra, and Vittorio Pellegrini. Fabrication of artificial graphene in a GaAs quantum heterostructure. *Journal of Vacuum Science & Technology B, Nanotechnology and Microelectronics: Materials, Processing, Measurement, and Phenomena*, 33(6):06FG03, 2015.

[33] Lingjie Du, Sheng Wang, Diego Scarabelli, Loren N Pfeiffer, Ken W West, Saeed Fallahi, Geoff C Gardner, Michael J Manfra, Vittorio Pellegrini, Shalom J Wind, et al. Emerging many-body effects in semiconductor artificial graphene with low disorder. *Nature communications*, 9(1):1–6, 2018.

[34] Sheng Wang, Diego Scarabelli, Lingjie Du, Yuliya Y Kuznetsova, Loren N Pfeiffer, Ken W West, Geoff C Gardner, Michael J Manfra, Vittorio Pellegrini,

Shalom J Wind, et al. Observation of Dirac bands in artificial graphene in small-period nanopatterned GaAs quantum wells. *Nature Nanotechnology*, 13(1):29–33, 2018.

[35] Efterpi Kalesaki, WH Evers, Guy Allan, Daniel Vanmaekelbergh, and Christophe Delerue. Electronic structure of atomically coherent square semiconductor superlattices with dimensionality below two. *Physical Review B*, 88(11):115431, 2013.

[36] Efterpi Kalesaki, Christophe Delerue, C Morais Smith, Wouter Beugeling, Guy Allan, and Daniël Vanmaekelbergh. Dirac cones, topological edge states, and nontrivial flat bands in two-dimensional semiconductors with a honeycomb nanogeometry. *Physical review x*, 4(1):011010, 2014.

[37] Wouter Beugeling, Efterpi Kalesaki, Christophe Delerue, Y-M Niquet, Daniel Vanmaekelbergh, and C Morais Smith. Topological states in multi-orbital HgTe honeycomb lattices. *Nature communications*, 6(1):1–7, 2015.

[38] Cenke Xu and Joel E Moore. Stability of the quantum spin Hall effect: Effects of interactions, disorder, and Z 2 topology. *Physical Review B*, 73(4):045322, 2006.

[39] Joel E Moore. The birth of topological insulators. *Nature*, 464(7286):194–198, 2010.

[40] Joel E Moore. Topological insulators. *IEEE Spectrum*, 48(7):38–57, 2011.

[41] Yew San Hor, A Richardella, Pedram Roushan, Yuqi Xia, Joseph G Checkelsky, Ali Yazdani, Md Zahid Hasan, Nai Phuan Ong, and Robert Joseph Cava. p-type Bi2Se3 for topological insulator and low-temperature thermoelectric applications. *Physical Review B*, 79(19):195208, 2009.

[42] Wei Zhang, Rui Yu, Hai-Jun Zhang, Xi Dai, and Zhong Fang. First-principles studies of the three-dimensional strong topological insulators Bi2Te3, Bi2Se3 and Sb2Te3. *New Journal of Physics*, 12(6):065013, 2010.

[43] Peng Cheng, Canli Song, Tong Zhang, Yanyi Zhang, Yilin Wang, Jin-Feng Jia, Jing Wang, Yayu Wang, Bang-Fen Zhu, Xi Chen, et al. Landau quantization of topological surface states in Bi2Se3. *Physical Review Letters*, 105(7):076801, 2010.

[44] Yew San Hor, Anthony J Williams, Joseph G Checkelsky, Pedram Roushan, Jungpil Seo, Qiang Xu, Henny W Zandbergen, Ali Yazdani, Nai Phuan Ong, and Robert Joseph Cava. Superconductivity in CuxBi2Se3 and its implications for pairing in the undoped topological insulator. *Physical review letters*, 104(5):057001, 2010.

[45] Timothy H Hsieh and Liang Fu. Majorana fermions and exotic surface Andreev bound states in topological superconductors: application to CuxBi2Se3. *Physical review letters*, 108(10):107005, 2012.

[46] Oleg V Yazyev, Emmanouil Kioupakis, Joel E Moore, and Steven G Louie. Quasiparticle effects in the bulk and surface-state bands of Bi2Se3 and Bi2Te3 topological insulators. *Physical Review B*, 85(16):161101, 2012.

[47] Tong Zhang, Niv Levy, Jeonghoon Ha, Young Kuk, and Joseph A Stroscio. Scanning tunneling microscopy of gate tunable topological insulator Bi2Se3 thin films. *Physical Review B*, 87(11):115410, 2013.

[48] Xiaoxiong Wang and T-C Chiang. Topological states in Bi2Se3 surfaces created by cleavage within a quintuple layer: Analysis in terms of the Shockley criterion. *Physical Review B*, 89(12):125109, 2014.

[49] H-H Kung, AP Goyal, DL Maslov, Xueyuen Wang, Alexander Lee, AF Kemper, S-W Cheong, and Girsh Blumberg. Observation of chiral surface excitons in a topological insulator Bi2Se3. *Proceedings of the National Academy of Sciences*, 116(10):4006–4011, 2019.

[50] B Andrei Bernevig, Taylor L Hughes, and Shou-Cheng Zhang. Quantum spin Hall effect and topological phase transition in HgTe quantum wells. *Science*, 314(5806):1757–1761, 2006.

[51] C Brüne, CX Liu, EG Novik, EM Hankiewicz, H Buhmann, YL Chen, XL Qi, ZX Shen, SC Zhang, and LW Molenkamp. Quantum Hall effect from the topological surface states of strained bulk HgTe. *Physical Review Letters*, 106(12):126803, 2011.

[52] W Beugeling, CX Liu, EG Novik, LW Molenkamp, and C Morais Smith. Reentrant topological phases in Mn-doped HgTe quantum wells. *Physical Review B*, 85(19):195304, 2012.

[53] Ilya K Drozdov, Aris Alexandradinata, Sangjun Jeon, Stevan Nadj-Perge, Huiwen Ji, RJ Cava, B Andrei Bernevig, and Ali Yazdani. One-dimensional topological edge states of bismuth bilayers. *Nature Physics*, 10(9):664–669, 2014.

[54] Jian Li, Hua Chen, Ilya K Drozdov, Ali Yazdani, B Andrei Bernevig, and AH MacDonald. Topological superconductivity induced by ferromagnetic metal chains. *Physical Review B*, 90(23):235433, 2014.

[55] Barry Bradlyn, L Elcoro, Jennifer Cano, MG Vergniory, Zhijun Wang, C Felser, MI Aroyo, and B Andrei Bernevig. Topological quantum chemistry. *Nature*, 547(7663):298–305, 2017.

[56] Jennifer Cano, Barry Bradlyn, Zhijun Wang, L Elcoro, MG Vergniory, C Felser, MI Aroyo, and B Andrei Bernevig. Building blocks of topological quantum chemistry: Elementary band representations. *Physical Review B*, 97(3):035139, 2018.

[57] B Keimer and JE Moore. The physics of quantum materials. *Nature Physics*, 13(11):1045–1055, 2017.

[58] M Zahid Hasan and Charles L Kane. Colloquium: topological insulators. *Reviews of modern physics*, 82(4):3045, 2010.

[59] M. Zahid Hasan and Joel E. Moore. Three-Dimensional Topological Insulators. *Annual Review of Condensed Matter Physics*, 2(1):55–78, 2011.

[60] David A Siegel, Cheol-Hwan Park, Choongyu Hwang, Jack Deslippe, Alexei V Fedorov, Steven G Louie, and Alessandra Lanzara. Many-body interactions in quasi-freestanding graphene. *Proceedings of the National Academy of Sciences*, 108(28):11365–11369, 2011.

[61] Ganesh R Bhimanapati, Zhong Lin, Vincent Meunier, Yeonwoong Jung, Judy Cha, Saptarshi Das, Di Xiao, Youngwoo Son, Michael S Strano, Valentino R Cooper, et al. Recent advances in two-dimensional materials beyond graphene. *ACS nano*, 9(12):11509–11539, 2015.

[62] Congjun Wu, Doron Bergman, Leon Balents, and S Das Sarma. Flat bands and Wigner crystallization in the honeycomb optical lattice. *Physical review letters*, 99(7):070401, 2007.

[63] Jay D Sau, Sumanta Tewari, Roman M Lutchyn, Tudor D Stanescu, and S Das Sarma. Non-Abelian quantum order in spin-orbit-coupled semiconductors: Search for topological Majorana particles in solid-state systems. *Physical Review B*, 82(21):214509, 2010.

[64] Kai Sun, Zhengcheng Gu, Hosho Katsura, and S Das Sarma. Nearly flatbands with nontrivial topology. *Physical review letters*, 106(23):236803, 2011.

[65] Liang Fu, Charles L Kane, and Eugene J Mele. Topological insulators in three dimensions. *Physical review letters*, 98(10):106803, 2007.

[66] Steve M Young, Sugata Chowdhury, Eric J Walter, Eugene J Mele, Charles L Kane, and Andrew M Rappe. Theoretical investigation of the evolution of the topological phase of Bi2Se3 under mechanical strain. *Physical Review B*, 84(8):085106, 2011.

[67] Jun-Wei Luo and Alex Zunger. Design principles and coupling mechanisms in the 2D quantum well topological insulator HgTe/CdTe. *Physical review letters*, 105(17):176805, 2010.

[68] Kostya S Novoselov, Andre K Geim, Sergei Vladimirovich Morozov, Da Jiang, Michail I Katsnelson, IVa Grigorieva, SVb Dubonos, Firsov, and AA. Two-dimensional gas of massless Dirac fermions in graphene. *nature*, 438(7065):197–200, 2005.

[69] Mark P Boneschanscher, Joost Van Der Lit, Zhixiang Sun, Ingmar Swart, Peter Liljeroth, and Daniël Vanmaekelbergh. Quantitative atomic resolution force imaging on epitaxial graphene with reactive and nonreactive AFM probes. *ACS nano*, 6(11):10216–10221, 2012.

[70] Joost Van Der Lit, Mark P Boneschanscher, Daniël Vanmaekelbergh, Mari Ijäs, Andreas Uppstu, Mikko Ervasti, Ari Harju, Peter Liljeroth, and Ingmar Swart. Suppression of electron–vibron coupling in graphene nanoribbons contacted via a single atom. *Nature communications*, 4(1):1–6, 2013.

[71] Nadine J van der Heijden, Daniel Smith, Gaetano Calogero, Rik S Koster, Daniel Vanmaekelbergh, Marijn A van Huis, and Ingmar Swart. Recognizing nitrogen dopant atoms in graphene using atomic force microscopy. *Physical Review B*, 93(24):245430, 2016.

[72] Sampsa K Hämäläinen, Mark P Boneschanscher, Peter H Jacobse, Ingmar Swart, Katariina Pussi, Wolfgang Moritz, Jouko Lahtinen, Peter Liljeroth, and Jani Sainio. Structure and local variations of the graphene moiré on Ir(111). *Physical Review B*, 88(20):201406, 2013.

[73] Zhixiang Sun, Sampsa K Hämäläinen, Jani Sainio, Jouko Lahtinen, Daniël Vanmaekelbergh, and Peter Liljeroth. Topographic and electronic contrast of the graphene moiré on Ir(111) probed by scanning tunneling microscopy and noncontact atomic force microscopy. *Physical Review B*, 83(8):081415, 2011.

[74] Päivi Järvinen, Sampsa K Hämäläinen, Kaustuv Banerjee, Pasi Häkkinen, Mari Ijäs, Ari Harju, and Peter Liljeroth. Molecular self-assembly on graphene on SiO2 and h-BN substrates. *Nano letters*, 13(7):3199–3204, 2013.

[75] Robert Drost, Andreas Uppstu, Fabian Schulz, Sampsa K Hämäläinen, Mikko Ervasti, Ari Harju, and Peter Liljeroth. Electronic states at the graphene–hexagonal boron nitride zigzag interface. *Nano letters*, 14(9):5128–5132, 2014.

[76] Yuanbo Zhang, Victor W Brar, Feng Wang, Caglar Girit, Yossi Yayon, Melissa Panlasigui, Alex Zettl, and Michael F Crommie. Giant phonon-induced conductance in scanning tunnelling spectroscopy of gate-tunable graphene. *Nature Physics*, 4(8):627–630, 2008.

[77] Yuanbo Zhang, Victor W Brar, Caglar Girit, Alex Zettl, and Michael F Crommie. Origin of spatial charge inhomogeneity in graphene. *Nature Physics*, 5(10):722–726, 2009.

[78] Yang Wang, Victor W Brar, Andrey V Shytov, Qiong Wu, William Regan, Hsin-Zon Tsai, Alex Zettl, Leonid S Levitov, and Michael F Crommie. Mapping Dirac quasiparticles near a single Coulomb impurity on graphene. *Nature Physics*, 8(9):653–657, 2012.

[79] Yang Wang, Dillon Wong, Andrey V Shytov, Victor W Brar, Sangkook Choi, Qiong Wu, Hsin-Zon Tsai, William Regan, Alex Zettl, Roland K Kawakami, et al. Observing atomic collapse resonances in artificial nuclei on graphene. *Science*, 340(6133):734–737, 2013.

[80] Fabian Schulz, Peter H Jacobse, Filippo Federici Canova, Joost Van Der Lit, David Z Gao, Adrianus Van Den Hoogenband, Patrick Han, Robertus JM Klein Gebbink, Marc-Etienne Moret, Pekka M Joensuu, et al. Precursor geometry determines the growth mechanism in graphene nanoribbons. *The Journal of Physical Chemistry C*, 121(5):2896–2904, 2017.

[81] Xiaowei Zhang, Oleg V Yazyev, Juanjuan Feng, Liming Xie, Chenggang Tao, Yen-Chia Chen, Liying Jiao, Zahra Pedramrazi, Alex Zettl, Steven G Louie, et al. Experimentally engineering the edge termination of graphene nanoribbons. *ACS nano*, 7(1):198–202, 2013.

[82] Jinming Cai, Pascal Ruffieux, Rached Jaafar, Marco Bieri, Thomas Braun, Stephan Blankenburg, Matthias Muoth, Ari P Seitsonen, Moussa Saleh, Xinliang Feng, et al. Atomically precise bottom-up fabrication of graphene nanoribbons. *Nature*, 466(7305):470–473, 2010.

[83] Hajo Söde, Leopold Talirz, Oliver Gröning, Carlo Antonio Pignedoli, Reinhard Berger, Xinliang Feng, Klaus Müllen, Roman Fasel, and Pascal Ruffieux. Electronic band dispersion of graphene nanoribbons via Fourier-transformed scanning tunneling spectroscopy. *Physical Review B*, 91(4):045429, 2015.

[84] Pascal Ruffieux, Shiyong Wang, Bo Yang, Carlos Sánchez-Sánchez, Jia Liu, Thomas Dienel, Leopold Talirz, Prashant Shinde, Carlo A Pignedoli, Daniele Passerone, et al. On-surface synthesis of graphene nanoribbons with zigzag edge topology. *Nature*, 531(7595):489–492, 2016.

[85] Shiyong Wang, Leopold Talirz, Carlo A Pignedoli, Xinliang Feng, Klaus Müllen, Roman Fasel, and Pascal Ruffieux. Giant edge state splitting at atomically precise graphene zigzag edges. *Nature communications*, 7(1):1–6, 2016.

[86] Leopold Talirz, Hajo Söde, Tim Dumslaff, Shiyong Wang, Juan Ramon Sanchez-Valencia, Jia Liu, Prashant Shinde, Carlo A Pignedoli, Liangbo Liang, Vincent Meunier, et al. On-surface synthesis and characterization of 9-atom wide armchair graphene nanoribbons. *ACS nano*, 11(2):1380–1388, 2017.

[87] Joost Van der Lit, Peter H Jacobse, Daniel Vanmaekelbergh, and Ingmar Swart. Bending and buckling of narrow armchair graphene nanoribbons via STM manipulation. *New Journal of Physics*, 17(5):053013, 2015.

[88] Mari Ijäs, Mikko Ervasti, A Uppstu, Peter Liljeroth, J Van Der Lit, I Swart, and Ari Harju. Electronic states in finite graphene nanoribbons: Effect of charging and defects. *Physical Review B*, 88(7):075429, 2013.

[89] Chenggang Tao, Liying Jiao, Oleg V Yazyev, Yen-Chia Chen, Juanjuan Feng, Xiaowei Zhang, Rodrigo B Capaz, James M Tour, Alex Zettl, Steven G Louie, et al. Spatially resolving edge states of chiral graphene nanoribbons. *Nature Physics*, 7(8):616–620, 2011.

[90] Yen-Chia Chen, Dimas G De Oteyza, Zahra Pedramrazi, Chen Chen, Felix R Fischer, and Michael F Crommie. Tuning the band gap of graphene nanoribbons synthesized from molecular precursors. *ACS nano*, 7(7):6123–6128, 2013.

[91] Markus König, Steffen Wiedmann, Christoph Brüne, Andreas Roth, Hartmut Buhmann, Laurens W Molenkamp, Xiao-Liang Qi, and Shou-Cheng Zhang. Quantum spin Hall insulator state in HgTe quantum wells. *Science*, 318(5851):766–770, 2007.

[92] Charles L Kane and Eugene J Mele. Quantum spin Hall effect in graphene. *Phys. Rev. Lett.*, 95(22):226801, 2005.

[93] Charles L Kane and Eugene J Mele. Z 2 topological order and the quantum spin Hall effect. *Physical review letters*, 95(14):146802, 2005.

[94] Ryan Babbush, Peter J Love, and Alán Aspuru-Guzik. Adiabatic quantum simulation of quantum chemistry. *Scientific reports*, 4:6603, 2014.

[95] Jingfu Zhang, Man-Hong Yung, Raymond Laflamme, Alán Aspuru-Guzik, and Jonathan Baugh. Digital quantum simulation of the statistical mechanics of a frustrated magnet. *Nature Communications*, 3(1):1–10, 2012.

[96] Jae-yoon Choi, Sebastian Hild, Johannes Zeiher, Peter Schauß, Antonio Rubio-Abadal, Tarik Yefsah, Vedika Khemani, David A Huse, Immanuel Bloch, and Christian Gross. Exploring the many-body localization transition in two dimensions. *Science*, 352(6293):1547–1552, 2016.

[97] Alexander Dauphin, Markus Müller, and Miguel Angel Martin-Delgado. Quantum simulation of a topological Mott insulator with Rydberg atoms in a Lieb lattice. *Physical Review A*, 93(4):043611, 2016.

[98] Dario Bercioux and Sander Otte. Quantum simulation: Solid-state platforms. *Nature Physics*, 13(7):628–629, 2017.

[99] Pierre Barthelemy and Lieven MK Vandersypen. Quantum dot systems: a versatile platform for quantum simulations. *Annalen der Physik*, 525(10-11):808–826, 2013.

[100] Nicholas J Ward, Ivan Kassal, and Alán Aspuru-Guzik. Preparation of many-body states for quantum simulation. *The Journal of chemical physics*, 130(19):194105, 2009.

[101] Roman Schmied, Janus H Wesenberg, and Dietrich Leibfried. Quantum simulation of the hexagonal Kitaev model with trapped ions. *New Journal of Physics*, 13(11):115011, 2011.

[102] Tobias Schaetz, Chris R Monroe, and Tilman Esslinger. Focus on quantum simulation. *New Journal of Physics*, 15(8):085009, 2013.

[103] Ryan Babbush, Dominic W Berry, Ian D Kivlichan, Annie Y Wei, Peter J Love, and Alán Aspuru-Guzik. Exponentially more precise quantum simulation of fermions in second quantization. *New Journal of Physics*, 18(3):033032, 2016.

[104] Toivo Hensgens, Takafumi Fujita, Laurens Janssen, Xiao Li, CJ Van Diepen, Christian Reichl, Werner Wegscheider, S Das Sarma, and Lieven MK Vandersypen. Quantum simulation of a Fermi–Hubbard model using a semiconductor quantum dot array. *Nature*, 548(7665):70–73, 2017.

[105] Peter JJ O'Malley, Ryan Babbush, Ian D Kivlichan, Jonathan Romero, Jarrod R McClean, Rami Barends, Julian Kelly, Pedram Roushan, Andrew Tranter, Nan Ding, et al. Scalable quantum simulation of molecular energies. *Physical Review X*, 6(3):031007, 2016.

[106] Richard P Feynman. Simulating physics with computers. *Int. J. Theor. Phys*, 21(6/7), 1982.

[107] Richard P Feynman. Quantum mechanical computers. *Foundations of physics*, 16(6):507–531, 1986.

[108] Jing-Min Hou and Wen-Xing Yang. Next-nearest-neighbor-tunneling-induced symmetry breaking of Hofstadter's butterfly spectrum for ultracold atoms on the honeycomb lattice. *Physics Letters A*, 373(31):2774–2777, 2009.

[109] Wei-Feng Tsai, Chen Fang, Hong Yao, and Jiangping Hu. Interaction-driven topological and nematic phases on the Lieb lattice. *New Journal of Physics*, 17(5):055016, 2015.

[110] Eduardo V Castro, Adolfo G Grushin, Belén Valenzuela, María AH Vozmediano, Alberto Cortijo, and Fernando de Juan. Topological fermi liquids from coulomb interactions in the doped honeycomb lattice. *Physical review letters*, 107(10):106402, 2011.

[111] Jun Wen, Andreas Rüegg, C-C Joseph Wang, and Gregory A Fiete. Interaction-driven topological insulators on the kagome and the decorated honeycomb lattices. *Physical Review B*, 82(7):075125, 2010.

[112] Stephan Rachel and Karyn Le Hur. Topological insulators and Mott physics from the Hubbard interaction. *Physical Review B*, 82(7):075106, 2010.

[113] Stephan Rachel. Interacting topological insulators: a review. *Reports on Progress in Physics*, 81(11):116501, 2018.

[114] Conan Weeks, Jun Hu, Jason Alicea, Marcel Franz, and Ruqian Wu. Engineering a robust quantum spin Hall state in graphene via adatom deposition. *Physical Review X*, 1(2):021001, 2011.

[115] Immanuel Bloch. Quantum gases in optical lattices. *Physics World*, 17(4):25, 2004.

[116] Immanuel Bloch. Ultracold quantum gases in optical lattices. *Nature physics*, 1(1):23–30, 2005.

[117] Fabian Grusdt, Tracy Li, Immanuel Bloch, and Eugene Demler. Tunable spin-orbit coupling for ultracold atoms in two-dimensional optical lattices. *Physical Review A*, 95(6):063617, 2017.

[118] Nathan Goldman, DF Urban, and D Bercioux. Topological phases for fermionic cold atoms on the Lieb lattice. *Physical Review A*, 83(6):063601, 2011.

[119] Immanuel Bloch and Achim Rosch. Exploring strongly correlated quantum many-body systems with ultracold atoms in optical lattices. *physica status solidi (b)*, 247(3):530–536, 2010.

[120] Peter Barmettler, Ana Maria Rey, Eugene Demler, Mikhail D Lukin, Immanuel Bloch, and Vladimir Gritsev. Quantum many-body dynamics of coupled double-well superlattices. *Physical Review A*, 78(1):012330, 2008.

[121] Immanuel Bloch, Jean Dalibard, and Wilhelm Zwerger. Many-body physics with ultracold gases. *Reviews of modern physics*, 80(3):885, 2008.

[122] Torsten Karzig, Charles-Edouard Bardyn, Netanel H Lindner, and Gil Refael. Topological polaritons. *Physical Review X*, 5(3):031001, 2015.

[123] AV Nalitov, DD Solnyshkov, and G Malpuech. Polariton Z topological insulator. *Physical review letters*, 114(11):116401, 2015.

[124] Florent Baboux, Eli Levy, Aristide Lemaître, Carmen Gómez, Elisabeth Galopin, Luc Le Gratiet, Isabelle Sagnes, Alberto Amo, Jacqueline Bloch, and Eric Akkermans. Measuring topological invariants from generalized edge states in polaritonic quasicrystals. *Physical Review B*, 95(16):161114, 2017.

[125] Zimeng Chi, Xiaoyong Guo, and Zaijun Wang. Topological phase transition of two-dimensional topological polaritons. *International Journal of Modern Physics B*, 31(11):1750070, 2017.

[126] Dmitry R Gulevich, Dmitry Yudin, Dmitry V Skryabin, Ivan V Iorsh, and Ivan A Shelykh. Exploring nonlinear topological states of matter with exciton-polaritons: Edge solitons in kagome lattice. *Scientific reports*, 7(1):1–8, 2017.

[127] S Klembt, TH Harder, OA Egorov, K Winkler, R Ge, MA Bandres, M Emmerling, L Worschech, TCH Liew, M Segev, et al. Exciton-polariton topological insulator. *Nature*, 562(7728):552–556, 2018.

[128] Chunyan Li, Fangwei Ye, Xianfeng Chen, Yaroslav V Kartashov, Albert Ferrando, Lluis Torner, and Dmitry V Skryabin. Lieb polariton topological insulators. *Physical Review B*, 97(8):081103, 2018.

[129] DD Solnyshkov, Olivier Bleu, and Guillaume Malpuech. Topological optical isolator based on polariton graphene. *Applied Physics Letters*, 112(3):031106, 2018.

[130] Holger Suchomel, Sebastian Klembt, Tristan H Harder, Martin Klaas, Oleg A Egorov, Karol Winkler, Monika Emmerling, Ronny Thomale, Sven Höfling, and Christian Schneider. Platform for electrically pumped polariton simulators and topological lasers. *Physical Review Letters*, 121(25):257402, 2018.

[131] Chuanyi Zhang, Yuanxu Wang, and Weifeng Zhang. Topological phase transition with p orbitals in the exciton-polariton honeycomb lattice. *Journal of Physics: Condensed Matter*, 31(33):335403, 2019.

[132] Daniele Bajoni, Dario Gerace, Matteo Galli, Jacqueline Bloch, Remy Braive, Isabelle Sagnes, Audrey Miard, Aristide Lemaître, Maddalena Patrini, and Lucio Claudio Andreani. Exciton polaritons in two-dimensional photonic crystals. *Physical Review B*, 80(20):201308, 2009.

[133] Marta Galbiati, Lydie Ferrier, Dmitry D Solnyshkov, Dimitrii Tanese, Esther Wertz, Alberto Amo, Marco Abbarchi, Pascale Senellart, Isabelle Sagnes, Aristide Lemaître, et al. Polariton condensation in photonic molecules. *Physical review letters*, 108(12):126403, 2012.

[134] Dimitrii Tanese, Evgeni Gurevich, Florent Baboux, Thibaut Jacqmin, Aristide Lemaître, Elisabeth Galopin, Isabelle Sagnes, Alberto Amo, Jacqueline Bloch, and Eric Akkermans. Fractal energy spectrum of a polariton gas in a Fibonacci quasiperiodic potential. *Physical review letters*, 112(14):146404, 2014.

[135] Alberto Amo and Jacqueline Bloch. Exciton-polaritons in lattices: A non-linear photonic simulator. *Comptes Rendus Physique*, 17(8):934–945, 2016.

[136] Yaakov Lumer, Yonatan Plotnik, Mikael C Rechtsman, and Mordechai Segev. Self-localized states in photonic topological insulators. *Physical review letters*, 111(24):243905, 2013.

[137] JM Zeuner, Y Plotnik, Mikael C Rechtsman, Y Lumer, M Segev, and A Szameit. Experimental demonstration of photonic Floquet topological insulators. In *The European Conference on Lasers and Electro-Optics*, page CK_3_1. Optical Society of America, 2013.

[138] Mikael C Rechtsman, Yonatan Plotnik, Julia M Zeuner, Daohong Song, Zhigang Chen, Alexander Szameit, and Mordechai Segev. Topological creation and destruction of edge states in photonic graphene. *Physical review letters*, 111(10):103901, 2013.

[139] Miguel A Bandres, Mikael C Rechtsman, Alexander Szameit, and Mordechai Segev. Lieb photonic topological insulator. In *2014 Conference on Lasers and Electro-Optics (CLEO)-Laser Science to Photonic Applications*, pages 1–2. IEEE, 2014.

[140] D Guzmán-Silva, Cristian Mejía-Cortés, MA Bandres, MC Rechtsman, S Weimann, S Nolte, M Segev, A Szameit, and RA Vicencio. Experimental observation of bulk and edge transport in photonic Lieb lattices. *New Journal of Physics*, 16(6):063061, 2014.

[141] Yonatan Plotnik, Mikael C Rechtsman, Daohong Song, Matthias Heinrich, Julia M Zeuner, Stefan Nolte, Yaakov Lumer, Natalia Malkova, Jingjun Xu, Alexander Szameit, et al. Observation of unconventional edge states in 'photonic graphene'. *Nature materials*, 13(1):57–62, 2014.

[142] Hanan Herzig Sheinfux, Ido Kaminer, Yonatan Plotnik, Guy Bartal, and Mordechai Segev. Subwavelength multilayer dielectrics: Ultrasensitive transmission and breakdown of effective-medium. In *2014 Conference on Lasers and Electro-Optics (CLEO)-Laser Science to Photonic Applications*, pages 1–2. IEEE, 2014.

[143] Thibaut Jacqmin, Iacopo Carusotto, Isabelle Sagnes, Marco Abbarchi, DD Solnyshkov, Guillaume Malpuech, Elisabeth Galopin, Aristide Lemaître, Jacqueline Bloch, and Alberto Amo. Direct observation of Dirac cones and a flatband in a honeycomb lattice for polaritons. *Physical review letters*, 112(11):116402, 2014.

[144] M Milićević, T Ozawa, P Andreakou, I Carusotto, T Jacqmin, E Galopin, A Lemaitre, L Le Gratiet, I Sagnes, J Bloch, et al. Edge states in polariton honeycomb lattices. *2D Materials*, 2(3):034012, 2015.

[145] Miguel A Bandres, Mikael C Rechtsman, and Mordechai Segev. Topological transport in photonic quasicrystals. In *2015 Conference on Lasers and Electro-Optics (CLEO)*, pages 1–2. IEEE, 2015.

[146] Y Plotnik, MA Bandres, S Stützer, Y Lumer, MC Rechtsman, A Szameit, and M Segev. Analogue of Rashba pseudo-spin-orbit coupling in photonic lattices by gauge field engineering. *Physical Review B*, 94(2):020301, 2016.

[147] Guillermo Muñoz-Matutano, Andrew Wood, Mattias Johnsson, Xavier Vidal, Ben Q Baragiola, Andreas Reinhard, Aristide Lemaître, Jacqueline Bloch, Alberto Amo, Gilles Nogues, et al. Emergence of quantum correlations from interacting fibre-cavity polaritons. *Nature materials*, 18(3):213–218, 2019.

[148] Miguel A Bandres, Mikael C Rechtsman, and Mordechai Segev. Topological transport in photonic quasicrystals. In *2015 Conference on Lasers and Electro-Optics (CLEO)*, pages 1–2. IEEE, 2015.

[149] Mikael C Rechtsman, Yaakov Lumer, Yonatan Plotnik, Armando Perez-Leija, Alexander Szameit, and Mordechai Segev. Topological protection of photonic path entanglement. *Optica*, 3(9):925–930, 2016.

[150] Ronald Hanson, Leo P Kouwenhoven, Jason R Petta, Seigo Tarucha, and Lieven MK Vandersypen. Spins in few-electron quantum dots. *Reviews of modern physics*, 79(4):1217, 2007.

[151] Xing Lan Liu, Dorothee Hug, and Lieven MK Vandersypen. Gate-defined graphene double quantum dot and excited state spectroscopy. *Nano letters*, 10(5):1623–1627, 2010.

[152] MS Rudner, LMK Vandersypen, V Vuletić, and LS Levitov. Generating entanglement and squeezed states of nuclear spins in quantum dots. *Physical review letters*, 107(20):206806, 2011.

[153] Martin JA Schuetz, Benoit Vermersch, Gerhard Kirchmair, Lieven MK Vandersypen, J Ignacio Cirac, Mikhail D Lukin, and Peter Zoller. Quantum simulation and optimization in hot quantum networks. *Physical Review B*, 99(24):241302, 2019.

[154] Gerd Binnig, Heinrich Rohrer, Ch Gerber, and Edmund Weibel. Surface studies by scanning tunneling microscopy. *Physical review letters*, 49(1):57, 1982.

[155] Gerd Binnig and Heinrich Rohrer. Scanning tunneling microscopy—from birth to adolescence. *reviews of modern physics*, 59(3):615, 1987.

[156] Mark A Reed, John N Randall, James H Luscombe, William R Frensley, Raj J Aggarwal, Richard J Matyi, Tom M Moore, and Anna E Wetsel. Quantum dot resonant tunneling spectroscopy. In *Festkörperprobleme 29*, pages 267–283. Springer, 1989.

[157] LC Davis, MP Everson, RC Jaklevic, and Weidian Shen. Theory of the local density of surface states on a metal: Comparison with scanning tunneling spectroscopy of a Au(111) surface. *Physical Review B*, 43(5):3821, 1991.

[158] RC Ashoori, JA Lebens, NP Bigelow, and RH Silsbee. Energy gaps of the two-dimensional electron gas explored with equilibrium tunneling spectroscopy. *Physical Review B*, 48(7):4616, 1993.

[159] Danny Porath, Yair Levi, Moeen Tarabiah, and Oded Millo. Tunneling spectroscopy of isolated C 60 molecules in the presence of charging effects. *Physical Review B*, 56(15):9829, 1997.

[160] B Legrand, B Grandidier, JP Nys, D Stiévenard, JM Gérard, and V Thierry-Mieg. Scanning tunneling microscopy and scanning tunneling spectroscopy of self-assembled InAs quantum dots. *Applied physics letters*, 73(1):96–98, 1998.

[161] Jörg Kliewer and Richard Berndt. Scanning tunneling spectroscopy of Na on Cu(111). *Physical Review B*, 65(3):035412, 2001.

[162] Z Klusek, P Dabrowski, P Kowalczyk, W Kozlowski, W Olejniczak, P Blake, M Szybowicz, and T Runka. Graphene on gold: electron density of states studies by scanning tunneling spectroscopy. *Applied Physics Letters*, 95(11):113114, 2009.

[163] Ingmar Swart, Peter Liljeroth, and Daniel Vanmaekelbergh. Scanning probe microscopy and spectroscopy of colloidal semiconductor nanocrystals and assembled structures. *Chemical reviews*, 116(18):11181–11219, 2016.

[164] Peter Liljeroth, Jascha Repp, and Gerhard Meyer. Current-induced hydrogen tautomerization and conductance switching of naphthalocyanine molecules. *Science*, 317(5842):1203–1206, 2007.

[165] Leo Gross, Fabian Mohn, Peter Liljeroth, Jascha Repp, Franz J Giessibl, and Gerhard Meyer. Measuring the charge state of an adatom with noncontact atomic force microscopy. *Science*, 324(5933):1428–1431, 2009.

[166] Niko Pavliček, Ingmar Swart, Judith Niedenführ, Gerhard Meyer, and Jascha Repp. Symmetry dependence of vibration-assisted tunneling. *Physical review letters*, 110(13):136101, 2013.

[167] Christof Uhlmann, Ingmar Swart, and Jascha Repp. Controlling the orbital sequence in individual Cu-phthalocyanine molecules. *Nano letters*, 13(2):777–780, 2013.

[168] EPAM Bakkers, Zeger Hens, A Zunger, A Franceschetti, LP Kouwenhoven, L Gurevich, and D Vanmaekelbergh. Shell-tunneling spectroscopy of the single-particle energy levels of insulating quantum dots. *Nano Letters*, 1(10):551–556, 2001.

[169] William Shockley. On the surface states associated with a periodic potential. *Physical review*, 56(4):317, 1939.

[170] Ig Tamm. Über eine mögliche Art der Elektronenbindung an Kristalloberflächen. *Zeitschrift für Physik*, 76(11-12):849–850, 1932.

[171] Ig Tamm and D Blochinzev. Über die austrittsarbeit der elektronen aus metallen. *Zeitschrift für Physik*, 77(11-12):774–777, 1932.

[172] ET Goodwin. Electronic states at the surfaces of crystals: I. The approximation of nearly free electrons. In *Mathematical Proceedings of the Cambridge Philosophical Society*, volume 35, pages 205–220. Cambridge University Press, 1939.

[173] ET Goodwin. Electronic states at the surfaces of crystals: II. The approximation of tight binding: Finite linear chain of atoms. In *Mathematical Proceedings of the Cambridge Philosophical Society*, volume 35, pages 221–231. Cambridge University Press, 1939.

[174] ET Goodwin. Electronic states at the surfaces of crystals: IV. The activation of adsorbed atoms by surface electrons. In *Mathematical Proceedings of the Cambridge Philosophical Society*, volume 35, pages 474–484. Cambridge University Press, 1939.

[175] A Akin Ünal, Christian Tusche, Safia Ouazi, Sebastian Wedekind, Cheng-Tien Chiang, Aimo Winkelmann, Dirk Sander, Jürgen Henk, and Jürgen Kirschner. Hybridization between the unoccupied Shockley surface state and bulk electronic states on Cu(111). *Physical Review B*, 84(7):073107, 2011.

[176] F Baumberger, T Greber, and J Osterwalder. Fermi surfaces of the two-dimensional surface states on vicinal Cu(111). *Physical Review B*, 64(19):195411, 2001.

[177] R Courths, M Lau, T Scheunemann, H Gollisch, and R Feder. From the Shockley surface state on Cu(111) to sp-like surface resonances on Cu 3 Au(111). *Physical Review B*, 63(19):195110, 2001.

[178] SD Kevan. Evidence for a new broadening mechanism in angle-resolved photoemission from Cu(111). *Physical review letters*, 50(7):526, 1983.

[179] MP Everson, LC Davis, RC Jaklevic, and Weidian Shen. Effects of surface features upon the Au(111) surface state local density of states studied with scanning tunneling spectroscopy. *Journal of Vacuum Science & Technology B: Microelectronics and Nanometer Structures Processing, Measurement, and Phenomena*, 9(2):891–896, 1991.

[180] I Barke and H Hövel. Confined Shockley surface states on the (111) facets of gold clusters. *Physical review letters*, 90(16):166801, 2003.

[181] JM Nicholls, F Salvan, and B Reihl. Surface states of ordered Au, Ag, and Cu overlayers on Si(111) studied by inverse photoemission. *Physical Review B*, 34(4):2945, 1986.

[182] MP Everson, LC Davis, RC Jaklevic, and Weidian Shen. Effects of surface features upon the Au(111) surface state local density of states studied with scanning tunneling spectroscopy. *Journal of Vacuum Science & Technology B: Microelectronics and Nanometer Structures Processing, Measurement, and Phenomena*, 9(2):891–896, 1991.

[183] Thomas Andreev, Ingo Barke, and Heinz Hövel. Adsorbed rare-gas layers on Au(111): Shift of the Shockley surface state studied with ultraviolet photoelectron spectroscopy and scanning tunneling spectroscopy. *Physical Review B*, 70(20):205426, 2004.

[184] J Henk, M Hoesch, J Osterwalder, A Ernst, and P Bruno. Spin–orbit coupling in the L-gap surface states of Au(111): spin-resolved photoemission experiments and first-principles calculations. *Journal of Physics: Condensed Matter*, 16(43):7581, 2004.

[185] Moritz Hoesch, M Muntwiler, VN Petrov, M Hengsberger, L Patthey, M Shi, M Falub, T Greber, and J Osterwalder. Spin structure of the Shockley surface state on Au(111). *Physical Review B*, 69(24):241401, 2004.

[186] J Kröger, L Limot, H Jensen, R Berndt, and P Johansson. Stark effect in Au(111) and Cu(111) surface states. *Physical review B*, 70(3):033401, 2004.

[187] Matthias Muntwiler, Moritz Hoesch, Vladimir N Petrov, Matthias Hengsberger, Luc Patthey, Ming Shi, Mihaela Falub, Thomas Greber, and Jürg Osterwalder. Spin-and angle-resolved photoemission spectroscopy study of the Au(111) Shockley surface state. *Journal of electron spectroscopy and related phenomena*, 137:119–123, 2004.

[188] C Didiot, Y Fagot-Revurat, S Pons, B Kierren, and D Malterre. ARPES and STS investigation of noble metal Shockley states: Confinement in vicinal Au(1 1 1) surfaces and self-organized nanostructures. *Surface science*, 601(18):4029–4035, 2007.

[189] Paweł Janusz Kowalczyk, M Puchalski, Witold Kozłowski, P Dąbrowski, Z Klusek, and W Olejniczak. Investigation of the Shockley surface state on clean and air-exposed Au(111). *Applied surface science*, 254(15):4572–4576, 2008.

[190] Swantje Heers, Phivos Mavropoulos, Samir Lounis, Rudolf Zeller, and Stefan Blügel. Lifetime reduction of surface states at Cu, Ag, and Au (111) caused by impurity scattering. *Physical Review B*, 86(12):125444, 2012.

[191] Beomyoung Kim, Choong H Kim, Panjin Kim, Wonsig Jung, Yeongkwan Kim, Yoonyoung Koh, Masashi Arita, Kenya Shimada, Hirofumi Namatame, Masaki Taniguchi, et al. Spin and orbital angular momentum structure of Cu (111) and Au (111) surface states. *Physical Review B*, 85(19):195402, 2012.

[192] S Caravati, G Butti, GP Brivio, MI Trioni, S Pagliara, G Ferrini, G Galimberti, E Pedersoli, C Giannetti, and F Parmigiani. Cu(111) and Cu(001) surface electronic states. Comparison between theory and experiment. *Surface science*, 600(18):3901–3905, 2006.

[193] EJ Heller, MF Crommie, CP Lutz, and DM Eigler. Scattering and absorption of surface electron waves in quantum corrals. *Nature*, 369(6480):464–466, 1994.

[194] P. O. Gartland and B. J. Slagsvold. Transitions conserving parallel momentum in photoemission from the (111) face of copper. *Phys. Rev. B*, 12:4047–4058, Nov 1975.

[195] L. Bürgi, L Petersen, H Brune, and K Kern. Noble metal surface states: Deviations from parabolic dispersion. *Surface Science*, 447(1):L157 – L161, 2000.

[196] Fredrik E Olsson, Mats Persson, AG Borisov, J-P Gauyacq, J Lagoute, and S Fölsch. Localization of the Cu(111) surface state by single Cu adatoms. *Physical review letters*, 93(20):206803, 2004.

[197] Jérôme Lagoute, Xi Liu, and Stefan Fölsch. Link between adatom resonances and the Cu(111) Shockley surface state. *Physical review letters*, 95(13):136801, 2005.

[198] Jérôme Lagoute, Xi Liu, and Stefan Fölsch. Electronic properties of straight, kinked, and branched Cu/ Cu(111) quantum wires: A low-temperature scanning tunneling microscopy and spectroscopy study. *Physical Review B*, 74(12):125410, 2006.

[199] Lars Diekhöner, MA Schneider, AN Baranov, VS Stepanyuk, P Bruno, and K Kern. Surface states of cobalt nanoislands on Cu(111). *Physical review letters*, 90(23):236801, 2003.

[200] María Andrea Barral, Mariana Weissmann, and Ana María Llois. Characterization of the surface states of Co(0001), Co(111), and ultrathin films of Co on Cu(111). *Physical Review B*, 72(12):125433, 2005.

[201] Shen Shu Sung and Roald Hoffmann. How carbon monoxide bonds to metal surfaces. *Journal of the American Chemical Society*, 107(3):578–584, 1985.

[202] Xin-Xin ZHAO and Yi-Ming MI. First-Principle Calculations on the Atomic Geometry and Electronic States of CO Monolayer on Cu(001) Surface. *Acta Physico-Chimica Sinica*, 24(1):127–132, 2008.

[203] L Bartels, G Meyer, and K-H Rieder. Controlled vertical manipulation of single CO molecules with the scanning tunneling microscope: A route to chemical contrast. *Applied Physics Letters*, 71(2):213–215, 1997.

[204] John Weiner, Louw Feenstra, and Jörg Schmiedmayer. Conference on atoms and molecules near surfaces (CAMS). In *Journal of Physics: Conference Series*, volume 19, page 23, 2005.

[205] L Bartels, G Meyer, and K-H Rieder. Lateral manipulation of single Cu atoms on flat and stepped copper surfaces. *Journal of Vacuum Science & Technology A: Vacuum, Surfaces, and Films*, 16(3):1047–1049, 1998.

[206] Joseph A Stroscio and DM Eigler. Atomic and molecular manipulation with the scanning tunneling microscope. *Science*, 254(5036):1319–1326, 1991.

[207] Gerhard Meyer, Ludwig Bartels, Sven Zöphel, Erdmuth Henze, and Karl-Heinz Rieder. Controlled atom by atom restructuring of a metal surface with the scanning tunneling microscope. *Physical review letters*, 78(8):1512, 1997.

[208] L Bartels, G Meyer, and K-H Rieder. Basic steps of lateral manipulation of single atoms and diatomic clusters with a scanning tunneling microscope tip. *Physical Review Letters*, 79(4):697, 1997.

[209] L Bartels, G Meyer, and K-H Rieder. Basic steps involved in the lateral manipulation of single CO molecules and rows of CO molecules. *Chemical physics letters*, 273(5-6):371–375, 1997.

[210] L Bartels, G Meyer, and K-H Rieder. Atomic hop-scotch: different manipulation modes of single Cu atoms on Cu(111). *Chemical physics letters*, 285(3-4):284–287, 1998.

[211] Gerd Binnig and Heinrich Rohrer. In touch with atoms. In *More Things in Heaven and Earth*, pages 543–554. Springer, 1999.

[212] Alexander A Khajetoorians, Daniel Wegner, Alexander F Otte, and Ingmar Swart. Creating designer quantum states of matter atom-by-atom. *Nature Reviews Physics*, 1(12):703–715, 2019.

[213] Niklas Nilius, Thomas M Wallis, and Wilson Ho. Tailoring electronic properties of atomic chains assembled by STM. *Applied Physics A*, 80(5):951–956, 2005.

[214] Niklas Nilius, Thomas M Wallis, and Wilson Ho. Building alloys from single atoms: Au- Pd Chains on NiAl(110). *The Journal of Physical Chemistry B*, 108(38):14616–14619, 2004.

[215] Alexander Sperl, Joerg Kröger, Nicolas Néel, Henning Jensen, Richard Berndt, Andreas Franke, and Eckhard Pehlke. Unoccupied states of individual silver clusters and chains on Ag(111). *Physical Review B*, 77(8):085422, 2008.

[216] Kiyoshi Kanisawa, Stefan Fölsch, et al. Quantum Rings Engineered by Atom Manipulation. *Physical review letters*, 123(6):066801, 2019.

[217] Stefan Fölsch, Jianshu Yang, Christophe Nacci, and Kiyoshi Kanisawa. Atom-by-atom quantum state control in adatom chains on a semiconductor. *Physical review letters*, 103(9):096104, 2009.

[218] T Matsui, Chr Meyer, L Sacharow, J Wiebe, and R Wiesendanger. Electronic states of Fe atoms and chains on InAs(110) from scanning tunneling spectroscopy. *Physical Review B*, 75(16):165405, 2007.

[219] Howon Kim, Alexandra Palacio-Morales, Thore Posske, Levente Rózsa, Krisztián Palotás, László Szunyogh, Michael Thorwart, and Roland Wiesendanger. Toward tailoring Majorana bound states in artificially constructed magnetic atom chains on elemental superconductors. *Sci. Adv.*, 4(5):eaar5251, 2018.

[220] Rémy Pawlak, Silas Hoffman, Jelena Klinovaja, Daniel Loss, and Ernst Meyer. Majorana fermions in magnetic chains. *Progress in Particle and Nuclear Physics*, 107:1–19, 2019.

[221] Rémy Pawlak, Marcin Kisiel, Jelena Klinovaja, Tobias Meier, Shigeki Kawai, Thilo Glatzel, Daniel Loss, and Ernst Meyer. Probing atomic structure and Majorana wavefunctions in mono-atomic Fe chains on superconducting Pb surface. *npj Quantum Information*, 2(1):1–5, 2016.

[222] Stevan Nadj-Perge, Ilya K Drozdov, Jian Li, Hua Chen, Sangjun Jeon, Jungpil Seo, Allan H MacDonald, B Andrei Bernevig, and Ali Yazdani. Observation of Majorana fermions in ferromagnetic atomic chains on a superconductor. *Science*, 346(6209):602–607, 2014.

[223] Avijit Kumar, Kaustuv Banerjee, and Peter Liljeroth. Molecular assembly on two-dimensional materials. *Nanotechnology*, 28(8):082001, 2017.

[224] FE Kalff, Marnix P Rebergen, E Fahrenfort, Jan Girovsky, Ranko Toskovic, Jose L Lado, Joaquín Fernández-Rossier, and Alexander F Otte. A kilobyte rewritable atomic memory. *Nature nanotechnology*, 11(11):926–929, 2016.

[225] Jan Girovsky, Jose L. Lado, Floris E. Kalff, Eleonora Fahrenfort, Lucas J. J. M. Peters, Joaquín Fernández-Rossier, and Alexander F. Otte. Emergence of quasiparticle Bloch states in artificial crystals crafted atom-by-atom. *SciPost Phys.*, 2:020, 2017.

[226] Jan Girovsky, Jose L. Lado, Floris E. Kalff, Eleonora Fahrenfort, Lucas J. J. M. Peters, Joaquín Fernández-Rossier, and Alexander F. Otte. Emergence of quasiparticle Bloch states in artificial crystals crafted atom-by-atom. *SciPost Phys.*, 2:020, 2017.

[227] Md Nurul Huda, Shawulienu Kezilebieke, and Peter Liljeroth. Designer flat bands in one-dimensional artificial systems. *arXiv preprint arXiv:2003.08234*, 2020.

[228] Richard Wallace Robinett. Energy eigenvalues and periodic orbits for the circular disk or annular infinite well. *Surface Review and Letters*, 5(02):519–526, 1998.

[229] Richard Wallace Robinett. Visualizing the solutions for the circular infinite well in quantum and classical mechanics. *American Journal of Physics*, 64(4):440–446, 1996.

[230] Marlou R Slot, Thomas S Gardenier, Peter H Jacobse, Guido CP van Miert, Sander N Kempkes, Stephan JM Zevenhuizen, Cristiane Morais Smith, Daniel Vanmaekelbergh, and Ingmar Swart. Experimental realization and characterization of an electronic Lieb lattice. *Nat. Phys.*, 13(7):672, 2017.

[231] R.W. Robinett. *Quantum Mechanics: Classical Results, Modern Systems, and Visualized Examples*. Oxford University Press, 2006.

[232] D.W. Ball. *Physical Chemistry*. Cengage Learning, 2014.

[233] Jörg Kliewer, Richard Berndt, and S Crampin. Scanning tunnelling spectroscopy of electron resonators. *New Journal of Physics*, 3(1):22, 2001.

[234] Borman S.T.P. Harteveld J.W. Freeney, S.E and I. Swart. Coupling quantum corrals to form artificial molecules. *SciPost Phys.*, 10, 2020.

[235] AH Castro Neto, Francisco Guinea, Nuno MR Peres, Kostya S Novoselov, and Andre K Geim. The electronic properties of graphene. *Reviews of modern physics*, 81(1):109, 2009.

[236] Congjun Wu and S Das Sarma. p x, y-orbital counterpart of graphene: Cold atoms in the honeycomb optical lattice. *Physical Review B*, 77(23):235107, 2008.

[237] B Wunsch, F Guinea, and F Sols. Dirac-point engineering and topological phase transitions in honeycomb optical lattices. *New Journal of Physics*, 10(10):103027, 2008.

[238] Torben Müller, Simon Fölling, Artur Widera, and Immanuel Bloch. State preparation and dynamics of ultracold atoms in higher lattice orbitals. *Physical review letters*, 99(20):200405, 2007.

[239] Marijana Milićević, Tomoki Ozawa, Gilles Montambaux, Iacopo Carusotto, Elisabeth Galopin, Aristide Lemaître, L Le Gratiet, Isabelle Sagnes, Jacqueline Bloch, and Alberto Amo. Orbital edge states in a photonic honeycomb lattice. *Physical Review Letters*, 118(10):107403, 2017.

[240] Boubekeur Lalmi, Hamid Oughaddou, Hanna Enriquez, Abdelkader Kara, Sébastien Vizzini, Bénidicte Ealet, and Bernard Aufray. Epitaxial growth of a silicene sheet. *Applied Physics Letters*, 97(22):223109, 2010.

[241] Michel Houssa, Emilio Scalise, Kiroubanand Sankaran, Geoffrey Pourtois, VV Afanas' Ev, and Andre Stesmans. Electronic properties of hydrogenated silicene and germanene. *Applied Physics Letters*, 98(22):223107, 2011.

[242] Cheng-Cheng Liu, Wanxiang Feng, and Yugui Yao. Quantum spin Hall effect in silicene and two-dimensional germanium. *Physical review letters*, 107(7):076802, 2011.

[243] Patrick Vogt, Paola De Padova, Claudio Quaresima, Jose Avila, Emmanouil Frantzeskakis, Maria Carmen Asensio, Andrea Resta, Bénédicte Ealet, and Guy Le Lay. Silicene: compelling experimental evidence for graphenelike two-dimensional silicon. *Physical review letters*, 108(15):155501, 2012.

[244] L Matthes, O Pulci, and F Bechstedt. Optical properties of two-dimensional honeycomb crystals graphene, silicene, germanene, and tinene from first principles. *New Journal of Physics*, 16(10):105007, 2014.

[245] LC Lew Yan Voon, Jiajie Zhu, and Udo Schwingenschlögl. Silicene: Recent theoretical advances. *Applied Physics Reviews*, 3(4):040802, 2016.

[246] Adil Acun, Lijie Zhang, Pantelis Bampoulis, M Farmanbar, Arie van Houselt, AN Rudenko, M Lingenfelder, G Brocks, Bene Poelsema, MI Katsnelson, et al. Germanene: the germanium analogue of graphene. *Journal of physics: Condensed matter*, 27(44):443002, 2015.

[247] Lijie Zhang, Pantelis Bampoulis, Arie van Houselt, and Henricus JW Zandvliet. Two-dimensional Dirac signature of germanene. *Applied physics letters*, 107(11):111605, 2015.

[248] LC Post, T Xu, NA Franchina Vergel, A Tadjine, Y Lambert, F Vaurette, D Yarekha, L Desplanque, D Stiévenard, X Wallart, et al. Triangular nanoperforation and band engineering of InGaAs quantum wells: a lithographic route toward Dirac cones in III–V semiconductors. *Nanotechnology*, 30(15):155301, 2019.

[249] Cheol-Hwan Park and Steven G Louie. Making massless Dirac fermions from a patterned two-dimensional electron gas. *Nano letters*, 9(5):1793–1797, 2009.

[250] L Nadvornik, M Orlita, NA Goncharuk, L Smrčka, V Novák, V Jurka, K Hruška, Z Výborný, ZR Wasilewski, M Potemski, et al. From laterally modulated two-dimensional electron gas towards artificial graphene. *New Journal of Physics*, 14(5):053002, 2012.

[251] G De Simoni, Achintya Singha, M Gibertini, B Karmakar, M Polini, V Piazza, LN Pfeiffer, KW West, F Beltram, and V Pellegrini. Delocalized-localized transition in a semiconductor two-dimensional honeycomb lattice. *Applied Physics Letters*, 97(13):132113, 2010.

[252] Sheng Wang, Diego Scarabelli, Yuliya Y Kuznetsova, Shalom J Wind, Aron Pinczuk, Vittorio Pellegrini, Michael J Manfra, Geoff C Gardner, Loren N Pfeiffer, and Ken W West. Observation of electron states of small period artificial graphene in nano-patterned GaAs quantum wells. *Applied Physics Letters*, 109(11):113101, 2016.

[253] Christophe Delerue. Prediction of robust two-dimensional topological insulators based on Ge/Si nanotechnology. *Physical Review B*, 90(7):075424, 2014.

[254] Christophe Delerue and D Vanmaekelbergh. Electronic band structure of zinc blende CdSe and rock salt PbSe semiconductors with silicene-type honeycomb geometry. *2D Materials*, 2(3):034008, 2015.

[255] Athmane Tadjine and Christophe Delerue. Colloidal nanocrystals as LEGO® bricks for building electronic band structure models. *Physical Chemistry Chemical Physics*, 20(12):8177–8184, 2018.

[256] Wiel H Evers, Bart Goris, Sara Bals, Marianna Casavola, Joost De Graaf, Rene Van Roij, Marjolein Dijkstra, and Daniël Vanmaekelbergh. Low-dimensional semiconductor superlattices formed by geometric control over nanocrystal attachment. *Nano letters*, 13(6):2317–2323, 2013.

[257] Mark P Boneschanscher, Wiel H Evers, Jaco J Geuchies, Thomas Altantzis, Bart Goris, Freddy T Rabouw, SAP Van Rossum, Herre SJ van der Zant, Laurent DA Siebbeles, Gustaaf Van Tendeloo, et al. Long-range orientation and atomic attachment of nanocrystals in 2D honeycomb superlattices. *Science*, 344(6190):1377–1380, 2014.

[258] Wiel H Evers, Juleon M Schins, Michiel Aerts, Aditya Kulkarni, Pierre Capiod, Maxime Berthe, Bruno Grandidier, Christophe Delerue, Herre SJ Van Der Zant, Carlo Van Overbeek, et al. High charge mobility in two-dimensional percolative networks of PbSe quantum dots connected by atomic bonds. *Nature communications*, 6(1):1–8, 2015.

[259] Joep L Peters, Thomas Altantzis, Ivan Lobato, Maryam Alimoradi Jazi, Carlo Van Overbeek, Sara Bals, Daniel Vanmaekelbergh, and Sophia Buhbut Sinai. Mono-and multilayer silicene-type honeycomb lattices by oriented attachment of PbSe nanocrystals: synthesis, structural characterization, and analysis of the disorder. *Chemistry of materials*, 30(14):4831–4837, 2018.

[260] Carlo Van Overbeek, Joep L Peters, Susan AP Van Rossum, Marc Smits, Marijn A Van Huis, and Daniel Vanmaekelbergh. Interfacial self-assembly and oriented attachment in the family of PbX (X= S, Se, Te) nanocrystals. *The Journal of Physical Chemistry C*, 122(23):12464–12473, 2018.

[261] Thomas S Gardenier, Jette J van den Broeke, Jesper R Moes, Ingmar Swart, Christophe Delerue, Marlou R Slot, C Morais Smith, and Daniel Vanmaekelbergh. p Orbital flat band and Dirac cone in the electronic honeycomb lattice. *ACS nano*, 14(10):13638–13644, 2020.

[262] Conan Weeks and Marcel Franz. Topological insulators on the Lieb and perovskite lattices. *Physical Review B*, 82(8):085310, 2010.

[263] Elliott H Lieb. Two theorems on the Hubbard model. *Physical review letters*, 62(10):1201, 1989.

[264] Sebabrata Mukherjee, Alexander Spracklen, Debaditya Choudhury, Nathan Goldman, Patrik Öhberg, Erika Andersson, and Robert R Thomson. Observation of a localized flat-band state in a photonic Lieb lattice. *Physical review letters*, 114(24):245504, 2015.

[265] Rodrigo A Vicencio, Camilo Cantillano, Luis Morales-Inostroza, Bastián Real, Cristian Mejía-Cortés, Steffen Weimann, Alexander Szameit, and Mario I Molina. Observation of localized states in Lieb photonic lattices. *Physical review letters*, 114(24):245503, 2015.

[266] Aleksi Julku, Sebastiano Peotta, Tuomas I Vanhala, Dong-Hee Kim, and Päivi Törmä. Geometric origin of superfluidity in the Lieb-lattice flat band. *Physical review letters*, 117(4):045303, 2016.

[267] Shiqiang Xia, Yi Hu, Daohong Song, Yuanyuan Zong, Liqin Tang, and Zhigang Chen. Demonstration of flat-band image transmission in optically induced Lieb photonic lattices. *Optics Letters*, 41(7):1435–1438, 2016.

[268] M Niţă, B Ostahie, and A Aldea. Spectral and transport properties of the two-dimensional Lieb lattice. *Physical Review B*, 87(12):125428, 2013.

[269] NB Kopnin and AS Melnikov. Proximity-induced superconductivity in two-dimensional electronic systems. *Physical Review B*, 84(6):064524, 2011.

[270] Vesa Apaja, Markku Hyrkäs, and Matti Manninen. Flat bands, Dirac cones, and atom dynamics in an optical lattice. *Physical Review A*, 82(4):041402, 2010.

[271] Shintaro Taie, Hideki Ozawa, Tomohiro Ichinose, Takuei Nishio, Shuta Nakajima, and Yoshiro Takahashi. Coherent driving and freezing of bosonic matter wave in an optical Lieb lattice. *Science Advances*, 1(10):e1500854, 2015.

[272] Hideki Ozawa, Shintaro Taie, Tomohiro Ichinose, and Yoshiro Takahashi. Interaction-driven shift and distortion of a flat band in an optical Lieb lattice. *Physical review letters*, 118(17):175301, 2017.

[273] Falko Diebel, Daniel Leykam, Sebastian Kroesen, Cornelia Denz, and Anton S Desyatnikov. Conical diffraction and composite Lieb bosons in photonic lattices. *Physical review letters*, 116(18):183902, 2016.

[274] Shiqi Xia, Ajith Ramachandran, Shiqiang Xia, Denghui Li, Xiuying Liu, Liqin Tang, Yi Hu, Daohong Song, Jingjun Xu, Daniel Leykam, et al. Unconventional flatband line states in photonic Lieb lattices. *Physical review letters*, 121(26):263902, 2018.

[275] CE Whittaker, Emiliano Cancellieri, PM Walker, DR Gulevich, H Schomerus, D Vaitiekus, B Royall, DM Whittaker, E Clarke, IV Iorsh, et al. Exciton polaritons in a two-dimensional lieb lattice with spin-orbit coupling. *Physical review letters*, 120(9):097401, 2018.

[276] Zi-He Yang, Yan-Pu Wang, Zheng-Yuan Xue, Wan-Li Yang, Yong Hu, Jin-Hua Gao, and Ying Wu. Circuit quantum electrodynamics simulator of flat band physics in a Lieb lattice. *Physical Review A*, 93(6):062319, 2016.

[277] Rui Chen and Bin Zhou. Finite size effects on the helical edge states on the Lieb lattice. *Chinese Physics B*, 25(6):067204, 2016.

[278] T Kock, C Hippler, A Ewerbeck, and A Hemmerich. Orbital optical lattices with bosons. *Journal of Physics B: Atomic, Molecular and Optical Physics*, 49(4):042001, 2016.

[279] MR Slot, SN Kempkes, EJ Knol, WMJ van Weerdenburg, JJ van den Broeke, D Wegner, D Vanmaekelbergh, AA Khajetoorians, C Morais Smith, and I Swart. p-Band Engineering in Artificial Electronic Lattices. *Phys. Rev. X*, 9(1):011009, 2019.

[280] Dan Shechtman, Ilan Blech, Denis Gratias, and John W Cahn. Metallic phase with long-range orientational order and no translational symmetry. *Physical review letters*, 53(20):1951, 1984.

[281] Dan Shechtman and Ilan A Blech. The microstructure of rapidly solidified Al 6 Mn. *Metallurgical Transactions A*, 16(6):1005–1012, 1985.

[282] Chaney Lin, Lincoln S Hollister, Glenn J MacPherson, Luca Bindi, Chi Ma, Christopher L Andronicos, and Paul J Steinhardt. Evidence of cross-cutting and redox reaction in Khatyrka meteorite reveals metallic-Al minerals formed in outer space. *Scientific reports*, 7(1):1–14, 2017.

[283] Jian Shang, Yongfeng Wang, Min Chen, Jingxin Dai, Xiong Zhou, Julian Kuttner, Gerhard Hilt, Xiang Shao, J Michael Gottfried, and Kai Wu. Assembling molecular Sierpiński triangle fractals. *Nature chemistry*, 7(5):389–393, 2015.

[284] Sarang Gopalakrishnan, Ivar Martin, and Eugene A Demler. Quantum quasicrystals of spin-orbit-coupled dipolar bosons. *Physical review letters*, 111(18):185304, 2013.

[285] Anuradha Jagannathan and Michel Duneau. An eightfold optical quasicrystal with cold atoms. *EPL (Europhysics Letters)*, 104(6):66003, 2014.

[286] Z Valy Vardeny, Ajay Nahata, and Amit Agrawal. Optics of photonic quasicrystals. *Nature photonics*, 7(3):177–187, 2013.

[287] Laura C Collins, Thomas G Witte, Rochelle Silverman, David B Green, and Kenjiro K Gomes. Imaging quasiperiodic electronic states in a synthetic Penrose tiling. *Nat. Commun.*, 8:15961, 2017.

[288] SN Kempkes, MR Slot, SE Freeney, SJM Zevenhuizen, D Vanmaekelbergh, I Swart, and C Morais Smith. Design and characterization of electrons in a fractal geometry. *Nat. Phys.*, 15(2):127, 2019.

[289] Tsuneya Ando, Alan B Fowler, and Frank Stern. Electronic properties of two-dimensional systems. *Reviews of Modern Physics*, 54(2):437, 1982.

[290] K v Klitzing, Gerhard Dorda, and Michael Pepper. New method for high-accuracy determination of the fine-structure constant based on quantized Hall resistance. *Physical review letters*, 45(6):494, 1980.

[291] Bertrand I Halperin. Quantized Hall conductance, current-carrying edge states, and the existence of extended states in a two-dimensional disordered potential. *Physical Review B*, 25(4):2185, 1982.

[292] Bertrand I Halperin. Theory of the quantized Hall conductance. *Helvetica Physica Acta*, 56(1-3):75–102, 1983.

[293] RR Du, DC Tsui, HL Stormer, LN Pfeiffer, and KW West. Experimental evidence for composite particles in the fractional quantum Hall effect. *Surface science*, 305(1-3):18–22, 1994.

[294] Robert B Laughlin. Anomalous quantum Hall effect: an incompressible quantum fluid with fractionally charged excitations. *Physical Review Letters*, 50(18):1395, 1983.

[295] Bertrand I Halperin. Statistics of quasiparticles and the hierarchy of fractional quantized Hall states. *Physical Review Letters*, 52(18):1583, 1984.

[296] Warren S McCulloch and Walter Pitts. A logical calculus of the ideas immanent in nervous activity. *The bulletin of mathematical biophysics*, 5(4):115–133, 1943.

[297] Frank Rosenblatt. The perceptron: a probabilistic model for information storage and organization in the brain. *Psychological review*, 65(6):386, 1958.

[298] Yann LeCun, Yoshua Bengio, and Geoffrey Hinton. Deep learning. *nature*, 521(7553):436–444, 2015.

[299] A. Rosebrock. *Deep Learning for Computer Vision with Python: Starter Bundle*. PyImageSearch, 2017.

[300] J. Brownlee. *Deep Learning for Computer Vision: Image Classification, Object Detection, and Face Recognition in Python*. Machine Learning Mastery, 2019.

[301] Andrej Karpathy. Convolutional Neural Networks (CNNs / ConvNets). `https://cs231n.github.io/convolutional-networks/`, 2015.

[302] Ian Goodfellow, Yoshua Bengio, and Aaron Courville. *Deep Learning*. MIT Press, 2016. `http://www.deeplearningbook.org`.

[303] Richard AJ Woolley, Julian Stirling, Adrian Radocea, Natalio Krasnogor, and Philip Moriarty. Automated probe microscopy via evolutionary optimization at the atomic scale. *Applied Physics Letters*, 98(25):253104, 2011.

[304] Saoirsé Erin Freeney, Jonathan Catton, and Philip Moriarty. Towards Autonomous Scanning Probe Microscopy. 2016. *Email saoirse.freeney@gmail.com for a copy.*

[305] Sumit Tewari, Koen M Bastiaans, Milan P Allan, and Jan M van Ruitenbeek. Robust procedure for creating and characterizing the atomic structure of scanning tunneling microscope tips. *Beilstein journal of nanotechnology*, 8(1):2389–2395, 2017.

[306] Mohammad Rashidi and Robert A Wolkow. Autonomous scanning probe microscopy in situ tip conditioning through machine learning. *ACS nano*, 12(6):5185–5189, 2018.

[307] L Burzawa, Shuo Liu, and EW Carlson. Classifying surface probe images in strongly correlated electronic systems via machine learning. *Physical Review Materials*, 3(3):033805, 2019.

[308] O Gordon, P D'Hondt, L Knijff, SE Freeney, F Junqueira, P Moriarty, and I Swart. Scanning tunneling state recognition with multi-class neural network ensembles. *Review of Scientific Instruments*, 90(10):103704, 2019.

[309] Benjamin Alldritt, Prokop Hapala, Niko Oinonen, Fedor Urtev, Ondrej Krejci, Filippo Federici Canova, Juho Kannala, Fabian Schulz, Peter Liljeroth, and Adam S Foster. Automated structure discovery in atomic force microscopy. *Science advances*, 6(9):eaay6913, 2020.

[310] Jeffrey Donahue, Lisa Anne Hendricks, Sergio Guadarrama, Marcus Rohrbach, Subhashini Venugopalan, Kate Saenko, and Trevor Darrell. Long-term recurrent convolutional networks for visual recognition and description. In *Proceedings of the IEEE conference on computer vision and pattern recognition*, pages 2625–2634, 2015.

[311] Oliver M Gordon, Filipe LQ Junqueira, and Philip J Moriarty. Embedding human heuristics in machine-learning-enabled probe microscopy. *Machine Learning: Science and Technology*, 1(1):015001, 2020.

[312] Mohammad Rashidi, Jeremiah Croshaw, Kieran Mastel, Marcus Tamura, Hedieh Hosseinzadeh, and Robert A Wolkow. Deep learning-guided surface characterization for autonomous hydrogen lithography. *Machine Learning: Science and Technology*, 1(2):025001, 2020.

[313] Alexander Krull, P Hirsch, C Rother, A Schiffrin, and C Krull. Artificial-intelligence-driven scanning probe microscopy. *Communications Physics*, 3(1):1–8, 2020.

[314] Yi Zhang, A Mesaros, Kazuhiro Fujita, SD Edkins, MH Hamidian, K Ch'ng, H Eisaki, S Uchida, JC Séamus Davis, Ehsan Khatami, et al. Machine learning in electronic-quantum-matter imaging experiments. *Nature*, 570(7762):484–490, 2019.

[315] Oliver M Gordon, Jo EA Hodgkinson, Steff M Farley, Eugénie L Hunsicker, and Philip J Moriarty. Automated Searching and Identification of Self-Organised Nanostructures. *Nano Letters*, 2020.

[316] Olaf Ronneberger, Philipp Fischer, and Thomas Brox. U-net: Convolutional networks for biomedical image segmentation. In *International Conference on Medical image computing and computer-assisted intervention*, pages 234–241. Springer, 2015.

[317] Steff Farley, Jo EA Hodgkinson, Oliver M Gordon, Joanna Turner, Andrea Soltoggio, Philip J Moriarty, and Eugenie Hunsicker. Improving the segmentation of scanning probe microscope images using convolutional neural networks. *arXiv preprint arXiv:2008.12371*, 2020.

[318] Stephan Zevenhuizen. Flattening Images with Step Edges. `https://webspace.science.uu.nl/~zeven101/SPIEPy/example3.html`, 2017.

[319] Justin M Johnson and Taghi M Khoshgoftaar. Survey on deep learning with class imbalance. *Journal of Big Data*, 6(1):27, 2019.

[320] Karen Simonyan and Andrew Zisserman. Very deep convolutional networks for large-scale image recognition. *arXiv preprint arXiv:1409.1556*, 2014.

[321] Olga Russakovsky, Jia Deng, Hao Su, Jonathan Krause, Sanjeev Satheesh, Sean Ma, Zhiheng Huang, Andrej Karpathy, Aditya Khosla, Michael Bernstein, et al. Imagenet large scale visual recognition challenge. *International journal of computer vision*, 115(3):211–252, 2015.

[322] Diederik P Kingma and Jimmy Ba. Adam: A method for stochastic optimization. *arXiv preprint arXiv:1412.6980*, 2014.

[323] Thomas G Dietterich. Ensemble methods in machine learning. In *International workshop on multiple classifier systems*, pages 1–15. Springer, 2000.

[324] Tsung-Yi Lin, Genevieve Patterson, Matteo R Ronchi, Yin Cui, Michael Maire, Serge Belongie, Lubomir Bourdev, Ross Girshick, James Hays, Pietro Perona, and et al. Common Objects in Context. `https://cocodataset.org/`, 2020.

[325] Mark Everingham, Luc Van Gool, Christopher KI Williams, John Winn, and Andrew Zisserman. The pascal visual object classes (voc) challenge. *International journal of computer vision*, 88(2):303–338, 2010.

[326] J. Deng, W. Dong, R. Socher, L.-J. Li, K. Li, and L. Fei-Fei. ImageNet: A Large-Scale Hierarchical Image Database. In *CVPR09*, 2009.

[327] Alex Krizhevsky, Geoffrey Hinton, et al. Learning multiple layers of features from tiny images. 2009.

[328] Ruben Perez. SPMImages. `https://spmportal.quasarsr.com/spmportal/user-guide`, 2019.

[329] Morten Møller, Samuel P Jarvis, Laurent Guérinet, Peter Sharp, Richard Woolley, Philipp Rahe, and Philip Moriarty. Automated extraction of single H atoms with STM: tip state dependency. *Nanotechnology*, 28(7):075302, 2017.

[330] Raban Iten, Tony Metger, Henrik Wilming, Lídia Del Rio, and Renato Renner. Discovering physical concepts with neural networks. *Physical Review Letters*, 124(1):010508, 2020.

[331] Google Machine Learning Crash Course. Classification: Accuracy. `https://developers.google.com/machine-learning/crash-course/classification/accuracy`, 2020.

[332] TensorFlow. tf.keras.layers.Dropout. `https://www.tensorflow.org/api_docs/python/tf/keras/layers/Dropout`, 2020.

[333] M. F. Crommie, C. P. Lutz, and D. M. Eigler. Confinement of electrons to quantum corrals on a metal surface. *Science*, 262(5131):218–220, 1993.

[334] Christopher R. Moon, Laila S. Mattos, Brian K. Foster, Gabriel Zeltzer, and Hari C. Manoharan. Quantum holographic encoding in a two-dimensional electron gas. *Nat. Nanotechnol.*, 4:167–172, 2009.

[335] Sebastian Loth, Susanne Baumann, Christopher P. Lutz, D. M. Eigler, and Andreas J. Heinrich. Bistability in Atomic-Scale Antiferromagnets. *Science*, 335(6065):196–199, 2012.

[336] F. E. Kalff, M. P. Rebergen, E. Fahrenfort, J. Girovsky, R. Toskovic, J. L. Lado, J. Fernández-Rossier, and A. F. Otte. A kilobyte rewritable atomic memory. *Nat. Nanotechnol.*, 11:926–929, 2016.

[337] Roshan Achal, Mohammad Rashidi, Jeremiah Croshaw, David Churchill, Marco Taucer, Martin Cloutier Taleana Huff, Jason Pitters, and Robert A. Wolkow. Lithography for robust and editable atomic-scale silicon devices and memories. *Nat. Commun.*, 9:2778, 2018.

[338] A. J. Heinrich, C. P. Lutz, J. A. Gupta, and D. M. Eigler. Molecule Cascades. *Science*, 298(5597):1381–1387, 2002.

[339] Alexander Ako Khajetoorians, Jens Wiebe, Bruno Chilian, and Roland Wiesendanger. Realizing All-Spin–Based Logic Operations Atom by Atom. *Science*, 332(6033):1062–1064, 2011.

[340] Marek Kolmer, Rafal Zuzak, Ghassen Dridi, Szymon Godlewski, Christian Joachim, and Marek Szymonski. Realization of a quantum Hamiltonian Boolean logic gate on the Si(001):H surface. *Nanoscale*, 7:12325–12330, 2015.

[341] Taleana Huff, Hatem Labidi, Mohammad Rashidi, Lucian Livadaru, Thomas Dienel, Roshan Achal, Wyatt Vine, Jason Pitters, and Robert A. Wolkow. Binary atomic silicon logic. *Nat. Electronics*, 1:636–643, 2018.

[342] J. R. Hahn and W. Ho. Oxidation of a Single Carbon Monoxide Molecule Manipulated and Induced with a Scanning Tunneling Microscope. *Phys. Rev. Lett.*, 87:166102, 2001.

[343] Saw-Wai Hla, Ludwig Bartels, Gerhard Meyer, and Karl-Heinz Rieder. Inducing All Steps of a Chemical Reaction with the Scanning Tunneling Microscope Tip: Towards Single Molecule Engineering. *Phys. Rev. Lett.*, 85:2777–2780, 2000.

[344] Ingmar Swart, Leo Gross, and Peter Liljeroth. Single-molecule chemistry and physics explored by low-temperature scanning probe microscopy. *Chem. Commun.*, 47:9011–9023, 2011.

[345] Florian Albrecht, Matthias Neu, Christina Quest, Ingmar Swart, and Jascha Repp. Formation and characterization of a molecule–metal–molecule bridge in real space. *J. Am. Chem. Soc.*, 135:9200–9203, 2013.

[346] A. A. Khajetoorians, D. Wegner, A.F. Otte, and I. Swart. Creating designer quantum states of matter atom- by-atom. *Nat. Rev. Phys.*, 1:703–715, 2019.

[347] Wonhee Ko, Chuanxu Ma, Giang D. Nguyen, Marek Kolmer, and An-Ping Li. Atomic-Scale Manipulation and In Situ Characterization with Scanning Tunneling Microscopy. *Advanced Functional Materials*, 29:1903770, 2019.

[348] N. Nilius, T. M. Wallis, and W. Ho. Development of one- dimensional band structure in artificial gold chains. *Science*, 297:1853–1856, 2002.

[349] S. Fölsch, P. Hyldgaard, R. Koch, and K. H. Ploog. Quantum confinement in monatomic Cu chains on Cu(111). *Phys. Rev. Lett.*, 92:056803, 2004.

[350] Stefan Fölsch, Jianshu Yang, Christophe Nacci, and Kiyoshi Kanisawa. Atom-By-Atom Quantum State Control in Adatom Chains on a Semiconductor. *Phys. Rev. Lett.*, 103:096104, Aug 2009.

[351] Bruno Schuler, Mats Persson, Sami Paavilainen, Niko Pavliček, Leo Gross, Gerhard Meyer, and Jascha Repp. Effect of electron-phonon interaction on the formation of one-dimensional electronic states in coupled Cl vacancies. *Phys. Rev. B*, 91:235443, 2015.

[352] Jan Girovsky, Jose L. Lado, Floris E. Kalff, Eleonora Fahrenfort, Lucas J. J. M. Peters, Joaquín Fernández-Rossier, and Alexander F. Otte. Emergence of quasiparticle Bloch states in artificial crystals crafted atom-by-atom. *SciPost Phys.*, 2:020, 2017.

[353] S. R. Schofield, P. Studer, N. J. Hirjibehedin, C. F.and Curson, G. Aeppli, and D. R. Bowler. Quantum engineering at the silicon surface using dangling bonds. *Nat. Commun.*, 4:1649, 2013.

[354] Jae Whan Park, Hyo Sung Kim, Thomas Brumme, Thomas Heine, and Han Woong Yeom. Artificial relativistic molecules. *Nat. Commun.*, 11:815, 2020.

[355] Howon Kim, Alexandra Palacio-Morales, Thore Posske, Levente Rózsa, Krisztián Palotás, László Szunyogh, Michael Thorwart, and Roland Wiesendanger. Toward tailoring Majorana bound states in artificially constructed magnetic atom chains on elemental superconductors. *Science Advances*, 4(5), 2018.

[356] Christopher R Moon, Laila S Mattos, Brian K Foster, Gabriel Zeltzer, Wonhee Ko, and Hari C Manoharan. Quantum phase extraction in isospectral electronic nanostructures. *Science*, 319(5864):782–787, 2008.

[357] SN Kempkes, MR Slot, JJ van den Broeke, P Capiod, WA Benalcazar, D Vanmaekelbergh, D Bercioux, I Swart, and C Morais Smith. Robust zero-energy modes in an electronic higher-order topological insulator. *Nat. Mater.*, 18(12):1292–1297, 2019.

[358] Gregory A. Fiete and Eric J. Heller. Colloquium: Theory of quantum corrals and quantum mirages. *Rev. Mod. Phys.*, 75(3):933–948, 2003.

[359] S. E. Freeney, J. J. van den Broeke, A. J. J. Harsveld van der Veen, I. Swart, and C. Morais Smith. Edge-dependent topology in Kekulé lattices. *Phys. Rev. Lett.*, 124:236404, 2020.

[360] Wai-Kee Li and SM Blinder. Particle in an equilateral triangle: Exact solution of a nonseparable problem. *J. Chem. Educ.*, 64(2):130, 1987.

[361] David J Griffiths and Darrell F Schroeter. *Introduction to quantum mechanics*. Cambridge University Press, 2018.

[362] L. Bartels, G. Meyer, and K.-H. Rieder. Basic steps involved in the lateral manipulation of single CO molecules and rows of CO molecules. *Chem. Phys. Lett.*, 273(5):371 – 375, 1997.

[363] Robert J. Celotta, Stephen B. Balakirsky, Aaron P. Fein, Frank M. Hess, Gregory M. Rutter, and Joseph A. Stroscio. Invited Article: Autonomous assembly of atomically perfect nanostructures using a scanning tunneling microscope. *Rev. Sci. Inst.*, 85:121301, 2014.

[364] L Bartels, G Meyer, and K-H Rieder. The evolution of CO adsorption on Cu (111) as studied with bare and CO-functionalized scanning tunneling tips. *Surf. Sci.*, 432(3):L621–L626, 1999.

[365] Alexander Gustafsson and Magnus Paulsson. Scanning tunneling microscopy current from localized basis orbital density functional theory. *Phys. Rev. B*, 93(11):115434, 2016.

[366] Shigemitsu Nakanishi and Tetsuo Horiguchi. Surface lattice constants of Si (111), Ni (111) and Cu (111). *Jpn. J. Appl. Phys.*, 20(3):L214, 1981.

[367] David G Pettifor and David Pettifor. *Bonding and structure of molecules and solids*, volume 193. Clarendon Press Oxford, 1995.

[368] Jeremy K Burdett et al. *Chemical bonding in solids*. Oxford University Press, 1995.

[369] S Crampin, MH Boon, and JE Inglesfield. Influence of bulk states on laterally confined surface state electrons. *Phys. Rev. Lett.*, 73(7):1015, 1994.

[370] Takuya Kumagai and Akira Tamura. Analysis of scanning tunneling microscopy images and scanning tunneling spectrum of electrons confined in equilateral triangular quantum corrals. *J. Phys. Soc. Jpn.*, 77(1):014601, 2007.

[371] GB Shaw. Degeneracy in the particle-in-a-box problem. *J. Phys. A: Math. Nuc.Gen.*, 7(13):1537, 1974.

[372] David J Thouless, Mahito Kohmoto, M Peter Nightingale, and Md den Nijs. Quantized Hall conductance in a two-dimensional periodic potential. *Phys. Rev. Lett.*, 49(6):405, 1982.

[373] Alexander Altland and Martin R Zirnbauer. Nonstandard symmetry classes in mesoscopic normal-superconducting hybrid structures. *Phys. Rev. B*, 55(2):1142, 1997.

[374] Liang Fu. Topological crystalline insulators. *Phys. Rev. Lett.*, 106(10):106802, 2011.

[375] Robert-Jan Slager, Andrej Mesaros, Vladimir Juričić, and Jan Zaanen. The space group classification of topological band-insulators. *Nat. Phys.*, 9(2):98, 2013.

[376] Anand Kamlapure, Lasse Cornils, Jens Wiebe, and Roland Wiesendanger. Engineering the spin couplings in atomically crafted spin chains on an elemental superconductor. *Nat. Commun.*, 9(1):3253, 2018.

[377] Toshikaze Kariyado and Xiao Hu. Topological states characterized by mirror winding numbers in graphene with bond modulation. *Sci. Rep.*, 7(1):16515, 2017.

[378] Jiho Noh, Wladimir A Benalcazar, Sheng Huang, Matthew J Collins, Kevin P Chen, Taylor L Hughes, and Mikael C Rechtsman. Topological protection of photonic mid-gap defect modes. *Nat. Photonics*, 12(7):408, 2018.

[379] Kyoko Nakada, Mitsutaka Fujita, Gene Dresselhaus, and Mildred S Dresselhaus. Edge state in graphene ribbons: Nanometer size effect and edge shape dependence. *Phys. Rev. B*, 54(24):17954, 1996.

[380] Mitsutaka Fujita, Katsunori Wakabayashi, Kyoko Nakada, and Koichi Kusakabe. Peculiar localized state at zigzag graphite edge. *J. Phys. Soc. Jpn*, 65(7):1920–1923, 1996.

[381] David Nečas and Petr Klapetek. Gwyddion: an open-source software for SPM data analysis. *Open Phys.*, 10(1):181–188, 2012.

[382] Shuai Li, Wen-Xuan Qiu, and Jin-Hua Gao. Designing artificial two dimensional electron lattice on metal surface: a Kagome-like lattice as an example. *Nanoscale*, 8(25):12747–12754, 2016.

[383] Daniel C Mattis. The few-body problem on a lattice. *Reviews of Modern Physics*, 58(2):361, 1986.

[384] John Hubbard. Electron correlations in narrow energy bands V. A perturbation expansion about the atomic limit. *Proceedings of the Royal Society of London. Series A. Mathematical and Physical Sciences*, 296(1444):82–99, 1967.

[385] K Winkler, G Thalhammer, F Lang, R Grimm, J Hecker Denschlag, AJ Daley, A Kantian, HP Büchler, and P Zoller. Repulsively bound atom pairs in an optical lattice. *Nature*, 441(7095):853–856, 2006.

[386] Niels Strohmaier, Daniel Greif, Robert Jördens, Leticia Tarruell, Henning Moritz, Tilman Esslinger, Rajdeep Sensarma, David Pekker, Ehud Altman, and Eugene Demler. Observation of elastic doublon decay in the Fermi-Hubbard model. *Physical review letters*, 104(8):080401, 2010.

[387] Michael Schreiber, Sean S Hodgman, Pranjal Bordia, Henrik P Lüschen, Mark H Fischer, Ronen Vosk, Ehud Altman, Ulrich Schneider, and Immanuel Bloch. Observation of many-body localization of interacting fermions in a quasirandom optical lattice. *Science*, 349(6250):842–845, 2015.

[388] L Barbiero, C Menotti, A Recati, and L Santos. Out-of-equilibrium states and quasi-many-body localization in polar lattice gases. *Physical Review B*, 92(18):180406, 2015.

[389] Grazia Salerno, Giandomenico Palumbo, Nathan Goldman, and Marco Di Liberto. Interaction-induced lattices for bound states: Designing flat bands, quantized pumps, and higher-order topological insulators for doublons. *Physical Review Research*, 2(1):013348, 2020.

[390] WP Su, JR Schrieffer, and Ao J Heeger. Solitons in polyacetylene. *Physical review letters*, 42(25):1698, 1979.

[391] Maxim A Gorlach and Alexander N Poddubny. Topological edge states of bound photon pairs. *Physical Review A*, 95(5):053866, 2017.

[392] Maxim A Gorlach and Alexander N Poddubny. Interaction-induced two-photon edge states in an extended Hubbard model realized in a cavity array. *Physical Review A*, 95(3):033831, 2017.

[393] M Bello, Charles E Creffield, and Gloria Platero. Long-range doublon transfer in a dimer chain induced by topology and ac fields. *Scientific reports*, 6:22562, 2016.

[394] Miguel Bello, Charles E Creffield, and Gloria Platero. Sublattice dynamics and quantum state transfer of doublons in two-dimensional lattices. *Physical Review B*, 95(9):094303, 2017.

[395] Marco Di Liberto, Alessio Recati, Iacopo Carusotto, and Chiara Menotti. Two-body physics in the Su-Schrieffer-Heeger model. *Physical Review A*, 94(6):062704, 2016.

[396] Marco Di Liberto, Alessio Recati, Iacopo Carusotto, and Chiara Menotti. Two-body bound and edge states in the extended SSH Bose-Hubbard model. *The European Physical Journal Special Topics*, 226(12):2751–2762, 2017.

[397] Nikita A Olekhno, Egor I Kretov, Andrei A Stepanenko, Polina A Ivanova, Vitaly V Yaroshenko, Ekaterina M Puhtina, Dmitry S Filonov, Barbara Cappello, Ladislau Matekovits, and Maxim A Gorlach. Topological edge states of interacting photon pairs emulated in a topolectrical circuit. *Nature Communications*, 11(1):1–8, 2020.

[398] Daniel C Tsui, Horst L Stormer, and Arthur C Gossard. Two-dimensional magnetotransport in the extreme quantum limit. *Physical Review Letters*, 48(22):1559, 1982.

[399] Ching-Kai Chiu, Jeffrey CY Teo, Andreas P Schnyder, and Shinsei Ryu. Classification of topological quantum matter with symmetries. *Reviews of Modern Physics*, 88(3):035005, 2016.

[400] Stefano Longhi. Photonic Bloch oscillations of correlated particles. *Optics letters*, 36(16):3248–3250, 2011.

[401] Giacomo Corrielli, Andrea Crespi, Giuseppe Della Valle, Stefano Longhi, and Roberto Osellame. Fractional Bloch oscillations in photonic lattices. *Nature communications*, 4(1):1–6, 2013.

[402] Dmitry O Krimer and Ramaz Khomeriki. Realization of discrete quantum billiards in a two-dimensional optical lattice. *Physical Review A*, 84(4):041807, 2011.

[403] Marlou Slot. *Patterning atomic flatland: Electronic lattices crafted atom by atom*. PhD thesis, Utrecht University, 2019.

[404] Bernard A Lippmann and Julian Schwinger. Variational principles for scattering processes. I. *Physical Review*, 79(3):469, 1950.

[405] Alexander Blech, Yuval Shagam, Nicolas Hölsch, Prerna Paliwal, Wojciech Skomorowski, John W Rosenberg, Natan Bibelnik, Oded Heber, Daniel M Reich, Edvardas Narevicius, et al. Phase protection of Fano-Feshbach resonances. *Nature communications*, 11(1):1–7, 2020.

[406] SE Freeney, JJ van Den Broeke, AJJ Harsveld van der Veen, I Swart, and C Morais Smith. Edge-dependent topology in Kekulé lattices. *Physical Review Letters*, 124(23):236404, 2020.

[407] Jerry Tersoff and Donald R Hamann. Theory of the scanning tunneling microscope. *Physical Review B*, 31(2):805, 1985.

[408] S Crampin, M H Boon, and J E Inglesfield. Influence of Bulk States on Laterally Confined Surface State Electrons. *Physical Review Letters*, 73(7):1015–1018, aug 1994.

CHAPTER 7

APPENDIX

7.1 Summary in English

In this thesis, we investigated artificial atoms, molecules, lattices and intelligence in the context of scanning tunnelling microscopy (STM). We manipulated individual carbon monoxide molecules on a copper(111) surface, which allowed us to sculpt the electrical potential landscape at will. Figure 7.1 shows an example of a variety of quantum objects shaped into the surface in this way. Since a large part of the electronic behaviour in a material can be attributed to its geometry, we were able to experimentally mimic theoretical models. As highlighted in chapter 2, an assortment of artificial lattices had already been established using this platform. In this thesis, we expanded upon this framework with both new examples, and by investigating the artificial atoms and molecules that make up such lattices. Aside from this, we also developed a neural-network based algorithm that could categorise STM images based on tip state, paving the way for more efficient scanning probe microscopy. In the following pages, we summarise each chapter.

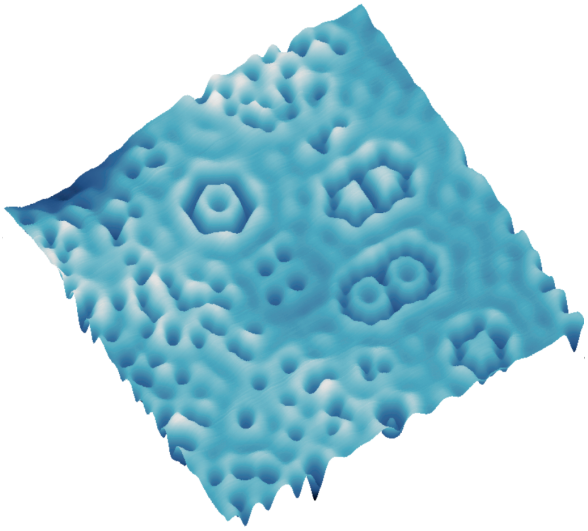

▲ Figure 7.1: A quantum playground of artificial atoms and molecules. The dips, CO molecules, are seen to scatter the Cu(111) electronic surface state. The dips in the centres of artificial atoms are actually nodes in the wave functions of confined electrons.

7.1.1 Automatic tip conditioning

First, in chapter 3 we sought to improve the efficiency of scanning tunnelling microscopy as a whole. Spending vast amounts of time preparing the STM tip is a common point of lamentation among scanning probe microscopists. However, such repetitive tasks are ripe for automation, and attempts at establishing this are already well underway. We contributed to this work by creating a neural network-based algorithm that could distinguish the state of the tip (that is to say, to categorise an STM image by type; sharp, double, unstable, rubbish, step country or bad country). The dataset used for training the neural network contained images of a gold(111) surface, and the final network ensemble had an accuracy of 88 %. Figure 7.2 shows a typical input and output to the neural network. This chapter represented a step towards the incorporation of automation into scanning probe microscopy. There are currently efforts underway to automate the process for the CO/Cu(111) substrate.

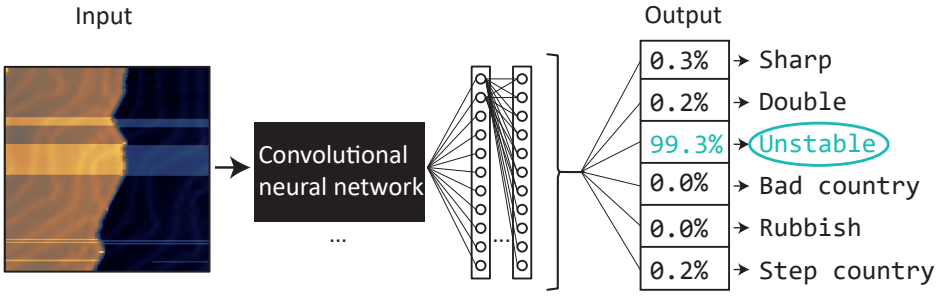

▲ Figure 7.2: We made use of a convolutional neural network (VGG-16) to automatically classify images. On the left, the STM image of Au(111) shows tip changes during the scan. A typical output for an image like this is given on the right, where the prediction for this example is correctly given as "unstable".

7.1.2 Artificial atoms and molecules

In chapter 4, we shifted to the CO/Cu(111) platform. There, we examined quantum simulation on a more fundamental level than in prior work. We investigated the elementary components of artificial lattices constructed with the CO/Cu(111) platform: quantum corrals of square and triangular geometries. Numerous lattices of this type had already been realised at the time of this project, however, the full range of parameters available to tweak (as defined in the tight-binding description) was not known. In a systematic way, we described how the on site energy of triangular and rectangular corrals depend inversely on area, also noting the smaller the corral, the larger the broadening of the peaks in differential conductance spectroscopy. Secondly, we presented a method to extract tight binding parameters by coupling corrals into dimers and trimers, and showed how the parameters could be varied when the size of the corral or the number of CO molecules separating them was altered. We found that the hopping integral could be tuned between 0 and -0.3 eV and -0.16 eV for s- and p-like states respectively, and found that typically, overlap was an important consideration. Finally, we wielded control over artificial orbitals level by coupling s- and p-like states. Furthermore, we selectively formed $s - p_y$ bonds while inhibiting $s - p_x$ bonds. Figure 7.3 summarises the coupling process using the p-like orbitals of triangular corrals as an example.

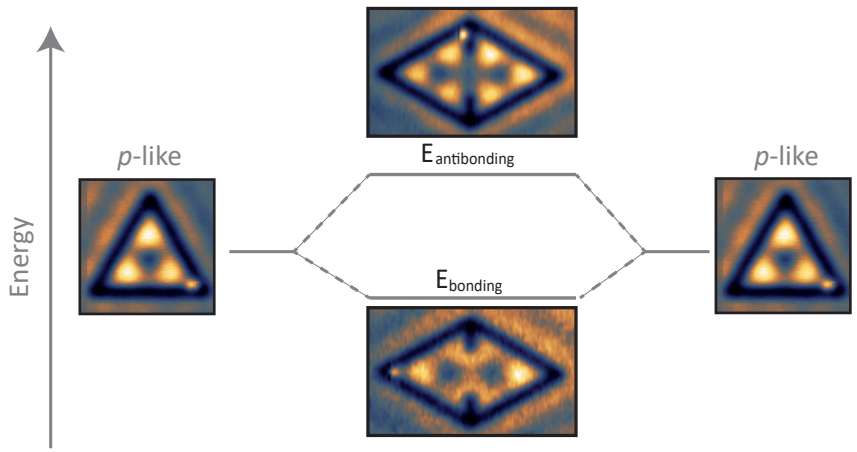

▲ Figure 7.3: Coupling the p-like states of triangular corrals yields bonding and antibonding states.

7.1.3 Concocting topology

Chapter 5 described an example of a lattice which has only been known to exist artificially, in this case, on the CO/Cu(111) platform. Underlying this experimental project was a theoretical prediction: by modulating the bonds in graphene to produce a so-called Kekulé lattice, a gap in the band structure can be opened, but not necessarily at the edges, which may exhibit topologically non-trivial bands, depending on their construction. This is interesting; while being insulators in the bulk, the electronic states at the interfaces of topological insulators are known to be robust, and are not easily perturbed by simple defects. The research question was then: could we mimic this behaviour using the CO/Cu(111) platform? To answer this, we constructed four configurations of a Kekulé lattice, summarised in figure 7.4, where we altered the termination of the crystal (left/right), and the positioning of the bond strengths (reversed in top/bottom). In two cases, edge states were observed, indeed mimicking a topological crystalline insulator. In the other two cases, we obtained entirely insulating systems. The results owed to the underlying symmetries of the system.

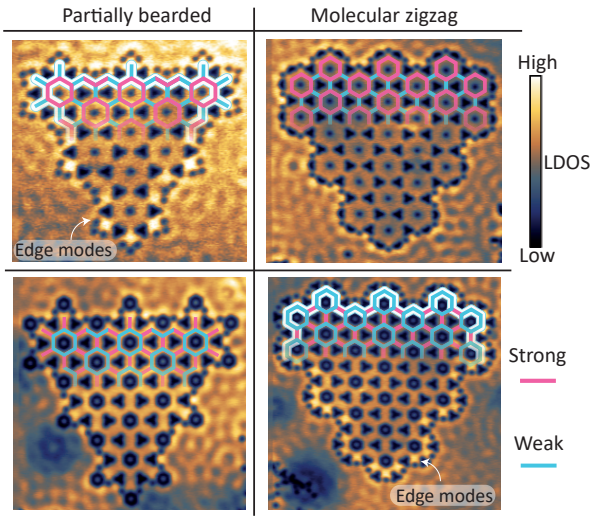

▲ Figure 7.4: Edge modes manifest in two of these configurations of the Kekulé lattice. This is determined by the unit cell, which is different in all four cases.

7.1.4 Simulations within simulations: probing interactions

Finally, chapter 6 delved into the possibility of simulating interactions in electronic quantum simulators. The CO/Cu(111) setup does well at simulating single particle models, but is there a way to simulate two-body physics? The theoretical answer is yes, the Hamiltonian describing two-body interactions on a 1D lattice is identical to the one describing a single particle in 2D. Experimentally, we realised a 2D variant of the Su-Schrieffer-Heeger lattice, for which a certain measurable signature of the simulated two-body interaction was predicted. We found the hint of this signature, however, some experimental shortcomings forbade us from making strong conclusions.

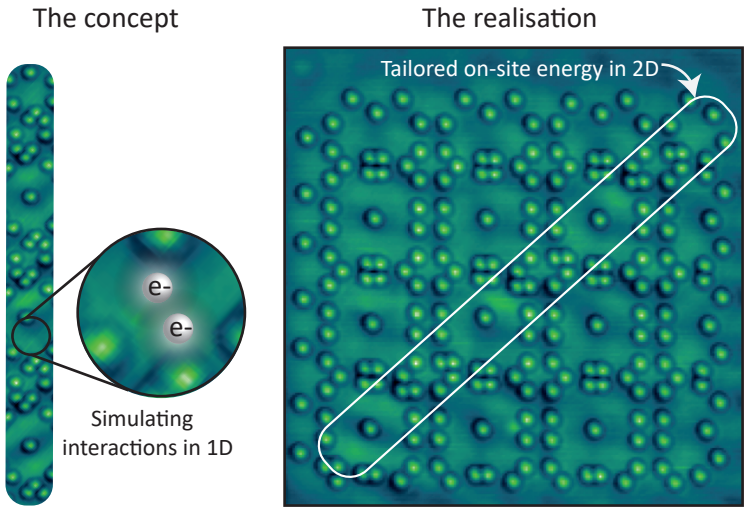

▲ Figure 7.5: On the left is an artistic representation of the interactions we wished to simulate, which are not typically feasible to measure with our experimental setup. On the right is one of the lattices we realised in order to simulate the two-particle interactions. The image was taken with a CO-terminated tip, and the CO molecules appear as protrusions.

7.1.5 Final remarks

The CO on Cu(111) platform is like a quantum playground where we can toy with electronic wavefunctions and tight-binding parameters in lattices. It has been shown to be useful as an experimental model system where we can probe exotic physical phenomena, however, there are some limitations. Firstly, since the surface bands lie at similar energy to bulk bands, the lifetime of surface electrons is diminished, which introduces broadening into differential conductance measurements. Platforms such as the InAs(111) surface, where the surface states are decoupled from the bulk and therefore experience better energy resolution, are a possible remedy. Secondly, certain interactions, such as spin-orbit interactions, cannot be modelled with the CO/Cu(111) platform. One possibility is that by using heavier elements, Rashba spin orbit coupling could be induced.
The efficiency of creating and investigating such artificial structures could be improved using a neural network-based STM image recognition system, generalised for many substrates. Such a system would automatically make tip conditioning decisions based on its input and the type of substrate. Refined automated adsorbate manipulation techniques could be added, as well as the ability to judge differential conductance spectra.
Looking beyond STM-based research techniques, type III-V semiconductors can be patterned with tiny holes using nanolithography, defining a lattice much like described in this thesis. This paves the way to obtain extra information about surfaces of interest, but also the possibility to transfer model systems to technology.

7.2 Samenvatting in het Nederlands

Dit proefschrift beschrijft de creatie van kunstmatige materie op atomaire schaal, molecuul voor molecuul.

Deze uitspraak lijkt misschien fantasierijk voor degenen die het bestaan van een rastertunnelmicroscoop (RTM, STM in het Engels) niet kennen. Deze microscoop kan individuele atomen tonen en ze vervolgens verschuiven. RTM bestaat echter al een halve eeuw,[2] waarbij de RTM zelf in 1981 werd uitgevonden.[3]Het duurde niet lang tot de eerste structuur op atomaire schaal naar wens werd samengesteld; onderzoekers bij IBM schreven de initialen van hun bedrijf met xenon-atomen op een nikkel oppervlak.[4] Vervolgens kwam de kwantumkraal, die elektronen opsloot. De kraal was een ring van ijzeratomen op het (111) oppervlak van koper. Op de (111) terminatie van een koper kristal is een "zee" van elektronen die voortkomen uit de Shockley-toestand. Adsorbaten die op het oppervlak worden geplaatst, verstrooien deze elektronische toestanden, wat resulteert in staande golfpatronen die meetbaar zijn met RTM. Een typisch RTM-topografie plaatje is evenredig met de waarschijnlijkheidsdichtheid $|\Psi|^2$, en doet visueel denken aan de rimpelingen die ontstaan wanneer een regendruppel een plas raakt.

Wanneer adsorbaten zo zijn gerangschikt dat ze een beperkte ruimte omsluiten (in het kwantumkraal-werk[6] uit 1993 was de omhulling cirkelvormig), dan worden de elektronen opgesloten en worden hun golffuncties en energieniveaus gekwantiseerd. Het opmerkelijke is dat deze gekwantiseerde toestanden direct vergelijkbaar zijn met atomair gedrag. Elektronen worden in atomen gevangen door de aantrekkende potentiaal van de atoomkern, in kwantumkralen worden ze opgesloten door een omringende repulsieve potentiaal. Kwantumcorralen kunnen dus als kunstmatige atomen worden beschouwd. Kwantumkralen kunnen aan elkaar worden gekoppeld om kunstmatige moleculen te vormen, die bindende- en antibindende orbitalen vertonen die specifiek zijn voor moleculen. Dit idee kan worden uitgebreid tot volledige kunstmatige twee-dimensionale roosters, door het gewenste potentiaallandschap molecuul voor molecuul te creëren. Het eerste voorbeeld van een op deze manier geconstrueerd rooster was kunstmatig grafeen.[7] Met behulp van koolmonoxide op Cu(111) werd de elektronische oppervlaktetoestand beperkt tot een hexagonaal patroon. De onderzoeksgroep emuleerde niet alleen het gedrag van elektronen in grafeen, ze openden ook een bandkloof door de eenheidscel van het rooster aan te passen. Door veranderen van de roosterconstante werd het kunstmatige grafeen effectief n- of p- gedoteerd. Veranderingen in de roostergeometrie konden ook magnetische velden simuleren. Dit werk onthulde de waarde van kunstmatige roosters die adsorbaat voor adsorbaat worden geproduceerd. Deze roosters zijn in hoge mate instelbaar en metingen van de lokale toestandsdichtheid kunnen onmiddellijk worden uitgevoerd. Al het bovenstaande onderzoek komt bij elkaar tot de kern van dit onderzoeksgebied: we zijn niet beperkt tot het nabootsen van alleen bestaande materialen. Sinds de publicatie van kunstmatig grafeen[7] is er een overvloed aan pub-

licaties geweest over nieuwe systemen die gemodelleerd zijn met hetzelfde platform: CO op Cu(111).
Even terzijde: dit platform als kwantumsimulator is zeker niet de enige mogelijkheid. Momenteel is er een scala aan technieken die controle en meting van kunstmatige kwantumtoestanden mogelijk maken, waaronder (magneto-) optische roosters,[8–11] fotonische roosters,[12] (topo) elektronische circuits[13] en akoestische systemen.[14–16] Zelfs binnen het domein van RTM zijn andere methoden voor de constructie van kunstmatige roosters aan getoond.[17–22]

Hoe creëer je kunstmatige materie?

In het bijzonder, hoe kan men koolmonoxide, koper en een rastertunnelmicroscoop gebruiken om controle uit te oefenen over het gedrag van elektronen? Allereerst moet het koperoppervlak atomair vlak zijn. Een koperkristal wordt geslepen en gepolijst zodat een (111) getermineerd vlak boven ligt (figuur 7.6a) wordt onder vacuüm gebracht, gesputterd en gegloeid. Dit is het proces van het bombarderen van het oppervlak met argonionen om eventuele verontreinigingen te verwijderen, en het opwarmen van het monster zodat de oppervlakte-atomen ontspannen tot hun minimale energieconfiguratie, die dus atomair vlak is. Het monster wordt vervolgens naar de RTM-kamer verplaatst en in de meetkop gepositioneerd, terwijl het in ultrahoog vacuüm blijft. Tijdens dit project hebben we gebruik gemaakt van de Omicron LT-STM getoond in figuur 7.6b, die tot 4.5 K wordt afgekoeld door middel van vloeibaar helium. Eenmaal koud kan koolmonoxide voorzichtig in de kamer worden gelekt, waar het op het Cu(111) oppervlak wordt geabsorbeerd. De RTM heeft een atoomscherpe naald die op een elektrische spanning zit ten opzichte van het monster. Deze naald, of tip, wordt gebruikt om het oppervlak elektronisch te “lezen” zoals braille. Voor het meten wordt de RTM-tip naar het koper oppervlak gebracht totdat een minuscule stroom in de orde van nano-ampère wordt gedetecteerd. Deze stroom komt voort uit kwantummechanisch tunnelen tussen de tip en het monster, en is omgekeerd exponentieel afhankelijk van de afstand daartussen. Dat wil zeggen, hoe kleiner de afstand tussen de tip en het monster, des te waarschijnlijker is het tunnel proces. Het is deze grote gevoeligheid die ons in staat stelt om kenmerken op de subnanometer schaal te kunnen zien. Met behulp van kleine piëzo-elektrische motoren scant de naald over het oppervlak, waarbij een constante stroom wordt gehandhaafd door deze waar nodig lichtjes terug te trekken of te naderen. Figuur 7.6c toont een weergave van een RTM-naald terwijl het een kwantumkraal scant. Gewoonlijk worden CO-moleculen gevisualiseerd als kleine gaten in het oppervlak (zoals te zien in figuren 7.6e en f), maar in figuur 7.6c werd de scan experimenteel verkregen met een CO-getermineerde tip (zwart = koolstof, rood = zuurstof), waardoor CO-moleculen verschijnen als uitsteeksels. De afgelegde route van de naald wordt weergegeven. De hoogte van de naald wordt op elk punt van de scan gemeten en vertaald naar een pixelintensiteit in een RTM-afbeelding. Figuur 7.6d toont een voorbeeld van een Cu(111) -oppervlak, op een

lengteschaal die 10.000 keer kleiner is dan de diameter van het monster. Dit figuur is 500 nm breed, wat de golflengte is van cyaan/groen licht; de terrassen in deze figuur zijn kleiner dan met een optische microscoop zou kunnen worden gezien, maar met RTM kunnen nog kleinere (figuren 7.6e en f) gebieden worden gemeten. Hoewel rastertunnelmicroscopie een krachtig hulpmiddel is, kan de benodigde betrokkenheid van de gebruiker een belemmering vormen. Voor een scherp, atomair beeld, moet de RTM-naald atomair scherp zijn. Het proces om een dergelijke naaldtoestand te verkrijgen, kan tijdrovend zijn. Onlangs zijn verschillende onderzoeksgroepen begonnen met het ontwikkelen van gereedschappen om het conditioneringsproces van de naald te automatiseren. Automatisering heeft een duidelijke waarde bij het creëren van kunstmatige materie gemaakt van individuele adsorbaten, maar ook meer in het algemeen bij sondemicroscopie. Een deel van de oplossing omvat beeldherkenningstechnieken, waaronder neurale netwerken.
Dit proefschrift draagt op een aantal manieren bij aan het werk aan kunstmatige roosters geproduceerd met het CO/Cu(111)-platform.

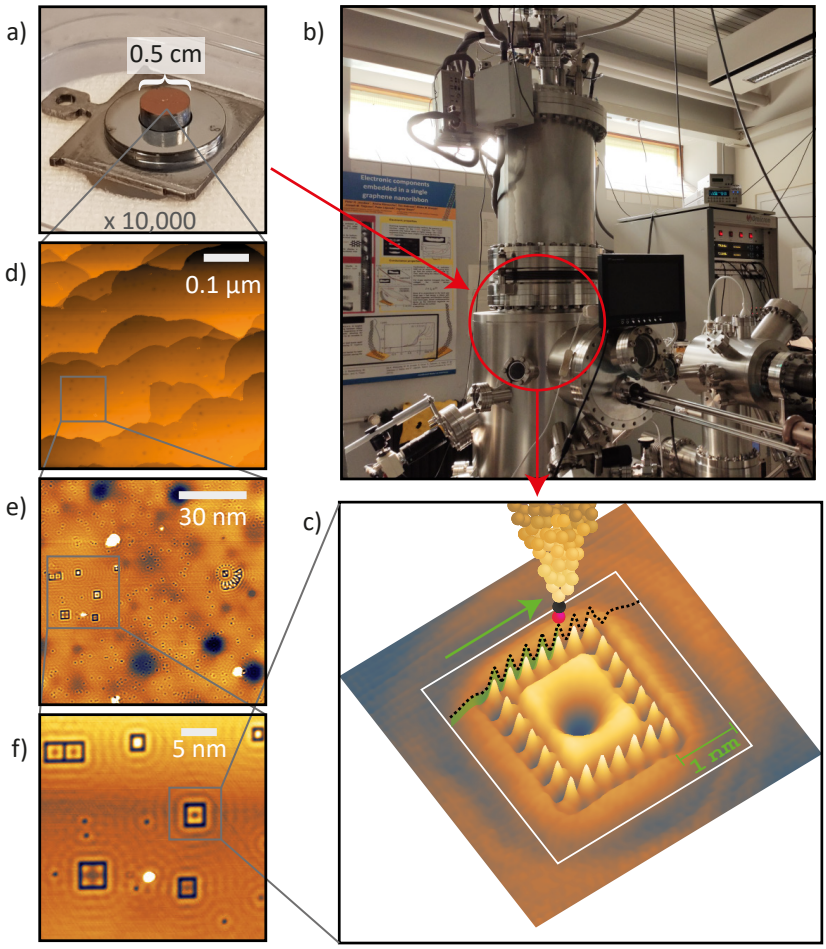

▲ Figure 7.6: **Inzoomen op kunstmatige roosters.** (a) Een koperkristal met een (111) getermineerd oppervlak. (b) De Omicron LT-STM waarin experimenten werden uitgevoerd. (c) Schematische weergave van een CO-getermineerde naald die een kwantumkraal scant (de scan is een echt experimenteel plaatje). (d) Een Cu(111) oppervlak, met zichtbare terrassen. (e) een vlak terras betere weergave van, waar een "kwantumspeeltuin" is aangelegd. (f) een beter zicht op vierkante kwantumkralen.

7.2.1 Automatische tipconditionering

Ten eerste hebben we in hoofdstuk 3 geprobeerd de efficiëntie van rastertunnel microscopie als geheel te verbeteren. Veel tijd besteden aan het voorbereiden van de RTM-naald is een veelvoorkomend punt van klaagzang onder rastersondemicroscopisten - vertel dit aan iedereen in het veld en ze zullen je bijna zeker verrassen met een tragisch verhaal over verloren tijd. Dergelijke repetitieve taken zijn echter bijzonder geschikt voor automatisering, en pogingen om dit tot stand te brengen zijn al in volle gang. We hebben aan dit werk bijgedragen door een op een neuraal netwerk gebaseerd algoritme te maken dat de staat van de tip kan onderscheiden (dat wil zeggen, om een RTM-afbeelding te categoriseren in de volgende types: scherp, dubbel, onstabiel, onzin, terrassen of slecht gebied). De dataset bevatte afbeeldingen van een Au(111) oppervlak en het uiteindelijke netwerkensemble had een nauwkeurigheid van 88 %. Dit hoofdstuk is een stap in de richting van de integratie van automatisering in RTM. Er worden momenteel inspanningen geleverd om het proces voor het CO/Cu(111)-substraat te automatiseren.

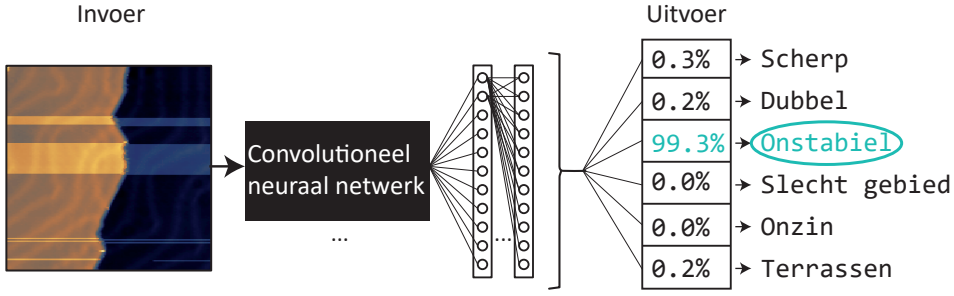

▲ Figure 7.7: We hebben gebruik gemaakt van een convolutioneel neuraal netwerk (VGG-16) om afbeeldingen automatisch te classificeren. Aan de linkerkant toont het RTM-afbeelding van Au(111) tipveranderingen tijdens de scan. Een typisch resultaat voor een afbeelding als deze wordt aan de rechterkant gegeven, waar de voorspelling voor dit voorbeeld correct wordt weergegeven als 'onstabiel'.

7.2.2 Kunstmatige atomen en moleculen

In hoofdstuk 4 zijn we overgeschakeld naar het CO/Cu(111)-platform. Daar hebben we kwantumsimulatie op een meer fundamenteel niveau onderzocht dan in eerder werk door letterlijk terug te gaan naar het begin. Dat wil zeggen, we onderzochten de elementaire componenten van kunstmatige roosters geconstrueerd met het CO/Cu(111)-platform: kwantumkralen van vierkante en driehoekige geometrieën. Talloze roosters van dit type waren al gerealiseerd op het moment van dit project, maar het volledige scala aan beschikbare parameters om te tweaken (zoals gedefinieerd in de "tight-binding" beschrijving) was niet bekend. Op een systematische manier hebben we beschreven hoe de energie van driehoekige en rechthoekige koralen omgekeerd afhangt van het omsloten gebied, waarbij we ook opmerken dat hoe kleiner de koraal is, hoe groter de verbreding van de pieken in differentiële conductiespectroscopie. Ten tweede presenteerden we een methode om strakke bindingsparameters te extraheren door kralen in dimeren en trimeren te koppelen, en lieten we zien hoe de parameters konden worden gevarieerd wanneer de grootte van de kraal of het aantal CO-moleculen die ze scheiden, werd gewijzigd. We ontdekten dat de hoppingintegraal kon worden ingesteld tussen 0 en -0,3 eV en -0,16 eV voor respectievelijk s - en p -achtige toestanden, en ontdekten dat overlap doorgaans een belangrijke bijdrage was. Ten slotte leverden we controle op het (kunstmatige) orbitaal niveau door s- en p-achtige toestanden te koppelen, en bovendien selectief $s - p_y$ -bindingen te vormen terwijl $s - p_x$ -bindingen werden geremd.

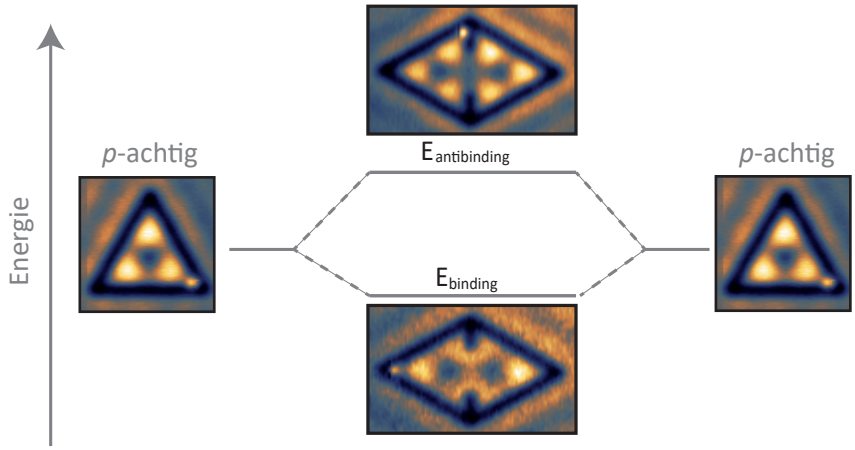

▲ Figure 7.8: Het koppelen van de p -achtige toestanden van driehoekige kralen levert bonding en antibinding toestanden op.

7.2.3 Topologie creëren

Hoofdstuk 5 beschreef een voorbeeld van een volledig kunstmatig (en dus niet in de natuur voorkomend) rooster. In dit geval werd het gerealiseerd op het CO/Cu(111)-platform. Aan dit experimentele project lag een theoretische voorspelling ten grondslag: door de bindingen in grafeen te moduleren en een zogenaamd Kekulé-rooster te produceren, kan een gat in de bandstructuur worden geopend, maar niet noodzakelijk aan de randen. In feite kunnen de randtoestanden topologisch niet-triviale banden vertonen, afhankelijk van hun constructie. Dit is interessant; terwijl ze isolatoren zijn aan de binnenkant, is bekend dat de elektronische toestanden op de grensvlakken van topologische isolatoren robuust zijn en niet gemakkelijk verstoord worden door eenvoudige defecten. De onderzoeksvraag was toen: kunnen we dit gedrag nabootsen met behulp van het CO/Cu(111) -platform? Om dit te beantwoorden, hebben we vier configuraties van een Kekulé-rooster geconstrueerd en vastgesteld dat in twee gevallen randtoestanden werden waargenomen en in de andere twee gevallen niet vanwege de onderliggende symmetrieën.

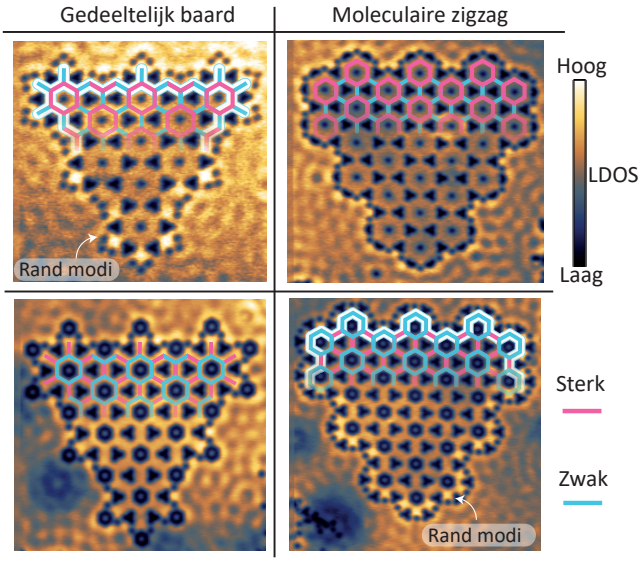

▲ Figure 7.9: Rand-modi manifesteren zich in twee van deze configuraties van het Kekulé-rooster. Dit wordt bepaald door de eenheidscel, die in alle vier gevallen anders is.

7.2.4 Simulaties binnen simulaties: interacties onderzoeken

Ten slotte ging hoofdstuk 6 in op de mogelijkheid om interacties te simuleren in elektronische kwantumsimulatoren. De CO/Cu(111) -opstelling doet het goed bij het simuleren van enkeldeeltjesmodellen, maar is er een manier om de twee-deeltjesfysica te simuleren? Het theoretische antwoord is ja, de Hamiltoniaan die interacties tussen twee lichamen op een 1D-rooster beschrijft, is identiek aan degene die een enkel deeltje in een bepaald 2D rooster beschrijft. We hebben vier verschillende roosters gebouwd. Muffin-tin simulaties lieten zien dat de relevante signaturen van twee-deeltjes interacties te zien zouden moeten zijn in onze artificiele roosters. Echter, de pieken in de scanning tunneling spectroscopie data waren zodanig breed dat er geen sluitend experimenteel bewijs kon worden gevonden voor een succesvolle simulatie van twee-deeltjes interactie.

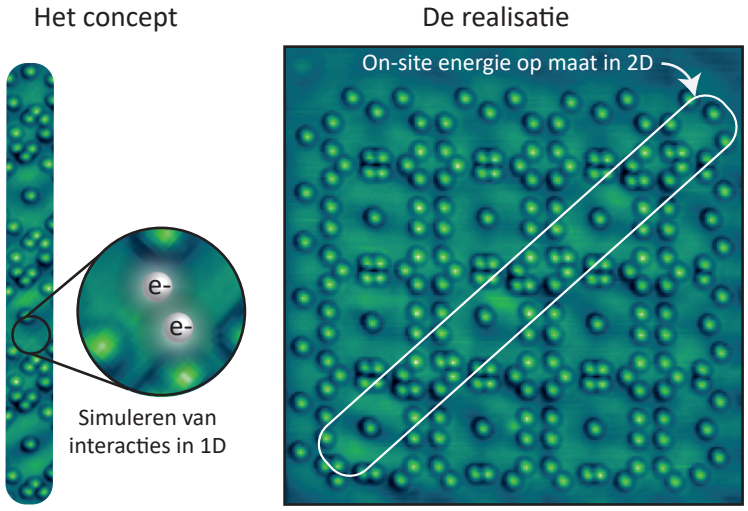

▲ Figure 7.10: Aan de linkerkant is een artistieke weergave van de interacties die we wilden simuleren, die doorgaans niet haalbaar zijn om te meten met onze experimentele opstelling. Aan de rechterkant is een van de roosters die we hebben gerealiseerd om de interacties met twee deeltjes te simuleren. De opname is gemaakt met een CO-getermineerde naald waardoor de CO moleculen verschijnen als uitsteeksels.

7.2.5 Slotopmerkingen

Het CO op Cu(111)-platform is als een kwantumspeeltuin waar we kunnen spelen met elektronische golffuncties en tight-binding parameters in roosters. Deze kwantumspeeltuin is nuttig als experimenteel modelsysteem om exotische fysische verschijnselen te onderzoeken. Er zijn echter enkele beperkingen. Ten eerste, aangezien de oppervlaktebanden op dezelfde energie liggen als bulkbanden, wordt de levensduur van oppervlakte-elektronen verkort, wat een verbreding van differentiële geleidbaarheidsmetingen introduceert. Platforms zoals het InAs(111) -oppervlak, waar de oppervlaktetoestanden zijn losgekoppeld van de bulk en daarom een betere energieresolutie mogelijk maken, zijn een mogelijke remedie. Ten tweede kunnen bepaalde interacties, zoals spin-orbit-interacties, niet worden gemodelleerd met het CO/Cu(111)-platform. Een mogelijkheid is dat door het gebruik van zwaardere elementen, Rashba spin-orbit-koppeling kan worden geïntroduceerd.
De efficiëntie van het maken en onderzoeken van dergelijke kunstmatige structuren zou kunnen worden verbeterd met behulp van een op neuraal netwerk gebaseerd STM-beeldherkenningssysteem, gegeneraliseerd voor veel substraten. Een dergelijk systeem zou automatisch beslissingen nemen over het conditioneren van de tip op basis van de input en het type substraat. Verfijnde geautomatiseerde manipulatietechnieken voor adsorbaten zouden kunnen worden toegevoegd, evenals de mogelijkheid om differentiële geleidbaarheidsspectra te beoordelen.
Als we verder kijken dan STM-gebaseerde onderzoekstechnieken, kunnen type III-V halfgeleiders worden voorzien van kleine gaatjes met behulp van nanolithografie, waardoor een rooster wordt gedefinieerd zoals beschreven in dit proefschrift. Dit maakt de weg vrij voor het verkrijgen van extra informatie over interessante oppervlakken, maar ook voor de mogelijkheid om daadwerkelijk functionele materialen te maken die kunnen worden toegepast.

7.3 Acknowledgements

When I think back over the time spent on my PhD, I sense how fortunate I was to have had such an outstanding working environment at the condensed matter and interfaces group (CMI) at Utrecht University. Moreover, I am delighted with the lovely colleagues, collaborators, supervisors and students I have had the pleasure of working with. In this section, I would like to thank those people, as well as my friends and family for their support.

First of all, I would like to express my gratitude to my supervisors and collaborators.

Ingmar Swart, thank you for the opportunity to work in your wonderful group. I really valued your excellent supervision and encouragement, and for always being so efficient and optimistic. I very much appreciated that you were always available for discussions, and that your advice was always solid. Your goal-oriented mindset helped me greatly whenever I got caught up in details. I liked how when you would visit the basement, equipment and experiments would start working again, like magic. Your supervisory style creates a fantastic working environment that binds together Team Kelder in a way that I will remember forever. Good luck with expanding your group in future!

Daniel Vanmaekelbergh, thank you for the opportunity to work in your group. I valued your supervision and discussions. I especially appreciated your knowledge that was both broad and deep, and that you had input on any topic I was working on.

Cristiane Morais Smith, your sheer drive and passion for physics is incredible. Your ability to generate new ideas and your eye for detail were of so much value during our Kekulé and dimerized square projects. I really admired and appreciated your enthusiasm and positivity throughout our projects – Thank you!

Jette van den Broeke, we worked together like a well-oiled machine during the Kekulé project. Your theoretical predictions were like blueprints for the factory floor that was the STM. Thank you for always so competently answering my thoughts when it came to theory in general, and thanks for all the good times we had together, partying (with Zelda), chilling at the beach, attending conferences and playing Animal Crossing at the start of lockdown. And of course, thank you for being one of my paranymphs!

Sander Kempkes, it was really a pleasure to collaborate with you on the dimerized square project. The advice you gave from the theoretical perspective was always on point, and of course of great value. I enjoyed attending the designer quantum materials conference with you in San Sebastian. While we were there, it was great fun preparing for Marlou's defense together as her paranymphs!

Marco Di Liberto, thank you for the lovely collaboration on the dimerized square project. I appreciate your many extensive explanations and ideas along with the passion you had for your work. I'm very grateful that you were willing to answer all

the questions I had!
Philip Moriarty, thank you for your liveliness and ambition during the automated STM project! As with during my master's project, it was a pleasure. Thank you also to **Oliver Gordon** and **Filipe Junqueira** for the collaboration, and **Greg Wilkinson** and **George Tucker** for their fruitful visit to Utrecht from Nottingham.
Next, I would like to thank each of my students. I am very grateful for the talent and dedication that each of them delivered.
Meike Bos, the first student I supervised (together with Marlou): thank you for working with us on the notoriously difficult to prepare lead surfaces. I also had fun on the physics outreach day where you made LN2 ice cream!
Jan Jurre Harsveld van der Veen, here is a haiku for you: *Once upon a time – COs were neatly arranged – down in the basement.* Thank you for all the atomic construction you did during your master's project on the Kekulé lattice. At some point we realized we could compete for the minimum time for building a unit cell (I believe the record was 07:12). After that, our progress was relentless – we even went as far as to win a prize for the best poster at the Dutch SPM day 2018.
Lisanne Knijff, I still sometimes think of how you classified thousands of images for the automatic tip-prep project. You started learning Python before coming to work at our group, and impressively, mere weeks later, you were already training neural networks with us. Thank you for being excellent, for your blunt sense of humour, and for the good times.
Sam Borman, your unwavering perseverance throughout our project on artificial atoms was commendable. We gave it our best shot to manipulate CO on Cu(111) in the Fermi STM, but the very moment that the Dirac was available, you instantly got to work on building. You took it upon yourself to collaborate with **Mickey Bramer** at theoretical physics, and you never gave up with fitting Gaussians to the experimental data. Thank you for your great work!
Jaap Harteveld, we slammed out glorious results on square artificial atoms and molecules with "only minor" setbacks, running on little more than peanuts and cortisol. Thank you for your conscientiousness, your insightful quips, and all the laughs and positivity you brought.
Of course, I must thank not only my students but also everyone else in "**Team Kelder**", our sub(surface) group at CMI. I truly enjoyed the collaborative and positive dynamic that we shared and that you continue to share, and I feel fortunate to have been in a group like this for my PhD. Each time someone needed help, it was a given that someone would be there. Whether it was inside or outside of the lab, I learned something from each one of you. We had fun times playing table football and lamenting in the lab over non-compliant equipment. We also had great outings in pre-corona times; not only to scientific conferences, but also boating at the Biesbosch, singing karaoke, poker, bowling and gaming (both virtually and together at a video game bar).

Nadine van der Heijden, the queen of AFM, you taught me perhaps the majority of my functional knowledge of the basement equipment. My original project was about metal organic frameworks, and you were there to help with teaching me to prepare samples. Thank you for your good spirits, I certainly learned a lot from you and it was always a pleasure chatting to you back in the day!
Marlou Slot, you radiate a positive, committed and sustained passion to your work that leaves an impression on everyone around you. Your attitude towards science is an inspiration and your enthusiasm is infectious. Thank you for all the knowledge and moments of clarity you gave me and everyone else. Aside from that, I want to thank you for all the fun we had together inside and outside of the lab; kayaking, (watching you) singing, visiting conferences etc.
Peter Jacobse, everyone can learn a thing or two about dedication from you when it comes to you and Mathematica. Thank you for making the lab a brighter place with all your puns, wiener mélanges, and certain basement melodies. You've since continued to brighten my life with sunny pictures from California.
Thomas Gardenier AKA real Thomas, thank you for the Gauss tutorials! I appreciate the upbeat, can-do attitude that you bring to the basement. I enjoy the trivia and facts you like to share.
Jaco Geuchies, thank you for being so welcoming and friendly, I enjoyed our conversations.
Mark Mangnus, thank you for your good teamwork and good humour down in the basement!
Pascal Vermeeren, you brought a cool new dimension to Team Kelder with your astrochemistry research. Thank you for your positive and hardworking attitude down in the basement, especially at times of misfortune (R.I.P space rust). Luckily you made up for it with your calculations that resulted in a whopping 20 publications, at the time of writing.
Jesper Moes, thank you for being a great colleague. You brought emotional support to the Dirac lab daily with tea and complaints sessions. When corona struck, you were sometimes the only person I would physically see for the week when we would fill the cryostats, so I am grateful to you for my sanity. Thanks for always being up for some gezelligheid and banter, and for the social cohesion you bring to CMI.
Jos Mulkens, thank you for your unparalleled, untiring curiosity and for the zest with which you live your life. Thanks for teaching me a bit about singing; the Christmas carols and the preparation for Marlou's defense were great fun.
Pierre Capiod, thank you for both the intellectual and literal muscle you provided us down in the basement. You also brought great fun with karaoke, Eurovision and Halloween festivities.
Rian Ligthart, you did some cool work on circular corrals with magnetic fields. I appreciate the work you put into the Python muffin tin program; it came in really handy. Thanks also for letting me use your nice 3D animation in my presentations!

It was fun doing aerial acrobatics together sometimes!
Jan Cuperus, thank you for your scientific attitude and the good work you did on Bi(111). It was always great to walk into the Gauss lab to see what you were up to. Good luck with the remainder of your PhD!
Tomas Meerwijk AKA reciprocal Tomas, thanks for your great attitude and the fun!
Katerina Vaxevani, thanks for the cool presence you brought to CMI. I enjoyed partying with you to alternative throwback songs, and doing intensity workouts together.
Auke Vlasblom, thank you for your cheerful demeanor and your cool work on the automated tip preparation project! You always did a good job explaining it.
Leon Arends, thank you for the good work you did with simulating STM images, I always loved to hear it in the virtual group meetings during corona.
Thank you to **Julia van der Burgt, Margriet van Riggelen, Noor ten Veen, Luuk Goode, Thomas Mercadier** AKA French Thomas, and **Roel van Wijk** for bringing your good working attitudes and positivity to Team Kelder!
We would be in quite a dire situation if it weren't for the Scienta Omicron service technicians. Thank you to **Jens Garleff** for answering my questions in great detail, for showing me the inner mechanisms of the Omicron LT-STM (Dirac), and for the good conversations. Thank you to **Mehrdad Atabak** for teaching me about the Fermi STM. Thank you also to **Andreas Bettac** for the support with the Polar STM (Gauss).
Next, I would like to thank the very capable support staff at CMI.
Stephan Zevenhuizen, thank you for sharing your talents with us, and for being willing to help with my many technological queries. Your program Snap Zone and your Python modules for interfacing with MATRIX made my life much easier. Your work on the muffin tin code was also invaluable.
Hans Ligthart and **Peter van den Beld**, thank you for the technical support that you provided for the lab equipment and STMs. Your skills were of critical importance for the smooth functioning of the lab.
Linda Kumeling and **Silvia Benschop**, thank you for always responding so quickly to my administrative questions. Thanks also for your friendliness.
Thank you to the PIs of CMI who I haven't yet thanked, **Andries Meijerink, Celso de Mello-Donegá** and **Zeila Zanolli** for your organisation and knowledge.
To my office mates: The chats we had together were lovely, and we had great fun outside of the office doing mini golf at night and playing pool. Between Annalisa getting relentlessly teased and Christiaan and Tim communicating in a language that I am not sure was Dutch (or any language), we created a cosy office (also quite literally cosy with the sofa, plants and bunting).
Tim Prins, thanks for your reassuring presence in the office. I really enjoyed our chats, and I appreciate that you taught me a thing or two about Dutch culture!
Annalisa Brodu, thank you for balancing out the office temperature. Don't tell

anyone, but sometimes I was kind of cold after you left. Aside from that, thanks for being so friendly. I appreciate how welcoming you were when I first arrived!
Christiaan Post, thanks for your cuddly presence in the office and beyond. There is scarcely anything in this world that warms my heart more than your pure smile.
I would like to thank all my colleagues CMI for the overall gezelligheid. I really enjoyed the sports days, outings, birthday coffee breaks, and Christmas dinners. I want to thank Sinterklaas for visiting each year without fail, even digitally during corona. I also very much appreciated that during corona we maintained contact with virtual group meetings and borrels.
Naud van Bunningen, you are a character and a legend. Your unique mind is a cornucopia of curiosities. Thank you for sharing some of them with me and for being ridiculous – in a good way. I enjoyed philosophizing over life's questions with you, as well as playing games and sharing good YouTube videos.
Serena Busatto, thank you for your warmth and good spirits, I really enjoyed our chats.
Liudmyla Chepyga, I like that we helped each other to improve our Dutch – thanks!
Ian Pompermayer Machado, I really appreciated your good storytelling and welcoming presence. I had great fun splashing in the sea at Scheveningen with you – I bet it would be even more fun to do the same in Brazil!
Carlo van Overbeek, thanks for being so welcoming when I first arrived!
Maaike van der Sluijs, aside from your friendliness, thank you for the vegan treats you made on your birthday, and for alerting me about new vegan places in Utrecht!
I thank you **all** sincerely for making CMI a wonderful place to work, **Maryam Alimoradi Jazi, Anne Berends, Annelies van der Bok, Kelly Brouwer, Sophia Buhbut-Sinai, Pradip Chakraborty, Luke Chadwick, Jeppe Christiansen, Philipp Dolata, Riande Dekker, Daniele Fabri, Robin Geitenbeek, Ellenor Geraffy, Onno Gijzeman, Marie van de Haar, Elleke van Harten, Jacobine van Hest, Thimo Jacobs, Alicia Jiménez, Matthijs de Jong, Anna Kaczmarek, Vasilii Khanin, Saydi Knook, Jintao Kong, Martijn Mekkering, Federico Montanarella, Pedro Monteiro Campos de Melo, Christa van Oversteeg, Matt Peerlings, Konstantina Pepelasi, Joep Peters, John Pold, Freddy Rabouw, Riccardo Reho, Bas Salzmann, Georgia Samara, Tim Senden, Guiseppe Soligno, Atul Sontakke, Kelly Sowers, Claudia Spallacci, Ward van der Stam, Jesse Steenhoff, Markus Suta, Thomas van Swieten, Pedro Villanueva-Delgado, Jelmer Visser, Jara Vliem, Patrick van Vliet, Joren Vos, Sadakazu Wakui, Winston Wang, Harold de Wijn, Jur de Wit, Weiwei Wu, Chengui Xia, Allan Xu, Wenjin Xu, Dechao Yu, Ting Yu** and **Dirk Floris Zwarts**.
Outside of work, I'd like to thank the wonderful friends I that I made after coming to the Netherlands, in no particular order:

Helen, thank you for being such an amazing friend. I don't know where I would be without you. I love you dearly. Thank you for being my paranymph.
Abel, at the time of writing we have sent a total of 59,558 messages to each other. You are a bro and you make me laugh daily. Thanks for letting me take care of your adorable chickens who I love and relate to on a personal level.
Nish, we were already students together in Nottingham but we both live in Utrecht now, thank you for all the fun we had together, especially skydiving.
Till, thank you for the weekly runs we do through Utrecht and for the fun board games. Thanks also for letting me work with you regularly during corona, I was much more efficient with writing my thesis there.
Victor, thank you for all the hilarious times and good chats. I hope that some day I can climb ropes and do handstands just like you.
Sorsha, I've had good fun with you at Dutch lessons, taking your cat Kaspi for a walk, eating Vietnamese wraps, second hand shopping and painting, thank you for your awesomeness!
Jie, Julia and **Alice**, we had fun learning Dutch together! Thanks for the fun times outside of the Dutch lessons.
Benjamin, thank you for being a great dungeon master, I had so much fun.
Nilam and **Thomas**, we had good times when we were neighbours in de Bilt - I miss popping around to each other's places for tea.
Nathan, I always have such a good time with you whenever we are together, whether it be at the Efteling or simply eating our veggies. Thank you for your warmth, kindness, patience, honesty, openness and of course your stroke of comedic genius. I appreciate the happiness we added to each other's lives, especially during the darkest depths of lockdown in the bleak midwinter. Thanks for spending Christmas and New Year's with me when I could not be with my family.
Amrita, my neighbour and first friend in the Netherlands, thank you for your delicious cooking and for all your love. I still make your dal recipe to this day. Thank you to **Asitav** as well for the good chats!
I'm grateful to my housemates that I've had over the years in the Netherlands for generally being amazing: **András, Patrick, Bruno, Frédéric, Sam, Lauriane, Giusi, Manolo, Yvonne, Sanne** and **Daan**. I've had so much fun with all of you.
I'd like to thank my group of dear friends who I met at the University of Nottingham in the UK; **Cat, Catriona, Ian, Jon, Martin, Matthew, Natasha, Will**, and **Alex**.
When I was able to visit you and vice versa, we had the usual ridiculous laughs. Thanks for always keeping me virtual company, for the Minecraft, anime and video chats. Most of all, thank you always for being good friends. Particularly to Alex: thank you for all your support and all the good times, hilarious times and beautiful times.
From the bottom of my heart, I would like to thank my best friends from London.

I consider you sisters and I love you; **Jennifer, Liza, Meena, Nathile** and **Rae**. Thank you for the holidays together and the support of all kinds.
Lastly, I would like to thank my family. **Mum**, thank you for the opportunities you gave me in life, it is thanks to your hard work and influence that I got to this point. My brothers **Tadhg, Fergus** and **Sherman**, I thank each of you for being you, and for all the laughs and insight you provide. **Fat Jack** is a cat and cannot read this, but I love him too. I appreciate all members of my extended family for being so welcoming when we visited Ireland and Bermuda. Finally, I am grateful to my **dad** - who passed away in December 2017 - for the boundless love and kindness he had for me, and for the memories I will always treasure.

7.4 Publications

This thesis is based on the following articles:

- S.E. Freeney, M.R. Slot, T.S. Gardenier, I. Swart, and D. Vanmaekelbergh. *Electronic quantum materials simulated with artificial model lattices.* In preparation
- S.E. Freeney, S.T.P. Borman, J.W. Harteveld, and I. Swart. *Coupling quantum corrals to form artificial molecules.* SciPost Phys **9**, 085 (2020)
- S.E. Freeney, J.J. van den Broeke, A.J.J. Harsveld van der Veen, I. Swart, and C. Morais Smith. *Edge-Dependent Topology in Kekulé Lattices.* Phys. Rev. Lett **124**, 236404 (2020)
- O. Gordon, P. D'Hondt, L. Knijff, S.E. Freeney, F. Junqueira, P. Moriarty, and I. Swart. *Scanning tunneling state recognition with multi-class neural network ensembles.* Review of Scientific Instruments. **90**, 103704 (2019)

Other publications:

- S.N. Kempkes, M.R. Slot, S.E. Freeney, S.J.M. Zevenhuizen, D. Vanmaekelbergh, I. Swart, and C. Morais Smith. *Design and characterization of electrons in a fractal geometry.* Nature Physics **15**, 127–131 (2019)

7.5 Conference contributions

Poster January 2020	Quantum corrals as Artificial Atoms *Physics@Veldhoven, Netherlands*
Talk November 2019	Constructing Topological Insulators Atom-by-Atom *Dutch SPM day, AMOLF, Amsterdam, Netherlands*
Poster July 2019	Constructing Topological Insulators Atom-by-Atom *Quantum Designer Physics Workshop, Donostia/San Sebastian, Spain*
Poster March 2019	Constructing Topological Insulators Atom-by-Atom *Physics department day, Utrecht University, Netherlands*
Talk March 2019	Constructing Topological Insulators Atom-by-Atom *DPG Spring Meeting, Regensburg, Germany*
Poster January 2019	Constructing Topological Insulators Atom-by-Atom *Physics department day, Veldhoven, Netherlands*
Poster (1st prize) November 2018	Constructing Topological Insulators Atom-by-Atom *Dutch SPM day, Utrecht University, Netherlands*
Poster July 2018	Constructing Topological Insulators Atom-by-Atom *SPSTM-7 & LTSPM-1 International Conference, Nijmegen, Netherlands*
Poster September 2016	Towards autonomous scanning probe microscopy *NC-AFM summer school, Osnabrück, Germany*

7.6 About the author

Saoirsé [†] Erin Freeney was born in London, United Kingdom, on the 9th of April 1994. She is of Irish and Bermudian descent. From 2005 to 2012, she attended St. Anne's Catholic High School for Girls in London, studying biology, mathematics, physics and chemistry at A-level. During this time, her interest in science, particularly physics, was piqued by reading popular science books such as *Quantum Theory Cannot Hurt You* and *A Brief History of Time*, as well as attending weekly public lectures at University College London.
In 2012, she enrolled in a combined bachelor's/master's programme in Physics at the University of Nottingham, exceeding her expected grades for entry and winning a Sir Peter Mansfield high achiever scholarship. Her bachelor's project involved modelling three-body asteroid interactions using MATLAB under the supervision of Prof. Michael Swift. Her master's project was on the automation of image recognition of scanning probe microscopy images, supervised by Prof. Philp Moriarty. Her programming skills for these projects were facilitated by programming courses during her studies, including the image processing course where she created a facial recognition program. In her spare time, Saoirsé participated in physics outreach events in Nottingham (Science in the Park and Nottingham Light Night). She also enjoyed participating in hackathons at the university.
In 2016, she graduated from the University of Nottingham and accepted a PhD position in Utrecht, Netherlands, under the supervision of Ingmar Swart and Daniel Vanmaekelbergh. This was an NWO project titled "Functionalized organic-metal (FOM) networks: a platform for designing Dirac fermions". Saoirsé has published her work in peer-reviewed journals and has presented at (inter)national conferences. During her PhD, she supervised one master's student and four bachelor's students for their experimental and computational projects. She also provided teaching assistance for several courses: Solids and Surfaces (three times), Quantum Chemistry (twice), and Physics for Chemistry students (once). At the time of writing, Saoirsé's level of Dutch is approximately B1.
Outside of science, Saoirsé enjoys aerial acrobatics, frequenting the gym, running and calisthenics. She also likes cooking (delicious vegan food) for friends, casual drawing/painting, and animals. For fun during corona lockdown, she did some short programming projects with friends, and befriended two Eurasian collared doves with her housemates.

[†]Saoirsé is pronounced "Sersha", to rhyme with inertia. It is the Gaelic word for freedom.